Probabilistic Tsunami Hazard Assessment (PTHA) for Crescent City, CA

Final Report
August 30, 2014

Frank I. González, Randall J. LeVeque, and Loyce M. Adams
University of Washington

Chris Goldfinger, Oregon State University

George R. Priest, Oregon Department of Geology and Mineral Industries

Kelin Wang, Geological Survey of Canada

This report supercedes the Phase I PTHA Report [23]

Photo Source: http://tripsintohistory.com/wave-propagation-content/uploads/2012/03/
800px-Crescent_City_California_harbor_aerial_viewUSArmyCorpofEngineeers1.jpg

Contents

1 Executive summary

This report builds on and supercedes Phase I of a demonstration Probabilistic Tsunami Hazard Assessment (PTHA) study of Crescent City, California [23], which developed an improved methodology for PTHA and associated products that addressed only tsunami flooding depth.

The study documented in this report was originally conceived as a follow-on that simply extended Phase I products to include additional tsunami parameters associated with tsunami flow in particular, current speed and momentum flux. As this study was underway, however, it was reviewed by the California Probabilistic Tsunami Hazard Analysis Work Group (CA PTHA WG) [25] that included experts on various PTHA issues, most notably the critical issue of seismic source specification. Subsequently, the CA PTHA WG review concluded that the CSZ sources used in the Phase I work was not adequately consistent with the 2014 Update to the National Seismic Hazard Maps (NSHM) [54]. Consequently, an improved suite of CSZ sources had to be developed that was more consistent with the NSHM, as discussed in Section 7.6. As a consequence, the entire set of inundation model simulations had to be repeated and new PTHA flow depth products were developed. The results presented here thus supercede the results presented in the Phase I report [23].

Both Phase I [23] and this study were funded by BakerAECOM and motivated by FEMA's desire to explore methods to improve products of the FEMA Risk Mapping, Assessment, and Planning (Risk MAP) Program. Here we briefly summarize the goals, deliverables, technical challenges, additional work, primary results and conclusions, and recommendations of this study.

1.1 Goals

The primary goal of this pilot study was the development of improved PTHA methodology. As such, it is important to note that the probabilistic flood maps and other products included in this report are illustrative only and are not intended as guidance for operational decision-making, even though every effort was made to produce products consistent with best available science, within the limits of time and resources. In particular, there is significant uncertainty in the results because they are highly dependent on CSZ source specification, and source specification is an active area of research and debate by the scientific community.

1.2 Deliverables

The deliverables of this project were to be

- A final report that documents the development, testing, and application of an improved PTHA methodology, including a summary and discussion of results and recommendations for possible FEMA applications.

- Maps of maximum wave height and flood depth, current speed and momentum fluxes, with 1% and 0.2% annual probabilities of exceedance, i.e., the 100- and 500-year tsunami maps, referred to as the "deliverable maps".

- Digital data files for the deliverable maps of 1% and .2% annual probabilities of exceedance for the four quantities of interest above, plus other supporting files described in detail in Appendix D.

1.3 Technical challenges

In the course of this study, two significant technical challenges arose that had to be met:

- **Inadequate CSZ Sources representation.** Because of advances in methods to generate stochastic seismic slip realizations, and because the Bandon, Oregon study by Witter, et. al. [61] clearly demonstrated the need for additional seismic scenarios – see Section 7.6.1 and Section 10.1, we first adopted the 15 Bandon sources as 15 realizations of a Cascadia event instead of pursuing our original plan to use the 12 Cascadia sources of the Seaside, Oregon PTHA study by González et. al. [22]. Then a

review by the California Probabilistic Tsunami Hazard Analysis Work Group [25] noted that these 15 Bandon sources we hoped to use in our final study lacked smaller, segmented scenarios in the Southern CSZ [20] and recommended that these sources be included in order to bring our work more into line with the 2014 Update to the National Seismic Hazard Maps [54]. As a result, we added two additional sources to the 15 and these are discussed in Sections 7.6.1 and 7.6.2.

- **Inadequate method for Tidal Uncertainty estimation.** Analysis revealed that, in contrast to the behavior of wave height and flooding depth, current speed and momentum flux are not monotonic non-decreasing functions of tidal stage. A significant R&D effort was therefore required to develop and test a more general method to estimate tidal uncertainty that could be used in the case of non-monotonic behavior. In response to this challenge, we developed the Pattern-Method [3] and used this method to include tidal uncertainty for all our quantities of interest. This is also discussed in Section 8.

1.4 Additional products and improvements

- We included a Japan tsunamigenic seismic source (*because the 2011 Tohoku event inflicted heavy damage on Crescent City and the West Coast – see Section 6.2 and Section 7.5*).

- We developed additional products with potential value to improve or supplement current deliverable maps (*because FEMA expressed a strong interest in such an effort – see Section 9.2*). These include p-contour plots, transect plots, deaggregated hazard curves and p-contour plots by earthquake zone.

- We also produced results for extended recurrence intervals of 300, 975, 2500, and 5000 years in addition to the deliverable maps of 100 and 500 years. This was in response to a strong interest expressed by the CA PTHA WG for PTHA products applicable to other applications requiring different Annual Return Period (ARP) risk levels [25].

- We improved the GeoClaw tsunami model and implemented GeoClaw-compatible tools for post-processing analyses and visualization. This improved GeoClaw was used to produce results for this study.

- The $1/3''$ grid used to monitor maximum depth, velocity, and momentum flux is now aligned with the $1/3''$ grid on which the bathymetry is specified. (In the Phase I results, these grids were slightly misaligned.)

1.5 Primary results, conclusions, and recommendations

The primary results include the 100- and 500-year tsunami deliverable maps. They are presented and discussed in Section 3 and Appendix C. These maps were generated by a significantly improved methodology than that of the Seaside study; the improvements include a more complete set of seismic sources (Table 1), and a more accurate method for estimating tidal uncertainty (Section 8). As expected, the inland extent and magnitude of the flooding for the 500-year tsunami far exceed that of the 100-year event; these products can now be compared with standard FEMA Flood Insurance Rate Maps (FIRMs) to determine whether these flooding levels exceed estimates of other coastal flooding hazards, such as storm surge. A final deliverable, digital data files of this map data, have been provided to BakerAECOM, and a description of these files is given in Appendix D.

Two of the primary conclusions we reached in the course of this study is that (a) the standard product, i.e., the deliverable maps that display annual probabilities of exceedance, can be highly sensitive to geophysical uncertanities and (b) maps of annual probabilities of exceedance presented alone can, under certain circumstances, even be misleading. Section 9.2 discusses these two issues in the context of another product that provides valuable additional insight by presenting the same probabilistic information in a different format that we call a *p*-contour map.

Finally, we recommend (a) that FEMA give serious consideration to the adoption of the p-contour map as a product that supplements and aids in the practical interpretation of the same probabilistic information displayed in the standard 100- and 500-year tsunami deliverable maps, and that (b) future PTHA studies should include close collaboration with a geoscientist expert in earthquake parameterization.

2   Introduction

This report documents the results of a pilot study supported by BakerAECOM to conduct a Probabilistic Tsunami Hazard Assessment (PTHA) of Crescent City, California for tsunamis generated by local and distant earthquakes. The report builds on work conducted as part of Phase 1, which dealt only with flooding depth. This study re-examines flooding depth and extends the PTHA methodology to include probabilistic products for tsunami current speed and momentum flux.

The results presented here supercede those of the Phase I report because (a) an improved suite of CSZ seismic sources was developed and, as a consequence, all inundation modeling simulations had to be re-run and (b) an improved tidal uncertainty method was developed [3] and applied in the development of all products presented here.

For the convenience of the reader, we have repeated in this report much of the content of the Phase I report that is informative and has not been superceded. The motivation for this approach was to create a stand-alone report that would not require frequent reference to Phase I report content.

The project is part of a coastal modeling/mapping effort funded by the Federal Emergency Management Agency (FEMA) Region IX office as part of the new California Coastal Analysis and Mapping Project (CCAMP). In turn, CCAMP is being conducted under the nationwide FEMA Risk Mapping, Assessment, and Planning (Risk MAP) Program, which focuses on providing communities with flood information and tools to enhance their mitigation plans and better protect their citizens.

2.1   Acknowledgements

Many colleagues have contributed ideas and insights that have guided the new approaches we suggest in this report, and/or provided guidance on aspects of the seismic modeling that is critical input to the tsunami modelling. In particular we want to acknowledge contributions of Brian Atwater, Art Frankel, Eric Geist, Finn Lovholt, Martin Mai, Geir Pedersen, Jonathan Varkovitzky, and Tim Walsh. The CA PTHA Work Group [25] provided valuable feedback and suggestions on our Phase I work which guided some approaches we adopted in the work reported here.

Knut Waagan participated in many discussions on stochastic approaches and the possible development of new methodologies, with funding and mentoring provided by Guang Lin at the Pacific Northwest National Laboratory in Richland, WA. The GeoClaw software was developed in collaboration with David George and Marsha Berger, with recent contributions by Kyle Mandli and others. This software builds on the Clawpack software that many others have also contributed to.

This research used resources of the Pacific Northwest National Laboratory Institutional Computing (PIC) Facility, which is a DOE Office of Science Urser Facility.

2.2   Goals

The goals of this study are to:

- Improve the PTHA methodology developed in Phase I by extending its capabilities to include tsunami flow-related variables such as current speed and momentum flux.

- Apply the improved PTHA methodology to the production of Crescent City maps that depict the 0.01 and 0.002 annual probability that certain level of wave heights and flooding depth, current speed, and momentum flux will be exceeded – i.e. the Crescent City "100-year" and "500-year" tsunami maps for all four of these quantities of interest. See Section 3 and Appendix C for some examples of these deliverable maps.

- Develop new approaches to efficiently generating probabilistic maps related to tsunami hazards, including suggestions for new ways of viewing and interpreting the data. See Section 9 for some examples of these additional products.

2.3 Limitations

We have identified many sources of uncertainty in the course of this work that have been impossible to properly quantify, even probabilistically. These are discussed further in Section 4 and in the context of our results in later sections. We want to stress that all probabilistic maps generated as part of this study are themselves uncertain, and are based on assumptions about the probability distributions of possible earthquake sources that are often not well defined. They are our best estimates based on what we have been able to identify as the best available science. For more information on some of the sources of uncertainty, see Section 4 and Section 10.

It is also important to keep in mind that rare events do sometimes happen, and so even if the probabilistic maps were exactly correct, it could still happen that a region where the annual probability of inundation is extremely low could be flooded tomorrow if the corresponding event occurs.

2.4 Scientific approach

This study builds on and extends the improved methodology developed in Phase I of this project [23]. Improvements of note including those of Phase I are:

- *CSZ Sources.* The suite of CSZ sources used in Phase I have been extended to include two additional scenarios in the Southern CSZ that improves consistency with the guidance provided in the 2014 Update to the National Seismic Hazard Maps [54].

- *Improved GeoClaw software.* The GeoClaw software, see Section 5 uses adaptive grid refinement to efficiently model the tsunami propagation. This code has been benchmarked, validated, and approved for such studies. Since Phase I, an improved version has recently been released. This version was used for results in this report. Careful comparisons with Phase I results for several cases were used to insure that changes to GeoClaw did not substantially affect any results.

- *Tidal Uncertainty estimates.* The methodology developed in the Phase I study has been improved and extended to include analyses of variables that include tsunami flow, such as current speed and momentum flux [3]. In Phase I each tsunami source was run with 3 tide levels, which was deemed adequate for incorporating tidal uncertainty of flow depths. For Phase II, each scenario was run with 5 tide levels since velocity and momentum flux vary less smoothly with tide level (see Section 8).

- *Japan source.* The addition of a far-field source in Japan, based on information updated since the 3 March 2011 Tohoku tsunami (Japan Earthquake Research Committee, 2011 [27]); see Section 7.5. This was also used for Phase I.

- *Additional products.* In Phase I, we generated sample products that may prove useful when interpreting probabilistic results, in particular contour maps of probability of exceedance for different exceedance levels; see Section 9.2. These products are now augmented with deaggregation plots by tsunami zone and 300, 975, 2500, and 5000 year maps.

The first step in the PTHA analysis is to specify a suite of seismic sources, including estimates of their mean inter-event time T_M and a Poisson rate $\mu = 1/T_M$. Then the GeoClaw tsunami model (see Section 5 for a description and validation studies of this model) is used to simulate generation, propagation and inundation corresponding to each seismic source, and a database is created of hazard indices, such as maximum flow depth, current velocity, and momentum flux on a fine resolution bathymetric/topographic grid of the Crescent City area. Actually five GeoClaw simulations are performed for each source, with five different static background water levels, in order to incorporate tidal uncertainty as described in Section 8. The database is then subjected to post-processing that creates a tsunami hazard curve at each position (x, y) of the Crescent City inundation grid. Each hazard curve provides probability of exceedance estimates for specific hazard index values that are then contoured and displayed in graphical form. Each of these steps is discussed in more detail below.

Figures 1 and 2 show Google Earth images of Crescent City at two scales. For this study the full region shown in Figure 1 has been studied, though many plots show only the downtown and harbor region seen in Figure 2 since many events do not inundate beyond this region. Figure 2 also shows 6 synthetic gauge locations that are referred to in some later figures.

In each GeoClaw run, adaptive mesh refinement is used so that a range of different grid resolutions are used in different regions (as discussed more in Section 5), but in all cases the region shown in Figure 1 is refined to a resolution of 2/3 arc-second on the finest computational grid. Periodically during the computation (every 30 seconds for most events, but more frequently for CSZ where the first wave is more sharply peaked), results from this grid are interpolated to a finer 1/3 arc-second grid that covers the region of Figure 1 in order to monitor the maximum flow depth observed over the full computation at each point on the grid. The result of each run is a record of the maximum flow depth values at each point on a 865×541 grid (467965 grid points) covering the region of Figure 1, between longitude 235.77 and 235.85 degrees East, and between latitudes 41.735 and 41.785 degrees North. We use east longitude coordinates since the full computational domain often extended west of longitude 0, and we also wanted to use positive coordinates increasing from west to east.

2.5 Bathymetry and topography data

The bathymetric and topographic Digital Elevation Models (DEMs) used are the ETOPO1 global and Crescent City region grids, available online at the NOAA/NGDC website

http://www.ngdc.noaa.gov/dem/squareCellGrid/search.

A detailed description of the development of each, including the underlying bathy/topo source data and quality are provided in [5] and [24].

ETOPO1 global bathymetry with a resolution of 1 arc-minute (approximately 2 km) was used over the ocean. This uses horizontal datum WGS84 and vertical datum MSL. For some farfield runs subsampled data at 4 arc-minute resolution was used, consistent with the finest level grids used over most of the ocean. These datasets were obtained from

http://www.ngdc.noaa.gov/mgg/gdas/gd_designagrid.html.

For the region around Crescent City, 1/3 arc-second (approximately 7.5 m by 10m resolution) bathymetry was used, obtained from

http://www.ngdc.noaa.gov/dem/squareCellGrid/download/693.

This uses horizontal datum WGS84 and vertical datum MHW. This was used for longitude 235.7655 to 235.84 and latitude 41.71643 to 41.7695.

Subsampled 1 arc-second (approximately 22.5 m by 30 m) bathymetry was used for a larger region around Crescent City, from longitude 235 to 236 and latitude 41.42 to 42.1.

Onshore topography is bare earth, with no structures. The onshore topography in the Crescent City region is referenced to MHW, so $B = 0$ in contour plots corresponds to MHW, which is roughly 0.77 m above MSL.
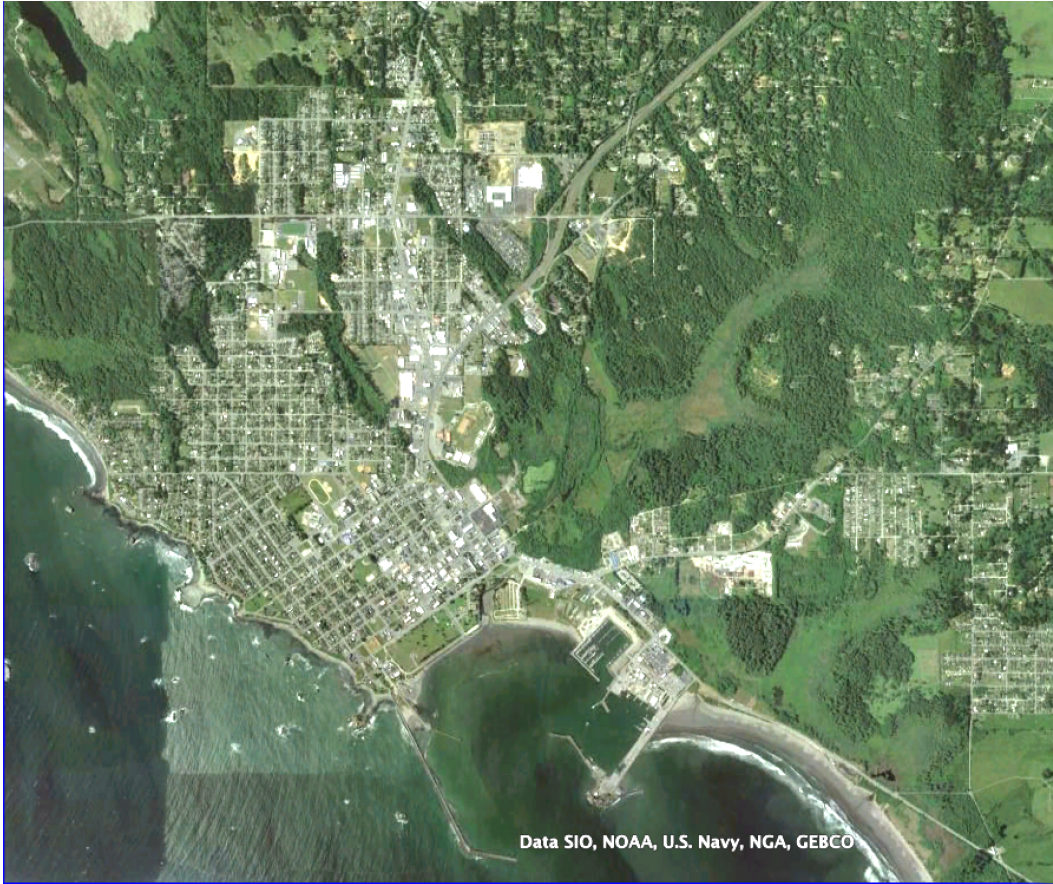
Figure 1: Google Earth view of Crescent City. This is the region used for the study and maximum inundation for each each run is recorded at every point on a 1/3 arc-second resolution grid covering this region.
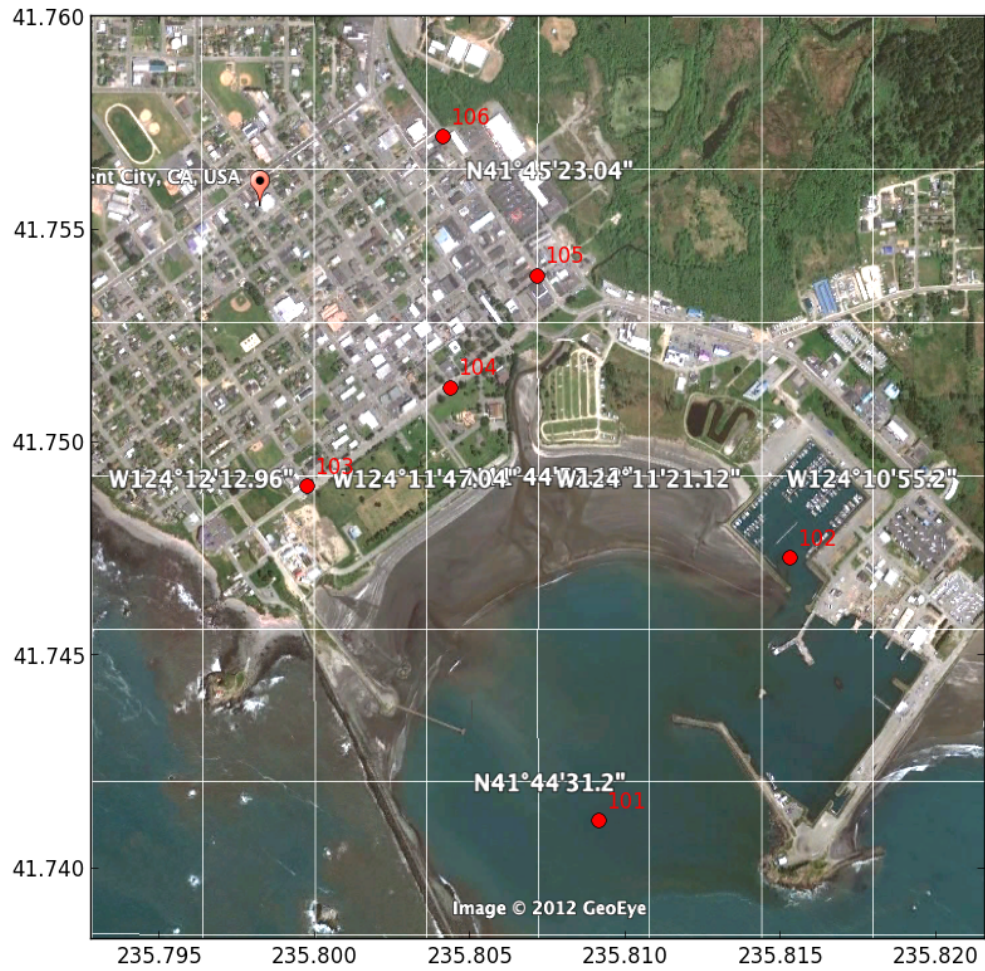
Figure 2: Zoom view of the harbor and downtown region. Gauges 101 through 106 in the computational results present below are indicated in this figure.

2.6 Notation and terminology

The following notation and terminology is used throughout this report.

- All depths and elevations are report in meters, since this is the convention for all datasets used.

- h refers to the water depth above topography or bathymetry. It is one of the primary variables of the shallow water equations.

- B refers to topography or bathymetry as specified by the topography datasets, and is relative to MHW since that is the vertical datum of the fine scale Crescent City bathymetry. Some CSZ events cause a change in the bathymetry in the Crescent City region (uplift or more typically subsidence). The plots are all presented relative to the pre-earthquake bathymetry.

- $\eta = B + h$ is the surface elevation relative to MHW.

- ζ will be used to denote the maximum observed value over the full time period of a tsunami of either h or $B + h$:

$$\zeta = \begin{cases} h, & \text{the flow depth, in regions where } B > 0 \text{ (onshore),} \\ B + h, & \text{the sea surface elevation, in regions where } B < 0. \end{cases} \tag{1}$$

  Inundation and hazard maps generally show ζ. The sea surface elevation is relative to MHW.

- The flow speed is defined by $s = \sqrt{u^2 + v^2}$, where u and v are the depth-averaged velocities in the E-W and N-S directions, respectively. In the shallow water equations that GeoClaw solves, the momenta hu and hv are two of the quantities computed and u and v are determined by dividing by h, the fluid depth.

- The term *momentum flux* in this work refers to the quantity $h(u^2 + v^2)$, which can be computed directly from the variables of the shallow water equations. This quantity has units of m^3/s^2. The more proper physical momentum flux can be obtained by multiplying this by by 1.8 (1000 kg / m^3) to obtain force per unit length normal to the flow direction, in units of kN/m as described in detail in Appendix E.

- ξ denotes the tide stage, relative to MSL. With GeoClaw we can run the code with sealevel set to different values and this is used in the way we handle tidal uncertainty.

- Tsunami sources we used will generally be denoted in the form AASZe03, for example, which refers to event number 3 on the Alaska Aleutian Subduction Zone. Many events, such as AASZe03, have only one *realization* (model for how slip is distributed on the fault plane, and/or the resulting seafloor deformation). Some events, e.g. a CSZ Mw 9.1 event, have multiple possible realizations. For the CSZ event in Phase I, we used the 15 Bandon sources, see Witter, et.al. [61], as 15 realizations of one CSZ event, and refer to them as CSZBe01r01 – CSZBe01r15. In this study, we use these same 15 that have been adjusted as described in Section 7.6, and refer to them as CSZRe01r01 – CSZRe01r15. To these 15, we add two more realizations as described in Section 7.6 and refer to them as CSZRe01r16 and CSZRe01r17.

  In the probabilistic modeling we typically assign a recurrence time to the event and then a conditional probability to each realization of the event. If there is only one realization of the event, its conditional probability is 1.

2.6.1 Probabilities, rates, and recurrence times

By *probability of an event* we generally mean *annual probability of occurrence*. Specific earthquake events are often assumed to be governed by a Poisson process with some *mean recurrence time T_M*, in which case the annual probability of occurrence is $p = 1 - e^{-\nu}$ where the *rate* is $\nu = 1/T_M$. If ν is small then $p \approx \nu$ with an error that is $O(\nu^2)$. For example, if $T_M = 250$ then $\nu = 0.004$ and $p = 0.003992$. For larger T_M there is even less error. Since T_M is not accurately known, it is generally fine to assume $p = 1/T_M$.

When calculating the probability that one of several possible events might happen, some care is required. If two independent events are considered with annual probabilities p_1 and p_2 then the annual probability of at least one of them occurring is

$$p_{12} = 1 - (1 - p_1)(1 - p_2) = p_1 + p_2 - p_1 p_2.$$

If both probabilities are very small then $p_{12} \approx p_1 + p_2$ but for larger probabilities the more accurate expression must be used. Similarly, if we are interested in the probability of any one of N independent events occurring, the probability is

$$p_{1\ldots N} = 1 - (1 - p_1)(1 - p_2) \cdots (1 - p_N) \approx p_1 + p_2 + \cdots + p_N$$

Again simply adding the probabilities is valid only if the result is much less than one, but otherwise not.

Note that when expressed in terms of Poisson rates, it is valid to add the rates: if $p_i = 1 - e^{-\nu_i}$ then $p_{1\ldots N}$ has rate $\nu_1 + \nu_2 + \cdots + \nu_N$ since

$$p_{1\ldots N} = 1 - e^{-\nu_1} e^{-\nu_2} \cdots e^{-\nu_N} = 1 - e^{-(\nu_1 + \cdots + \nu_N)}.$$

3 Probabilistic results

The deliverable maps of this study are the "100 year" and "500 year" flood maps for wave heights (η), flood depth (ζ), speed, and momentum flux. These products for the wave heights are given in Appendix C since they are a simple modification of the quantity ζ. In the body of this report we focus mainly on ζ, speed, and momentum flux, and the maps for these quantities of interest are shown below. They were computed as described in the remainder of this report, using all the earthquake sources of Section 7 and taking into account tidal uncertainty using the Pattern-Method described in [3] and summarized in Section 8.

3.1 The 100 year flood: ζ, speed, and momentum flux contours for $p = 0.01$

Figures 3, 4, and 5 show contours of ζ, speed, and momentum flux corresponding to $p = 0.01$, respectively. Recall from Section 2.6 that ζ is the maximum depth of fluid at on-shore points that are inundated, and is the maximum elevation above MHW for points offshore.

Each point in the region of a given color has an annual probability of 0.01 of inundation above the corresponding ζ, speed, or momentum flux value. These are determined by examining the respective hazard curve of each point and determining what value of ζ, speed, or momentum flux corresponds to $p = 0.01$. The outer limits of the area colored thus show the limits of the "100-year flood" for the respective quantity of interest.

Figure 3: ζ-contours for p=.01. This product was created using all the study sources in Table 1. This includes CSZ with recurrence time $T_M = 250$ years and a representative Japan source with recurrence time $T_M = 103$ years. Note that ζ is the flow depth onshore and the height above MHW offshore, measured in meters.

Figure 4: speed-contours for p=.01. This product was created using all the study sources in Table 1. This includes CSZ with recurrence time $T_M = 250$ years and a representative Japan source with recurrence time $T_M = 103$ years. Note that speed is measured in meters per second m/s.

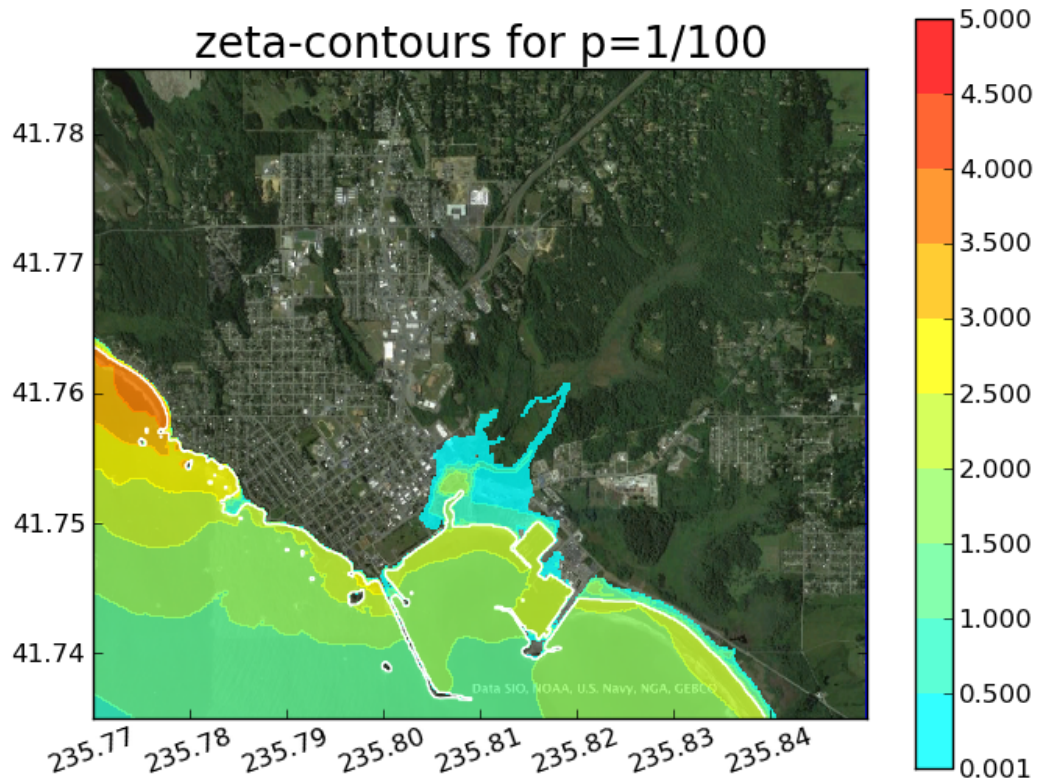Figure 5: Momentum flux contours for p=.01. This product was created using all the study sources in Table 1. This includes CSZ with recurrence time $T_M = 250$ years and a representative Japan source with recurrence time $T_M = 103$ years. Recall that "momentum flux" in this work is measured in m^3/s^2 (See Section 2.6). For conversion to kN/m multiply the numbers on the colorbar by 1.8 as described in Appendix E.

3.2 The 500 year flood: ζ, speed, and momentum flux contours for $p = 0.002$

Similarly, Figure 6, Figure 7, and Figure 8 show contours of ζ, speed, and momentum flux corresponding to $p = 0.002$, respectively. Each point in the region of a given color has an annual probability of 0.002 of inundation above the corresponding ζ, speed, or momentum flux value. These are determined by examining the respective hazard curve of each point and determining what value of ζ, speed, or momentum flux corresponds to $p = 0.002$. The outer limits of the area colored thus show the limits of the "500-year flood" for the respective quantity of interest.

Figure 6: ζ-contours for p=.002. This product was created using all the study sources in Table 1. This includes CSZ with recurrence time $T_M = 250$ years and a representative Japan source with recurrence time $T_M = 103$ years. Note that ζ is the flow depth onshore and the height above MHW offshore, measured in meters.
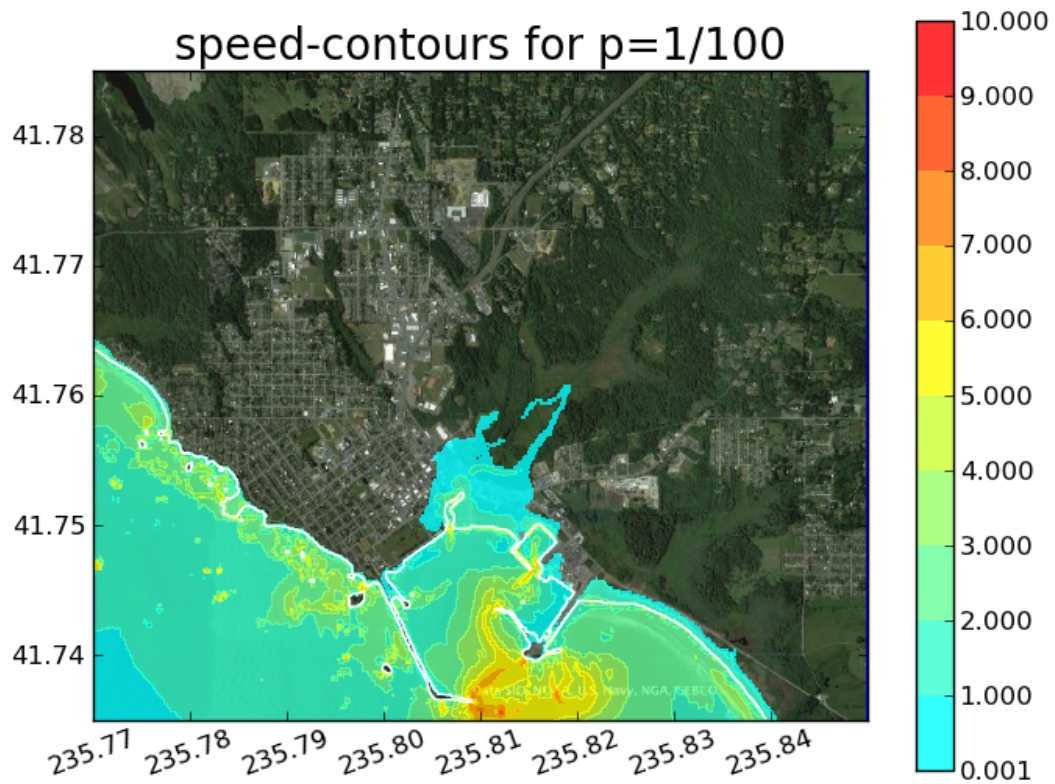
Figure 7: speed-contours for p=.002. This product was created using all the study sources in Table 1. This includes CSZ with recurrence time $T_M = 250$ years and a representative Japan source with recurrence time $T_M = 103$ years. Note that speed is measured in meters per second (m/s).
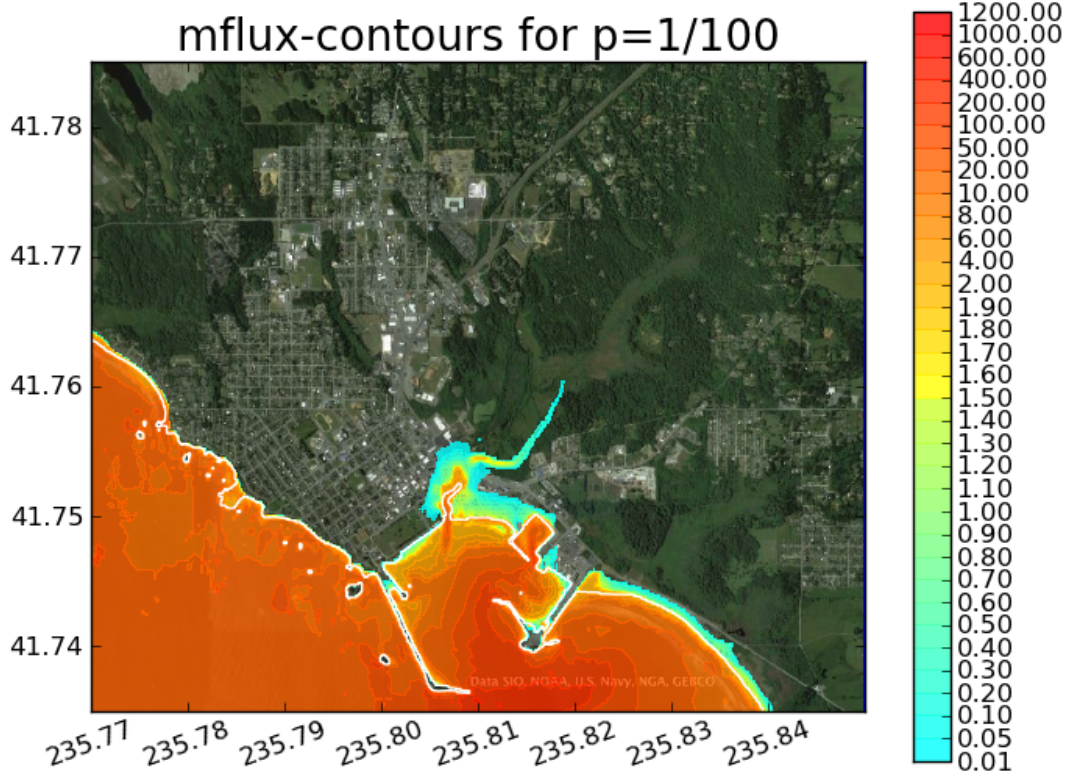
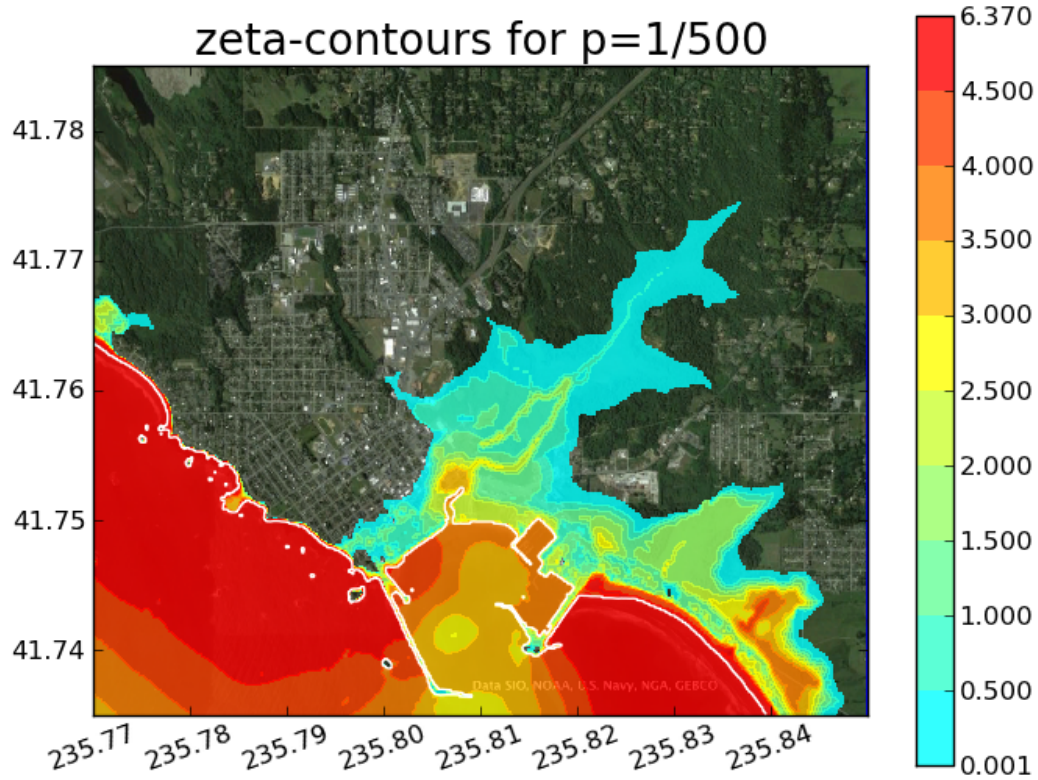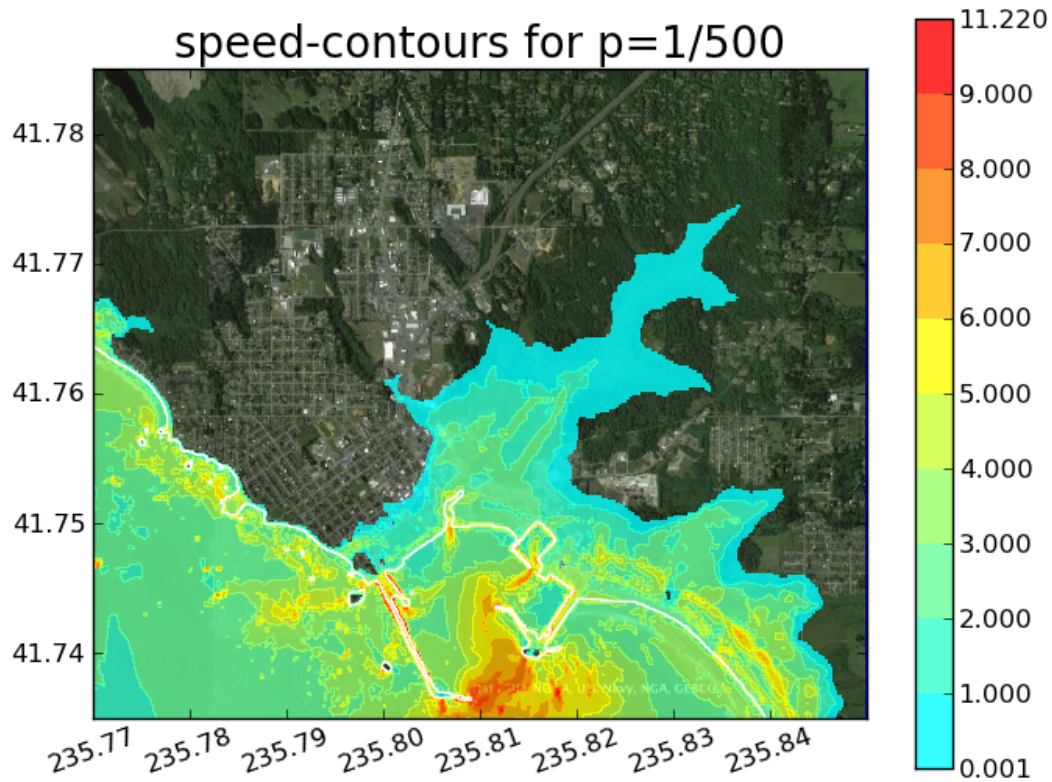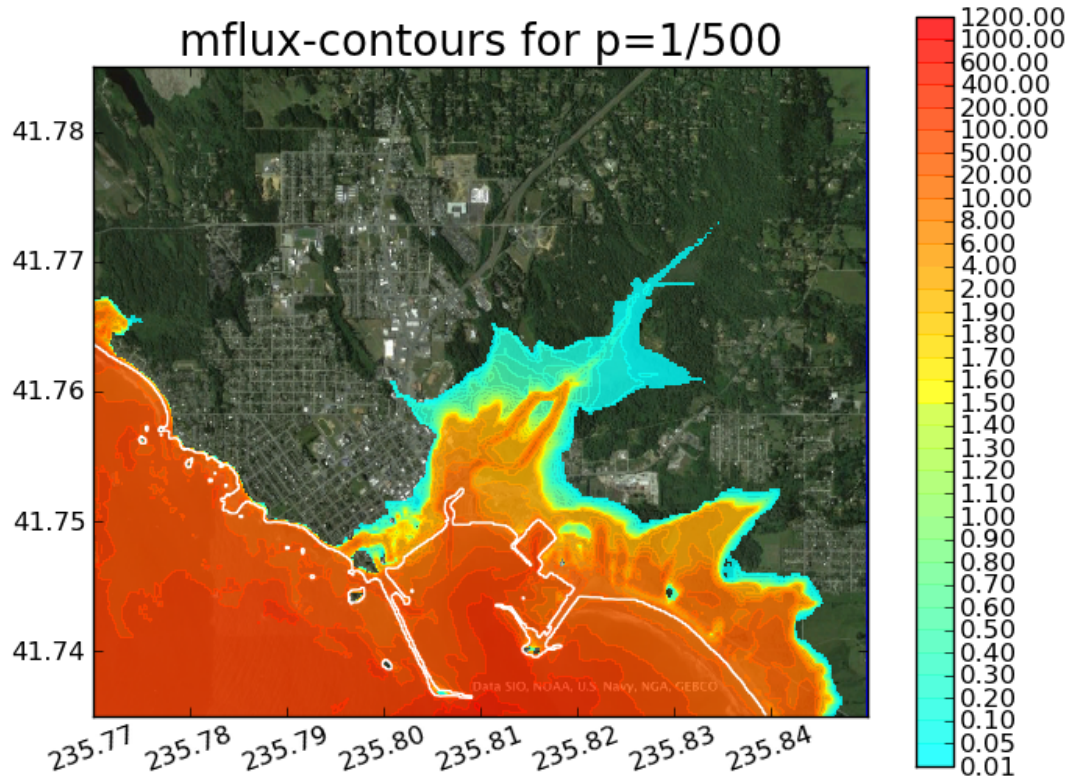Figure 8:   mflux-contours for p=.002. This product was created using all the study sources in Table 1. This includes CSZ with recurrence time $T_M = 250$ years and a representative Japan source with recurrence time $T_M = 103$ years. Note that momentum flux is measured in m^3/s^2 (See Section 2.6). For conversion to kN/m multiply the numbers on the colorbar by 1.8 as described in Appendix E.

These deliverable maps are specified as the desired results of this probabilistic study. Only looking at such maps may be misleading — the inundated region can be very sensitive to the probability levels chosen for display, or to the parameters used in the modeling, such as the recurrence time of one event. In Section 9.2 we show an example of this. We believe that it is possible to present the results of a probabilistic study in ways to convey additional information, and offer some suggestions in Section 9.2.

3.3   Hazard curves

The maps shown above and other probabilistic products described later are based on *hazard curves* that are constructed from the results of all individual GeoClaw runs over all the tsunami sources considered. Figure 9, Figure 10, and Figure 11 show typical hazard curves at four (x, y) points corresponding to the locations of Gauges 101, 103, 104, and 105 in Figure 2 for ζ, speed, and momentum flux, respectively. The horizontal axis in Figure 9 shows ζ as defined in Section 2.6, so it is the surface elevation above MHW at Gauge 101 and the flow depth at the other three locations. The vertical axis is *probability of exceedance*. At each ζ the corresponding $p(\zeta)$ approximates the annual probability of exceeding this value, at the particular (x, y) point. The horizontal axis in Figure 10 and Figure 11 are the speed and momentum flux, respectively.

These plots are generated as described in the following sections, and include tidal uncertainty as well as the probabilities of different earthquake events.

At Longitude, Latitude, Bathy: (235.8092, 41.7412, -7.0419)

At Longitude, Latitude, Bathy: (235.7998, 41.7490, 2.2815)

At Longitude, Latitude, Bathy: (235.8044, 41.7513, 2.0752)

At Longitude, Latitude, Bathy: (235.8073, 41.7539, 0.5435)
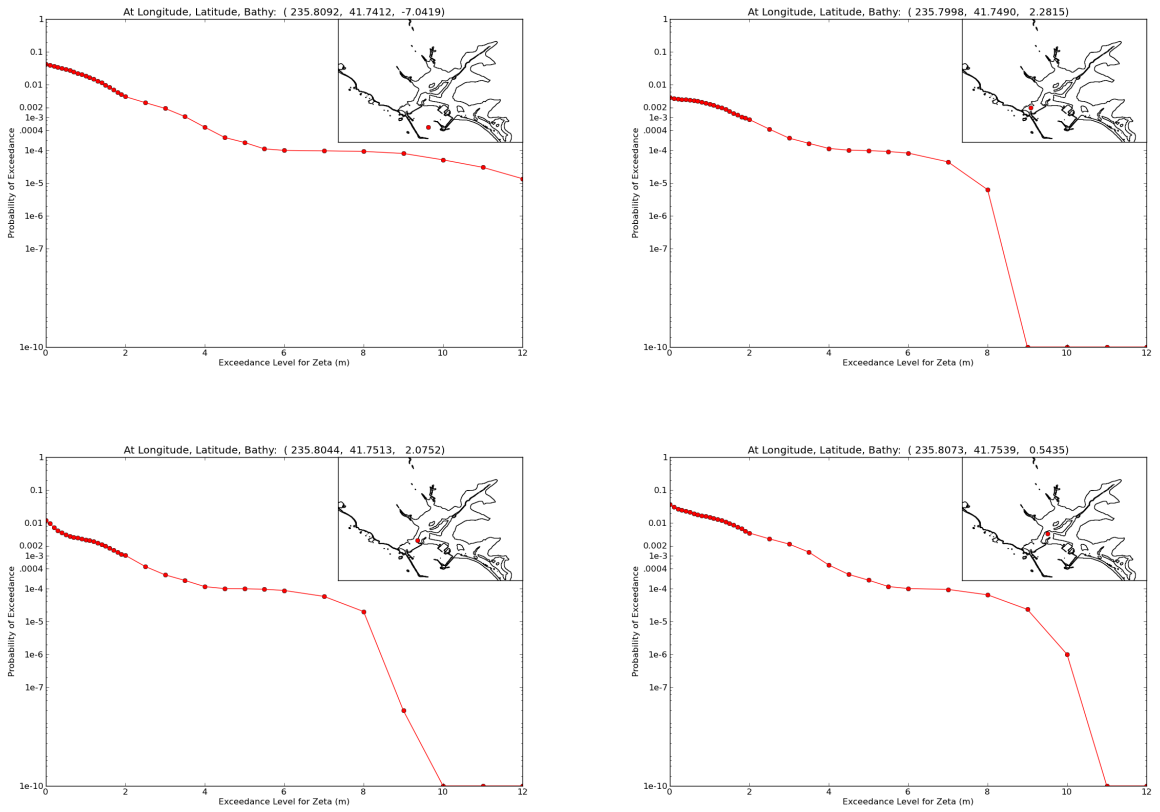
Figure 9: Sample hazard curves for ζ at four locations, Top: Gauges 101, 103; Bottom: Gauges 104, and 105 from Figure 2. Note that Gauge 101 is in the harbor, so ζ refers to the elevation above MHW. The other gauges are onshore and ζ refers to flow depth.

Figure 10: Sample hazard curves for speed at four locations, Top: Gauges 101, 103; Bottom: Gauges 104, and 105 from Figure 2.
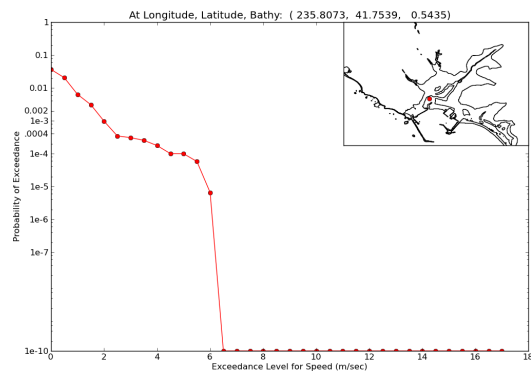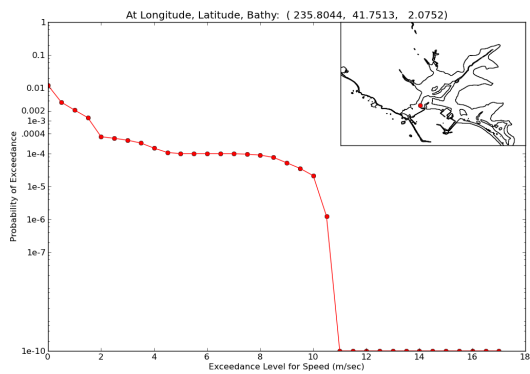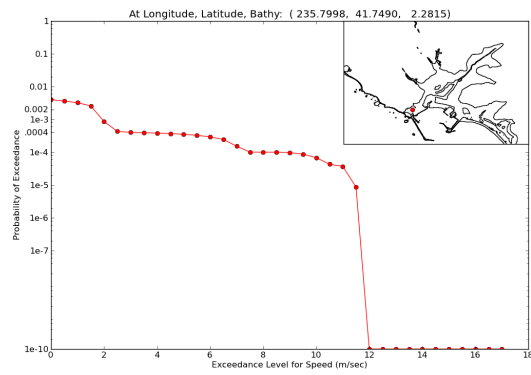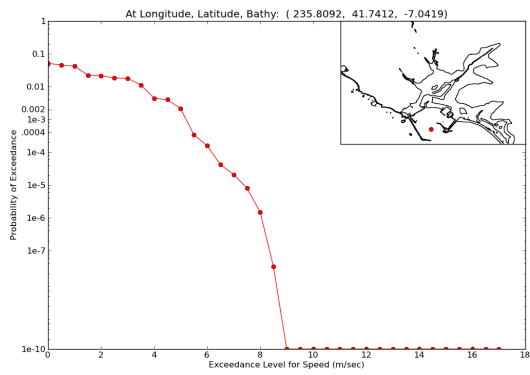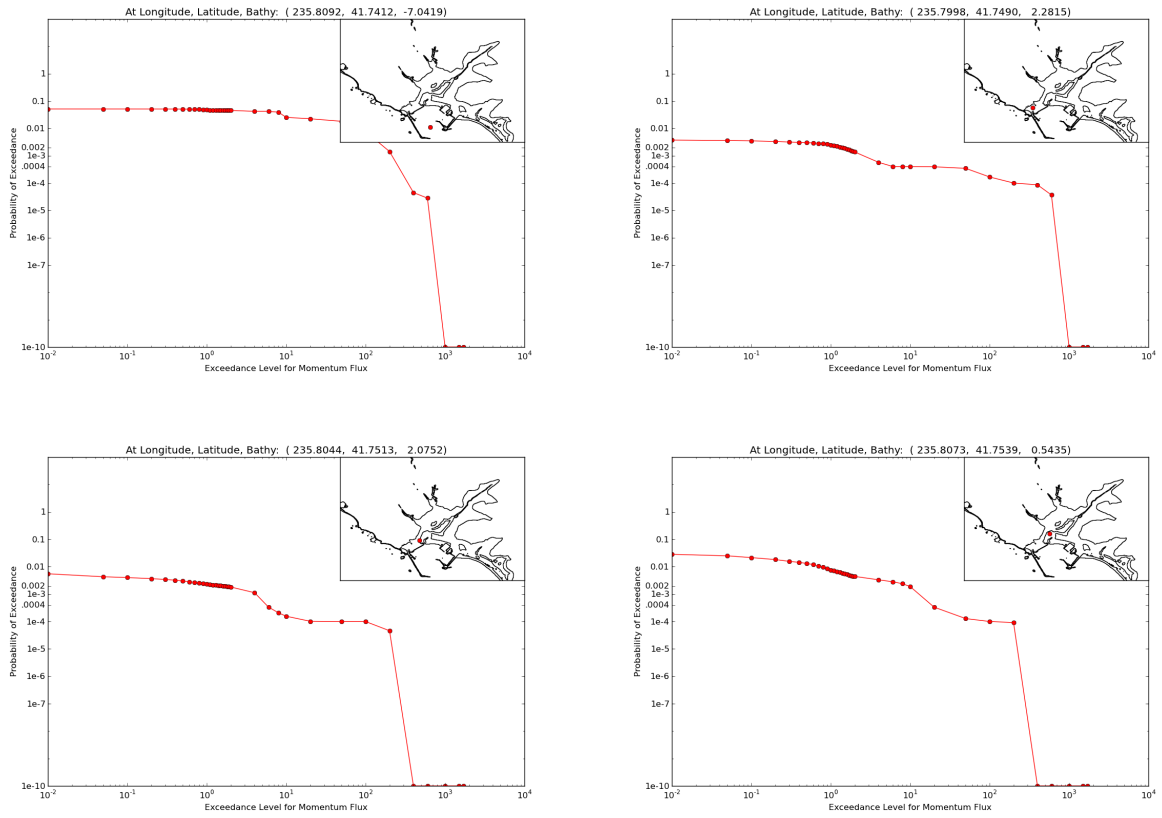
Figure 11: Sample hazard curves for momentum flux at four locations, Top: Gauges 101, 103; Bottom: Gauges 104, and 105 from Figure 2.

4   Sources of uncertainty

There are many sources of uncertainty that must feed into any probabilistic model of tsunami hazards. It is useful to distinguish between *epistemic* and *aleatoric* uncertainties, although it is not always possible to neatly divide all sources of uncertainty into one of these categories.

Aleatoric uncertainty refers to uncertainty due to the inherent randomness of the processes generating tsunamis. We can never know exactly when or where the next major earthquake will occur or how large it will be, let alone the details of the slip pattern on the fault that can affect the resulting inundation patterns. However, if we assume that we know suitable probability distributions (e.g. that one of a finite number of characteristic earthquakes might occur, and that they occur according to a Poisson process with known recurrence time), then we can use these probability distributions for the inputs in order to generate probability distributions of inundation at points in a community. There are challenges to doing this accurately and efficiently, but the desired output is a well defined probability distribution.

Epistemic uncertainty refers to uncertainty due to lack of knowledge of the underlying processes, which means we do not know the correct probability distributions for the inputs (and hence can't hope to produce the correct probability distribution for the output). For example, in general it is not known what the correct probability distribution is for how the slip might be distributed over the fault geometry. The fault geometry itself may not be well known. The time series of events is not simply a Poisson process and it is not even known what the correct mean recurrence time is in general for any particular event.

One can make a guess at what the right probability distribution is, or consider several possible probability distributions with some weighting. Doing the latter appears to reduce the epistemic uncertainty to another form of aleatoric uncertainty and may be useful in practice, but the philosophical difference is that epistemic uncertainty could in principle be eliminated if we had more information about the system. There is some correct probability distribution of possible events and if we could observe earthquakes for millions of years (and if the geophysical processes were time invariant) it might be possible to estimate the parameters describing this distribution arbitrarily well. On the other hand even if we knew the probability distribution exactly we would not have eliminated the aleatoric uncertainty described by this distribution — we still would not know which sample from this distribution the next earthquake will be or when it will occur.

Sources of uncertainty in PTHA include the following:

- Earthquake sources: This is a major source of uncertainty, and as discussed above there are large epistemic uncertainties in choosing the correct probability distribution of possible events. This is discussed in more detail in the coming sections.

- Tide stage: For a given earthquake and resulting tsunami, the extent and depth of inundation in Crescent City can vary greatly depending on whether the waves arrive at high tide or low tide. Since the earthquake might occur at any time in the tidal cycle with equal probability, this is a form of aleatoric uncertainty. There is little epistemic uncertainty since the probability that the tide will be greater than a given level at a random time can be estimated very well by past tidal records and/or from the harmonic constituents that describe the expected future tides. There are still challenges in determining the best approach to incorporating this aleatoric uncertainty into the PTHA that are discussed further in Section 8. This is particularly interesting for earthquake sources where the resulting tsunamis consists of several large waves that hit Crescent City many hours apart, and for which the tide may change significantly in between. The range of the tide stage used in this report is described in Section 8.

- Sea level rise: In this report we have used topography and bathymetry data relevant for current sea level. If the resulting hazard maps are to be used for many years to come, perhaps the expected rise in sea level over the time horizon of interest should also be taken into account.

- Quality of bathymetry and topography data. The ocean bathymetry used comes from the ETOPO1 data set, which provides 1 arc-minute resolution (about 2 km) over the entire Pacific Ocean. This

is thought to be sufficiently accurate for our needs. Near Crescent City, 1 arc-second and 1/3 arc-second data is used as described in Section 2.5. This has sufficient spatial resolution, but there is some uncertainty regarding whether the vertical elevation data is adequate for detailed modeling in Crescent City. In particular, the data used gives the topography of "bare earth", without buildings or other structures. In reality inundation of the city center would entail water flowing through the streets and around many buildings. This will surely change the inundation patterns. To some extent this uncertainty can be investigated by running the simulations with different bottom friction (Manning) coefficients. We have always used Manning coefficient $n = 0.025$, a commonly used value for tsunami modeling, which is appropriate for gravelly earth.

- Tsunami model: The GeoClaw numerical model is thought to be suitably accurate, as discussed in Section 5. However, it does not solve the shallow water equations exactly and so the computed solutions have errors relative to the true solution of these equations. Moreover the shallow water equations are not a perfect model of the fluid dynamics, so even the exact solution of these equations would not agree with the actual inundation from the event being modeled. The errors introduced in modeling and numerical simulation can also be considered as uncertainties in the predicted inundation patterns. In principle one could attempt to include this uncertainty in a probabilistic model. For example, by studying the difference between numerical results and actual observations from many past events it might be possible to estimate the probability distribution of differences between the two. However, this is complicated by the fact that the earthquake source for past events is generally not known with great precision, so it is hard to separate the error due to the numerical model from the error due to the incorrect specification of the tsunami source.

  In this study we have not attempted to include uncertainty due to the mathematical or numerical model of the shallow water equations. However, we have done studies in which key parameters such as the mesh sizes have been varied in order to verify that our solutions are essentially converged. Together with past validation studies of various shallow water codes we feel fairly confident that the errors due to the modeling are relatively small compared to the uncertainty in the sources used.

5 The GeoClaw tsunami model

5.1 Overview of code and methods

The GeoClaw tsunami model is a branch of the Clawpack open source software package, and is available via the website www.clawpack.org/geoclaw. Clawpack (Conservation Laws Package) was first released by LeVeque in 1994 and the package has been extensively developed and improved over the years. Clawpack is a general package for solving linear and nonlinear hyperbolic systems of partial differential equations, including the important class of nonlinear conservation laws, whose solutions typically contain shock waves and other discontinuities. Robust shock capturing methods are used that are designed to handle strong shock waves. These methods are described in detail in [30].

GeoClaw was originally named TsunamiClaw and originated out of the PhD dissertation of David George [17], completed in 2006. The code has since been further developed for tsunami modeling, and has also been adapted to solve other geophysical flow problems using two-dimensional depth-averaged systems of equations.

For tsunami modeling, the two-dimensional shallow water equations (also called the St. Venant equations) are solved. This system of equations is commonly used for modeling tsunami propagation and inundation, and is also the system of equations solved by other models such as MOST (Method of Splitting Tsunamis) [53].

The shallow water equations (SWE) are a nonlinear depth-averaged system of partial differential equations in which the fluid depth $h(x, y, t)$ and two horizontal depth-averaged velocities $u(x, y, t)$ and $v(x, y, t)$ are introduced. These equations are written in a form that corresponds to conservation of mass and momentum

whenever the terms on the right hand side vanish:

$$h_t + (hu)_x + (hv)_y = 0,$$

$$(hu)_t + \left(hu^2 + \frac{1}{2}gh^2\right)_x + (huv)_y = -ghB_x - Dhu, \qquad (2)$$

$$(hv)_t + (huv)_x + \left(hv^2 + \frac{1}{2}gh^2\right)_y = -ghB_y - Dhv.$$

Subscripts denote partial derivatives. The momentum source terms on the right hand side involve the varying bathymetry $B(x, y, t)$ and a frictional drag term, where $D(h, u, v)$ is a drag coefficient given by

$$D(h, u, v) = n^2 g h^{-4/3} \sqrt{u^2 + v^2}. \qquad (3)$$

The parameter n is the *Manning coefficient* and depends on the roughness. For tsunami modeling a constant value of $n = 0.025$ is often used and we have adopted that value for much of this work, following standard practice.

Coriolis terms can also be added to the right hand side of equations (2), but these generally have been found to be negligible in tsunami modeling. We have performed some of our computations both with and without the Coriolis terms and have confirmed this for the case of inundation in Crescent City.

The finite volume methods implemented in GeoClaw are based on dividing the computational domain into rectangular grid cells and storing cell averages of mass and momentum in each grid cell. These are updated each time step by a high-resolution Godunov type method [30] that is based on solving Riemann problems at the interfaces between neighboring grid cells and applying nonlinear limiters to avoid nonphysical oscillations. These methods are second order accurate in space and time wherever the solution is smooth, but robustly handle strong shock waves and other discontinuous solutions. This is important when the tsunami reaches shallow water and hydraulic jumps arise from wave breaking.

The methods have been extended to also deal robustly with inundation. Grid cells where $h = 0$ represent dry land. Cells can dynamically change between wet and dry each time step. The grid resolution near Crescent City is taken to be sufficiently fine that the shoreline and edge of the inundated region can be well approximated by the edge of the wet region.

Block structured adaptive mesh refinement (AMR) is used to employ much finer grid resolution in regions of particular interest. Regions of refinement track the tsunami as it propagates across the ocean and then additional levels of refinement are added around the coast of California and in the Crescent City region. We typically use 6 levels of refinement going from a coarse grid with $2°$ resolution covering much of the Pacific Ocean on Level 1, to the finest Level 6 having resolution of 2/3" in the region shown in Figure 1.

5.2   Grid refinement studies

Some events have been simulated at two different grid resolution as a way to verify that the grid being used is sufficiently fine to capture a converged solution of the shallow water equations. Figure 12 shows one such comparison, in which the top row is computed with 2/3" resolution on the finest level (as has been done in our production runs). The results are then interpolated onto a 1/3" grid for plotting purposes and to compute the probabilistic results on this finer grid. The bottom row shows results if the finest level covering Crescent City is instead refined to 1/3". These results suggest that there would be little to be gained by solving on the finer grid. These results are from Phase 1. We include them here for completeness, but see no need to rerun the experiment again.
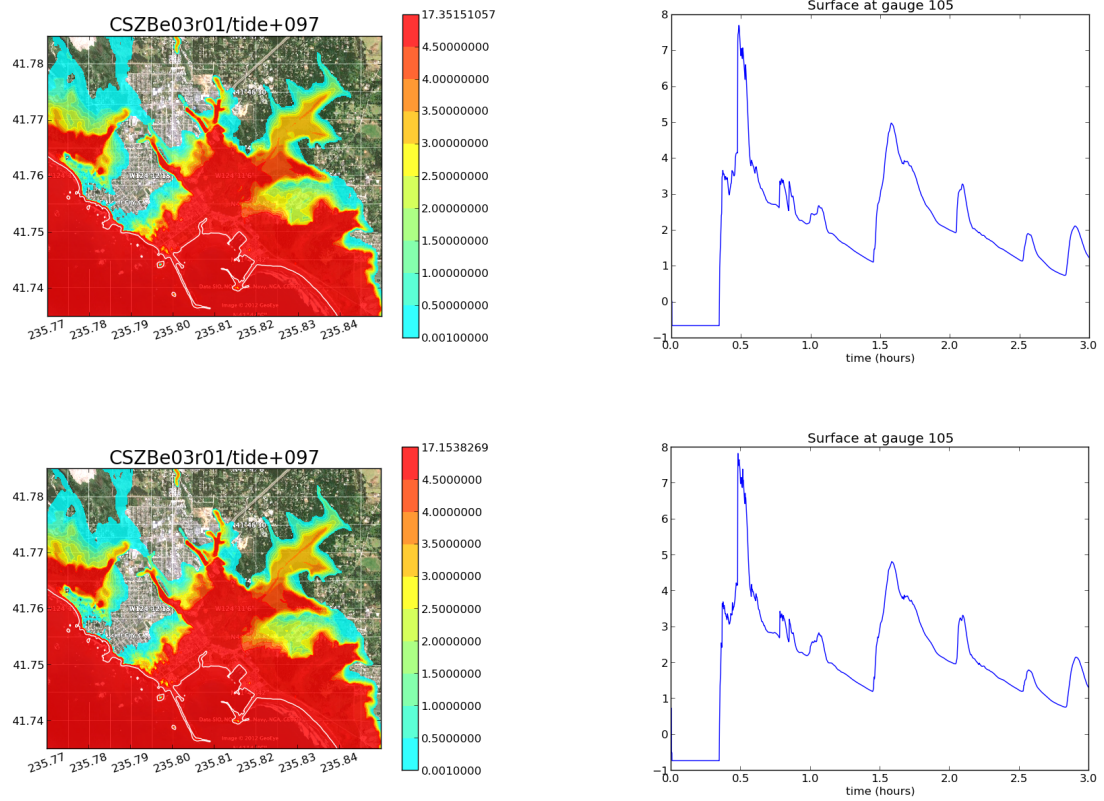
Figure 12: Results of one event realization CSZBe03r01 computed with two different fine grid resolutions. The top figures are using a 2/3" grid and the bottom is refined to 1/3". In each case the figure on the right is the depth as a function of time at gauge 105 from Figure 2.

5.3 Past validation studies

The GeoClaw model has undergone extensive verification and validation tests for tsunami modeling, as reported in [7, 11, 32, 21, 35, 31]. (*Verification* means confirming that the mathematical model equations are being solved correctly and accurately, while *validation* refers to investigating how well the solution of these equations agrees with reality.) Most of these papers and many simulation results can be found on the GeoClaw webpage, http://www.clawpack.org/geoclaw.

In particular, the GeoClaw model was extensively tested as part of a benchmarking workshop sponsored by the U.S. National Tsunami Hazard Mitigation Program (NTHMP) in 2011 [21, 42]. Nine tsunami benchmark problems were solved and the solutions compared at the workshop, and by the committee responsible for approving numerical models for NTHMP funded work. As a result of successful completion of the benchmark problems, the GeoClaw model has been approved by the NTHMP.

The benchmarks included comparison to analytic solutions, wave tank experiments, and one historical event, the 1993 tsunami that struck Okushiri Island.

Data from the Tohoku event of 11 March 2011 have recently been used to further validate the GeoClaw model, funded in part by an NSF RAPID grant awarded for this purpose. In one study [35], ten different proposed tsunami sources were used together with GeoClaw tsunami modeling to compare against several sets of observations. Five DART buoys were considered, along with comparison of the computed and observed inundation on the Sendai Plain and at four other locations along the Sanriku Coast of Japan (north of Sendai). Comparisons of GeoClaw results to the observed tide gauge measurements in Crescent City during this event are shown in Figure 16 for one of these sources.

Current gauges deployed near Hawaii recorded the Tohoku event. Ten of these gauges (in Honolulu, Kahului, and Hilo harbors and several inter-island channels) were used in a study by Arcos and LeVeque [7] to validate the GeoClaw model. Excellent agreement was observed at the inter-island channels and reasonable agreement was also found in the harbors. That paper also contains a discussion of the extreme spatial variability of maximum velocities relative to maximum surface elevation. This is easy to observe in Figure 18 below: while the surface elevation is roughly constant in this photograph, there are very strong channelized currents resulting in changes in velocity by several m/s between two points that are separated by only a few meters. This makes it much more challenging for a numerical model to match computed to observed velocities at particular locations in a harbor, even when such data is available, than it is to match surface elevations, which are more spatially uniform.

6 Validation results for Crescent City

In this section we present some sample results obtained for Crescent City, both to clarify the methodology used in this study and to further validate the code for this application. We illustrate results for two events. The first is the earthquake source AASZe03, a model for the 1964 Alaska earthquake that caused substantial flooding in Crescent City. The second is the 11 March 2011 Tohoku event, which caused substantial damage in the harbor but little flooding onshore.

6.1 Results for Alaska 1964

This earthquake source AASZe03 is discussed further in Section 7.1. It is a model for the 28 March 1964 event that flooded parts of the city, as illustrated in Figure 13.

Figure 14 shows the results of the GeoClaw simulation. The color map shows values of ζ, which is defined as elsewhere in this report to be the maximum flow depth over the full computation at points on land, or the maximum surface elevation relative to MHW for points offshore, measured in meters. In comparing these results to Figure 13, several points must be kept in mind:

- The true earthquake source for this 1964 event is not well understood. The source AASZe03 is an approximation based on a crude model in which the roughly 600×100 km fault geometry was split into 12 rectangular fault segments (100×50 km each) and a uniform slip imposed on each. See Section 7.1 for more details. Because this may not be a good approximation to the true seafloor motion, it is not clear how well the simulated inundation should match the true inundation.

- The blue line in Figure 13 is the approximate inundation limit, but it is not known how accurate this is. In particular, in the Elk Creek valley the inundation does not appear to go nearly as far inland in this map as in the GeoClaw simulation, but this area is largely uninhabited and and it is not known how much effort was made to map this region.

- The Crescent City bathymetry has changed since 1964. In particular, the marina in our bathymetry did not exist in 1964.

In spite of these limitations, the inundation of the downtown region appears to be quite similar to that shown in Figure 13.
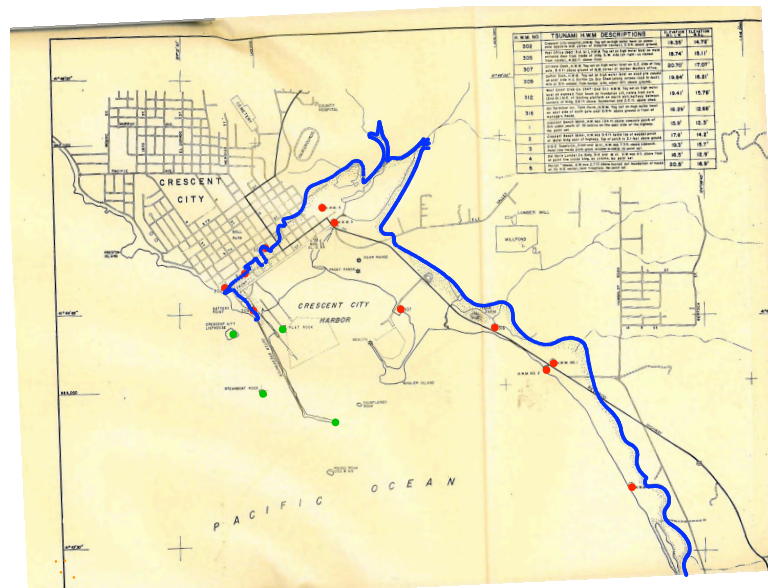

Figure 13: Inundation limits of the 1964 Alaska event tsunami, see Magoon [36].
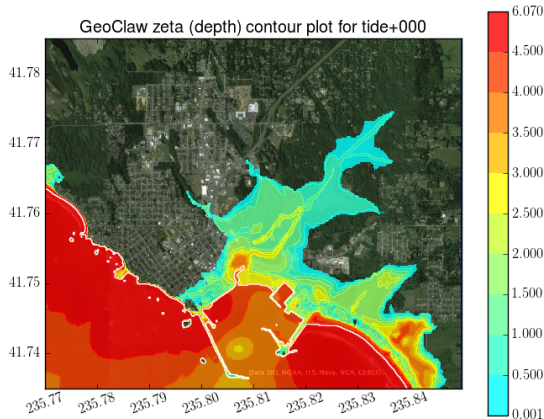
Figure 14: GeoClaw simulation results for the AASZe03 source, modeling the 1964 event. The maximum inundation depth is shown for a run at MSL.

6.2 Results for Tohoku 2011

Measurements of the 11 March 2011 Tohoku event in Crescent City provide some data that can be used for validation of the GeoClaw code. Figure 15 shows raw tide gauge data, illustrating that the largest waves arrived at low tide.

Wilson, et. al. [59] report that the Crescent City harbor experienced a maximum tsunami wave height of about 2.5 meters, and that the small boat harbor was nearly completely destroyed, at a cost of $20M. In spite of this loss, however, they report that significant runup did not occur.

The source model of G. Shao, et. al. [51] was selected as a representative model for this probabilistic study. MacInnes et al. [35] compared this source model to 9 others, and found that this one gave good agreement with many observations of both DART buoys and inundation along the coast of Japan. This is the source denoted TOHe01r03 in our probabilistic study, as discussed further in Section 7.5.

Figure 16 shows the tide gauge observations after detiding, along with the computed GeoClaw results obtained from runs at 6 different tide stages. The observations are shifted by 9 minutes so that the peaks line up better. The time shift can be largely explained by the lack of dispersion in the shallow water equations, as discussed in [7]. For each GeoClaw result, the vertical axis shows sea surface elevation relative to the initial surface level. These plots show quite good agreement of the surface elevation and indicate that the tsunami behavior at the tide gauge location is fairly insensitive to the tide stage used.

By contrast, current velocities can be much more sensitive to tide stage. Figure 17 shows a plot of the speed $s = \sqrt{u^2 + v^2}$ at the synthetic gauge 102 shown in Figure 2, inside the Small Boat Basin (SBB). Note that greater speeds are observed at lower tide stage than at higher tide stage. This is largely due to the fact that at higher tide the wave overtopped the breakwater bounding the SBB and so less water flowed through the entrance. However, this effect of lower tide stage leading to higher velocities has also been observed at many other points and complicates the incorporation of tidal uncertainty into the probabilistic analysis of currents, as discussed further in Section 8. There are no direct measurements of flow velocities in Crescent City harbor during this event, but analysis of video recorded has been used in [58] and [4] to estimate a peak velocity of roughly 4.5 m/s at the entrance to the SBB. Figure 18 shows one image of strong flow around the breakwater and into the SBB. Figures 19 and 20 show the maximum velocities recorded during GeoClaw runs at different tide stages. Figures 19 shows the runs at MLLW and MLW, which are most relevant for comparison since the tsunami arrived at low tide. The maximum near the SSB entrance is around 5–6 m/s.
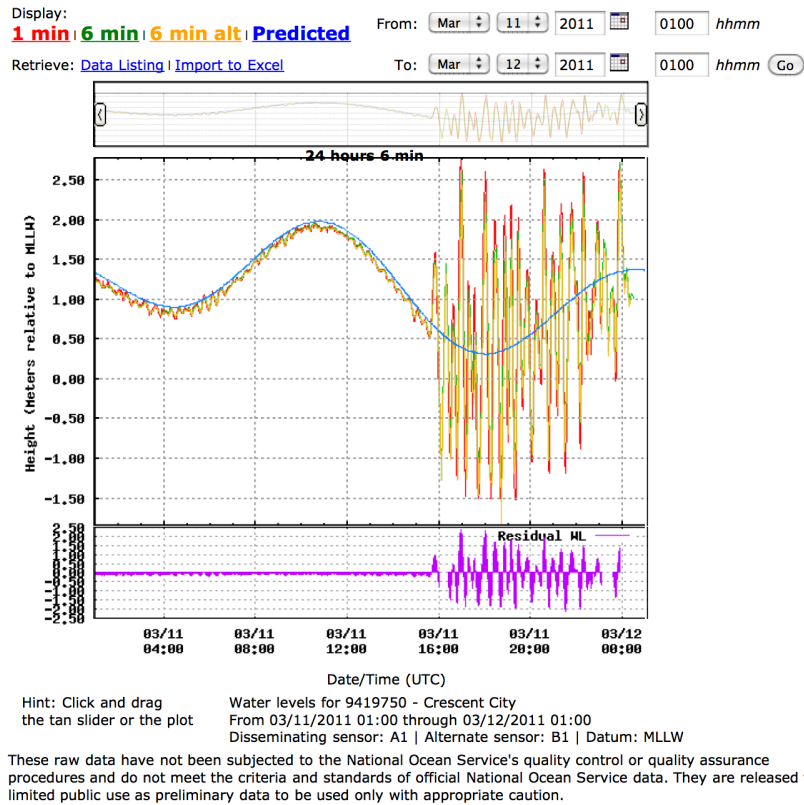
Figure 15: Raw data from Tide Gauge 9419750 at Crescent City during the Tohoku 2011 event. The first big waves arrived at low tide. The vertical scale is relative to MLLW, which is -1.13 m below MSL.
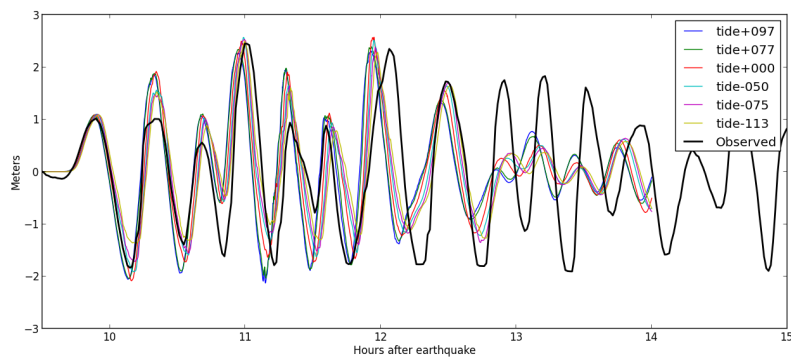
Figure 16: The thick black line is the observed surface elevation at Tide Gauge 9419750 after removing the tidal component and shifting by 9 minutes to better match the arrival time of the computational results. The simulated tide gauge data at the same point is shown in the other curves, as computed with different (fixed) tide levels and then shifted vertically so that 0 corresponds to the undisturbed surface in each case.
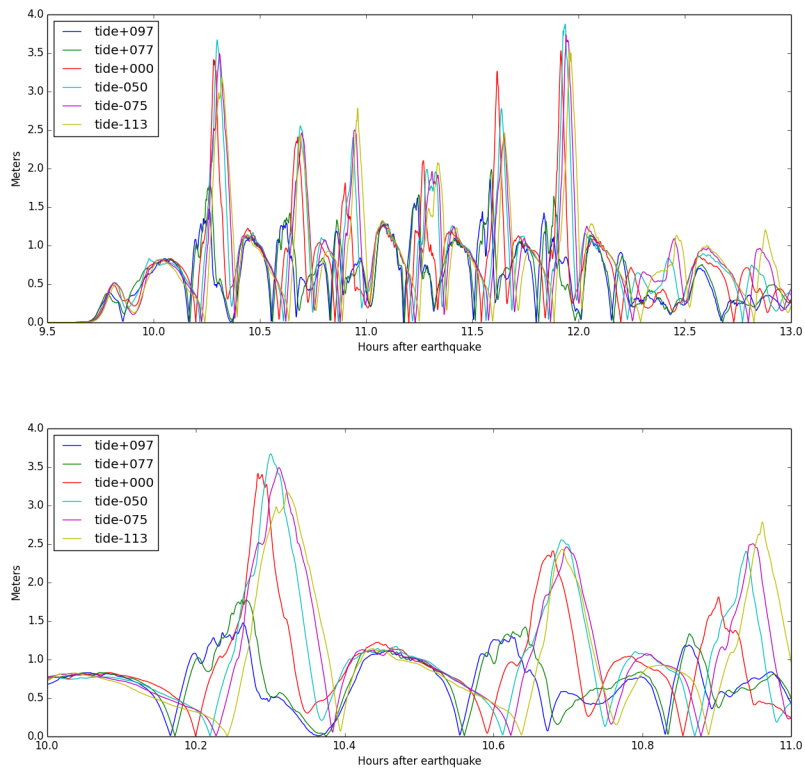
Figure 17: Current speed at synthetic gauge 102 in the Small Boat Basin, as calculated in GeoClaw runs at 6 different tide stages. The bottom figure zooms in on the first hour to better show that higher tide stage can lead to lower speeds.

Figure 18: Photograph of the Crescent City Marina taken during the Tohoku 2011 event, from Figure 3 of [4]. Numbers indicate estimated velocities in m/s. Note that the viewpoint is looking southwest.
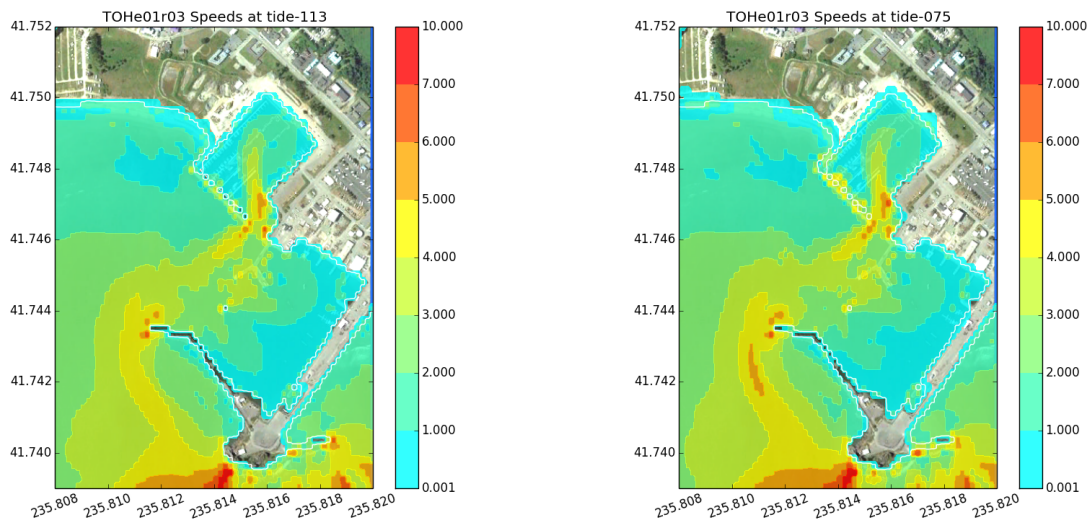
Figure 19: Computed maximum speed from simulations of the Tohoku 2011 event at fixed tide stages −1.13 m and −0.75 m relative to MSL, corresponding to MLLW and MLW respectively. Since the tsunami arrived at low tide, these are most relevant for comparison to Figure 18, although these show the maximum speeds observed while Figure 18 shows one instant in time.
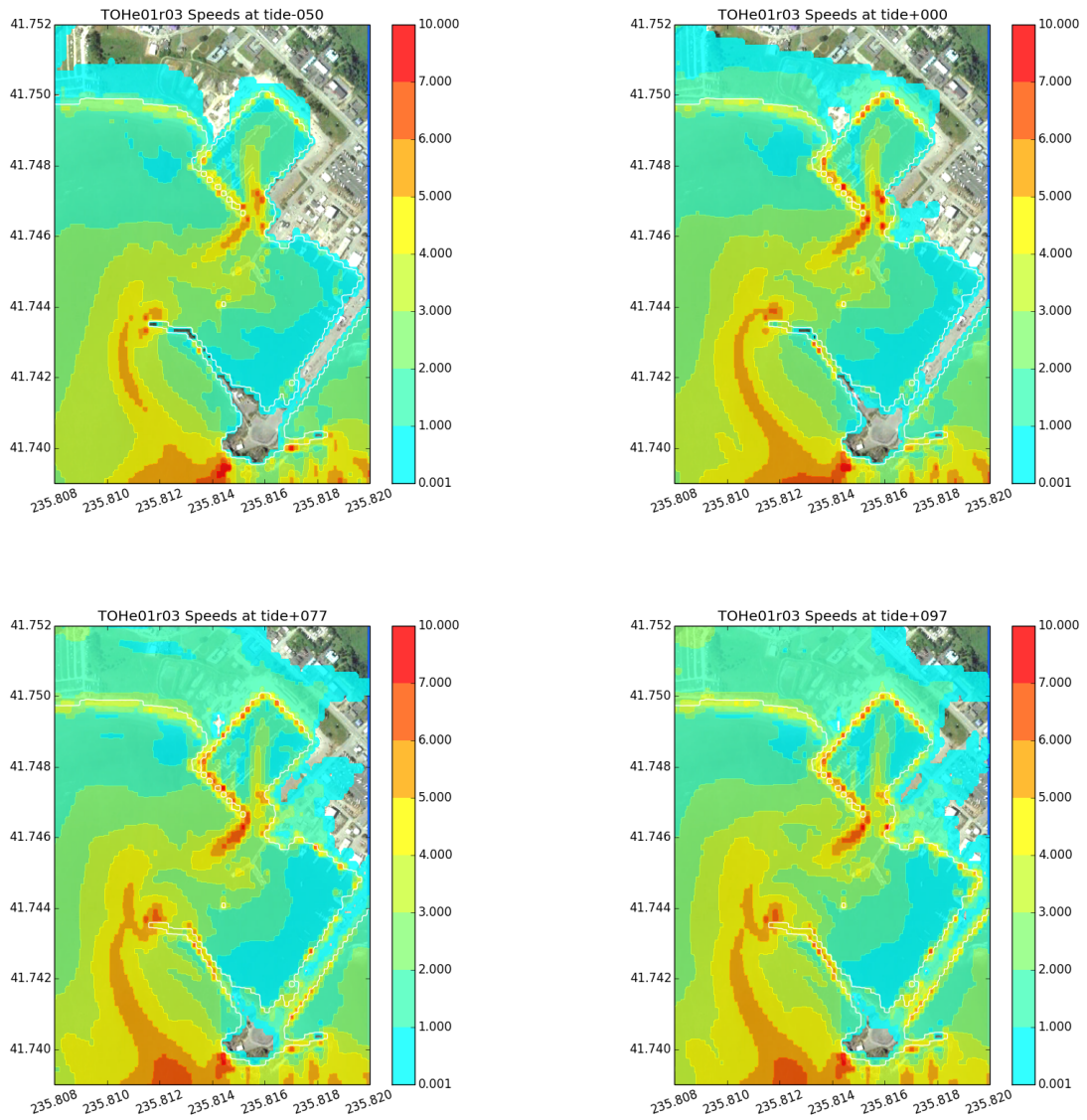
Figure 20: Computed maximum speed from simulations of the Tohoku 2011 event at fixed tide stages $-0.5, 0.0, 0.77,$ and 0.97 m relative to MSL. Note that onshore inundation is predicted at these higher tide levels.

34

7 Earthquake sources used for this study

Far-field sources used in this study, with the exception of sources off Japan, are those listed in Table 1 of the Seaside, OR, PTHA study (Tsunami Pilot Study Working Group (TPSWG), González, et al., [26]). The 2011 Tohoku event devastated the Japanese coast and inflicted serious damage on the coast of California, with more than $50-million in damage to two dozen harbors and one fatality (Wilson [57]). Consequently, a far-field source off Japan was also developed for this study as described below.

Near-field source specification in the Cascadia Subduction Zone was more difficult. Details of the incident wave characteristics, which are determined by the spatial structure of the seismic crustal displacement, have a strong effect on the degree of coastal inundation; this means a stochastic approach must be employed in which multiple realizations of the seismic slip distribution are generated, subject to geophysical constraints. It is the specification of these geophysical constraints on the slip distribution that is problematic, and this is discussed in more detail, below. After much discussion with experts, for Phase I, we decided to use the 15 realizations of CSZ events developed for a recent study of Bandon, OR [61]. These are discussed further in Section 7.6.1. For the final results, we supplement these 15 realizations with 2 additional ones as described further in this section. In addition, all 17 were adjusted as described in Section 7.6.4.

Detailed descriptions and justifications of our far-field sources also used in the Seaside study are provided in the TPSWG (2006) report [26]. In general, to take advantage of previous work in determining likely source parameters, these source specifications follow similar efforts used in the National Seismic Hazard Mapping Program. Note that, as in the Seaside study, only the largest earthquakes that might occur are considered because, although the recurrence rates are low, inclusion of more frequent but smaller earthquakes (and the associated tsunamis) is not likely to affect the 100- and 500-year hazard curves of interest. Table 1 lists the source parameters for our sources. Note that the Fault Model Specification column identifies the individual fault planes of the PMEL Unit Source Database as referenced in Arcas and Uslu [6]. Most of the text in the next four sections that explain the entries in Table 1 is taken verbatim from TPSWG [26].

All of the AASZ, KmSZ, KrSZ, SChSZ sources discussed below have been modified since the Phase I report. We are endebted to SeanPaul LaSelle for pointing out that in the PMEL fault plane descriptions, the latitude and longitude given for each unit source refer to the center of the fault plane at the bottom (deepest) edge rather than the top edge, in spite of the fact that the depth associated with each unit source corresponds to the top edge. For subduction zone faults, this change means that each fault plane is shifted seaward relative to the Phase I computations. This made a significant change in the resulting tsunami in a few cases where less of the seafloor displacement occurs onshore than previously.

7.1 Alaska Aleutians Subduction Zone (AASZ)

The seismic hazard maps for Alaska are described by Wesson et al. (1999), who consider two hazard models (Models I and II) for the Alaska-Aleutian megathrust in which earthquakes as large as M = 9.2 can occur. Model I consists of a western and an eastern seismic zone. The delineation between the zones occurs approximately at the site of the 1946 Aleutian earthquake. Model II consists of a western Aleutian seismic zone (Zone A) as in Model I, but a smaller eastern Alaska seismic zone with a western boundary coincident with the rupture boundary for the 1964 earthquake. The first tsunami model consists of three M = 9.2 earthquakes (West, Middle and East), with adjacent rupture areas. The East M = 9.2 ruptures would correspond in location to the 1964 rupture, whereas the West and Middle rupture areas would not correspond to any historic event. The Middle event also spans what some may believe is a tectonic segment boundary at the tip of the Alaska Peninsula. It is important that the rupture areas for the three events do not overlap as this would violate an important seismic moment balance along the subduction zone. Model III (West, Middle and East) was added to accommodate the possibility that a smaller magnitude earthquake (M = 8.2) in Prince William Sound might cause larger inundation at Crescent City than other earthquakes considered in this initial set of source parameters. Figures 21 and 22 present the slip and seafloor deformation for each of these earthquake source models.

Table 1: Study Source Parameters. The slip values for AASZ06-08, KmSZe01-02, KrSZe01-03, and SChSZe01 are corrections to the values used in the Seaside study of González, et.al. [22]. The conditional probabilities (weights) used in the analysis are 1 for the events with only one realization, and are given in the Total Weight column of Table 3 for the CSZRe01r01-CSZRe01r17 realizations (15 from Figure 27 plus 2 extra CSZR).

Source Name	M	Length (km)	Width (km)	Slip (m)	T_M (yr)	Fault Model Specification
AASZe01	9.2	1000	100	17.7	1313	acsza9-18, acszb9-18 (Model 1 West)
AASZe02	9.2	1000	100	17.7	750	acsza19-28, acszb19-28 (Model 1 Mid)
AASZe03	9.2	600	100	Dist.	750	acsza31-36, acszb31-36 (Model 1 East)
AASZe04	9.2	1200	100	14.8	1133	acsza11-22, acszb11-22 (Model 2 West)
AASZe05	9.2	1200	100	14.8	750	acsza23-34, acszb23-34 (Model 2 East)
AASZe06	8.2	300	100	1.9	875	acsza28-30, acszb28-30 (Model 3 West)
AASZe07	8.2	300	100	1.9	661	acsza31-33, acszb31-33 (Model 3 Mid)
AASZe08	8.2	300	100	1.9	661	acsza34-36, acszb34-36 (Model 3 East)
KmSZe01	8.8	500	100	8.9	100	kisza1-5, kiszb1-5
KmSZe02	8.8	500	100	8.9	100	kisza6-10, kiszb6-10
KrSZe01	8.5	300	100	5.3	500	kisza11-13, kiszb11-13
KrSZe02	8.5	300	100	5.3	500	kisza14-16, kiszb14-16
KrSZe03	8.5	300	100	5.3	500	kisza17-19, kiszb17-19
SChSZe01	9.5	1100	100	45.3	300	sasza39-49, saszb39-49
TOHe01	9.0	500	200	Var.	103	Shao, et.al. [51]
CSZRe01r01-CSZRe01r15	Var.	1000	Var.	Var.	250	Witter, et.al [61]
CSZRe01r16-CSZRe01r17	Var.	1000	Var.	Var.	250	Goldfinger, et.al [20]
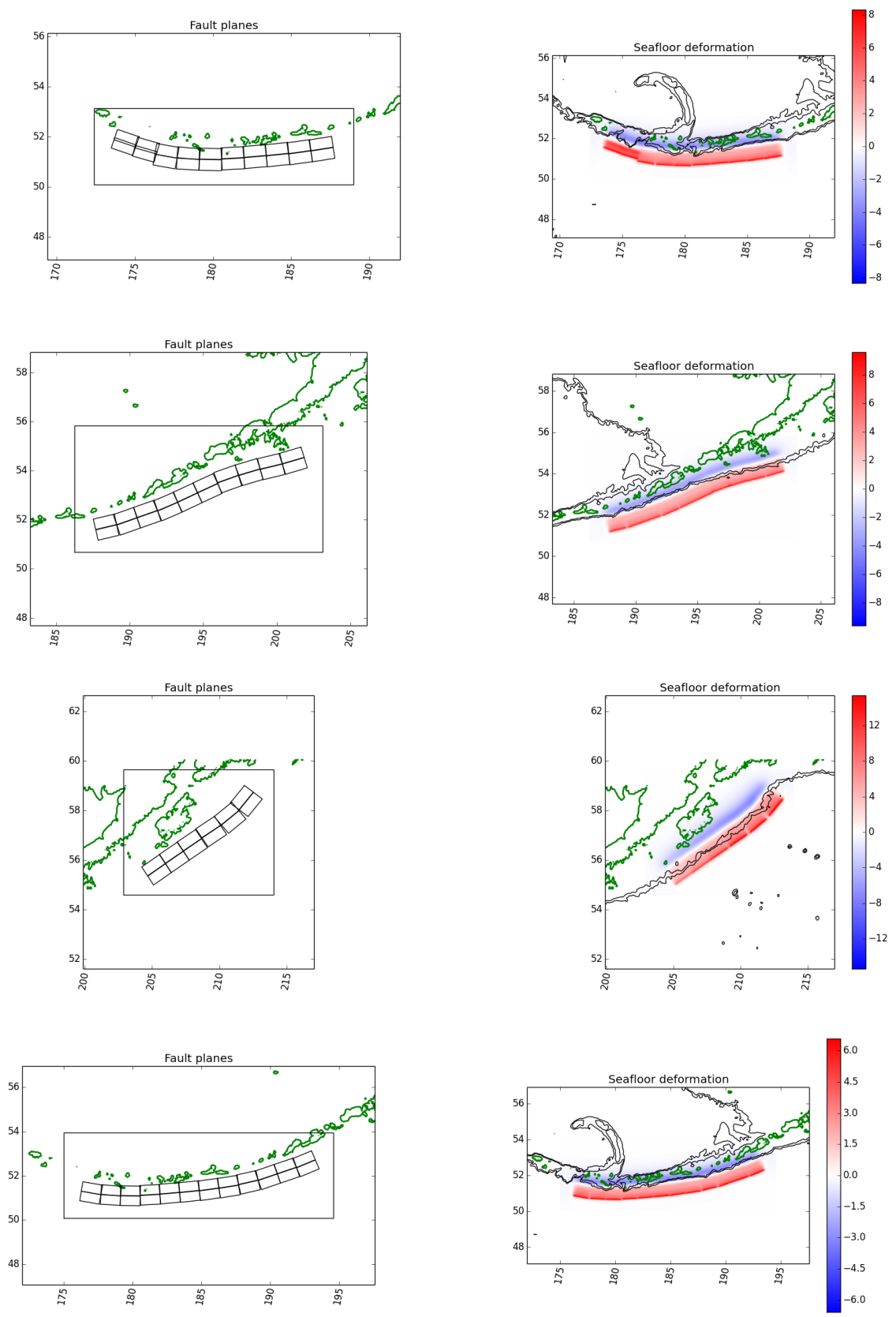
Figure 21: The sources AASZe01 through AASZe04. Left: Fault planes. Right: seafloor deformation. Note: AASZe03 is the only one in which slip varies spatially, and models the 1964 event.
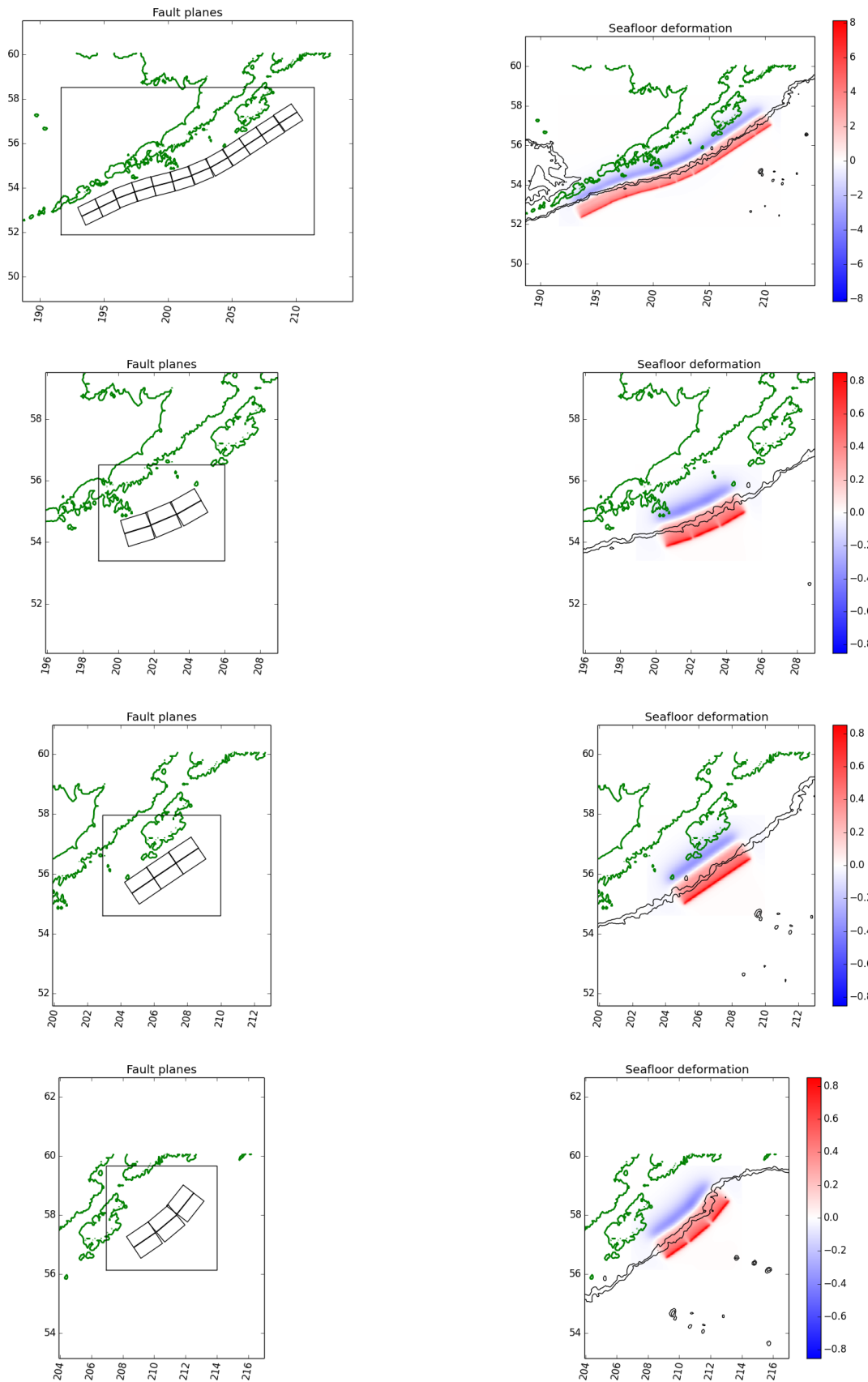
Figure 22: The sources AASZe05 through AASZe08. Left: Fault planes. Right: seafloor deformation.

7.2 Kamchatka Subduction Zone (KmSZ)

Like the Alaska-Aleutian Subduction Zone, large earthquakes have occurred along the Kamchatka Subduction Zone (KSZ) with noticeable frequency. Pinegina et. al. [44] concluded that Kamchatka has been impacted by large tsunamis at a rate of 1 every 100 years for the past 3,000 years, though not all are from local sources (about 10-20% are far field). Of note, the Mw = 8.8 1952 (Johnson and Satake, [28]) and the Mt = 8.8 1923 [1] earthquakes are probably representative of the largest earthquakes of this subduction zone. A tsunami model for Kamchatka can be constructed as done for the Alaska Tsunami Model 1 above, with two adjacent M = 8.8 earthquakes filling the entire subduction zone. Figure 23 presents the seafloor deformation for each of these earthquake source models.
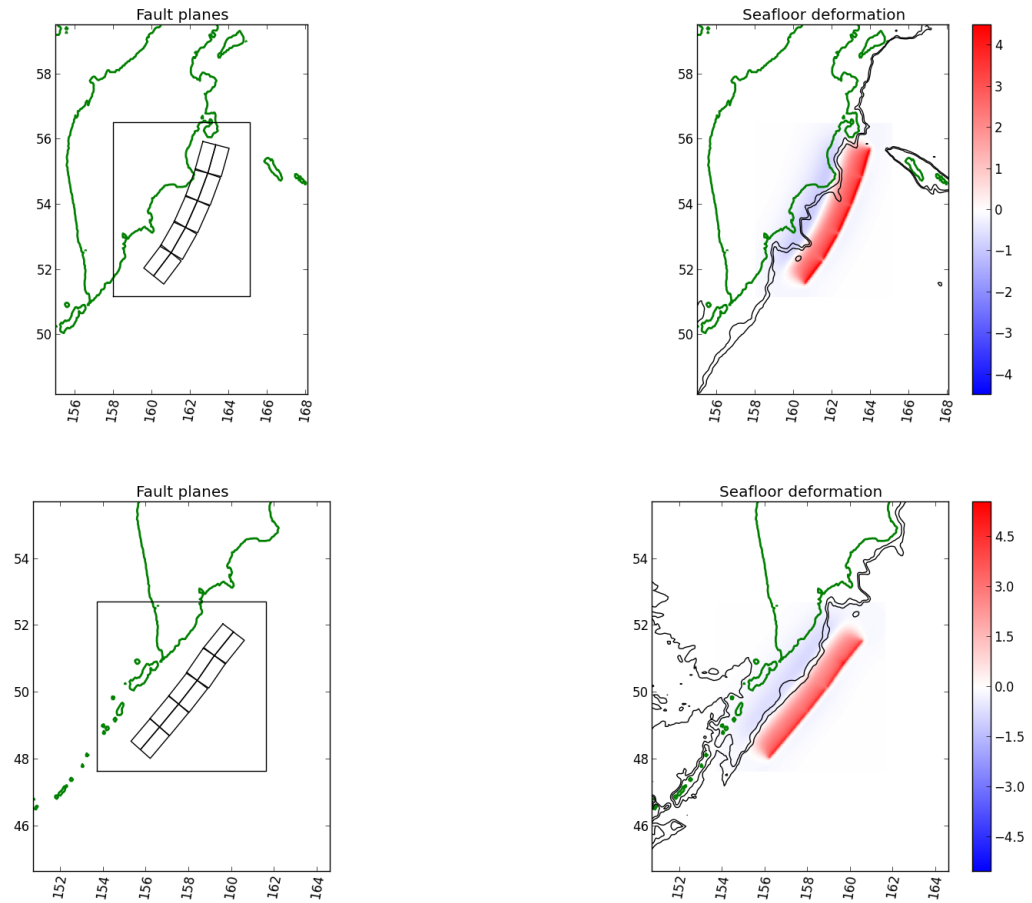
Figure 23: The sources KmSZe01 and KmSZe02. Left: Fault planes. Right: Resulting seafloor deformation.

7.3 Kurils Subduction Zone (KrSZ)

Continuing south along the Kuril Subduction Zone, the maximum magnitude earthquake is likely to be slightly smaller than for the Kamchatka Subduction Zone, primarily because of a change in tectonic regime for the overriding plate. From the analysis of the 13 October 1963 Kuril Islands earthquake (there was also a tsunami earthquake in the Kuril Islands on 20 October 1963) which Ward [56] and Ruff and Kanamori [47] placed at Mw = 8.5 and recent evidence of multi-segment rupture in the southern part of the Kuril Subduction Zone by Nanayama et. al. [41], it is reasonable to characterize this subduction zone with a series of M = 8.5 earthquakes. Nanayama et. al. [41] indicates that the average return time for these earthquakes is approximately 500 years. Approximately three M = 8.5 earthquakes would fill the Kuril Subduction Zone up to the southern extent of the Kamchatka Subduction Zone. Figure 24 presents the seafloor deformation for each of these earthquake source models.

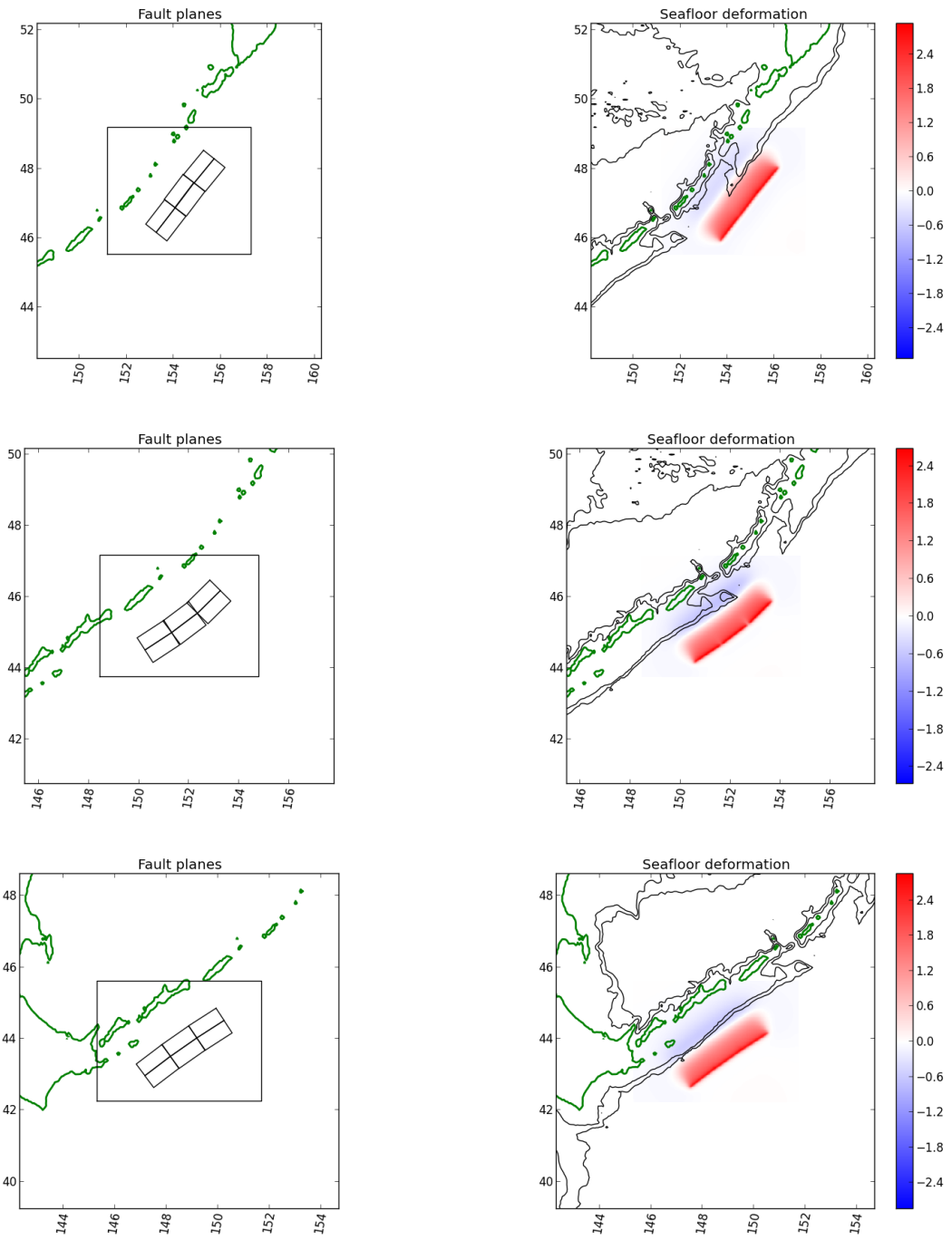Figure 24: The sources KrSZe01, KrSZe02, and KrSZe03. Left: Fault planes. Right: Resulting seafloor deformation.

7.4   South Chile Subduction Zone (SChSZ)

Earthquakes along the Chilean Subduction Zone are also considered, primarily because of the size of the M = 9.5-9.6 1960 earthquake (Cifuentes, [13]; Cifuentes and Silver, [14]) and observations of the associated tsunami along the west coast of North America. The amount of slip that occurred during the 1960 tsunami is difficult to ascertain because of the complexity of the event. The geodetic models of both Linde and Silver [33] and Barrientos and Ward [10] result in average amounts of slip that correspond to significantly lower seismic moment estimates than determined from seismic waveform data, though still at M about the 9.5 level. Average slip estimates vary from 17 m to 20 m, though the variable slip models indicate significantly higher amounts of slip, as much as 40-50 m, are predicted for the off shore extent of rupture and even small earthquakes (Barrientos and Ward, [10]; Linde and Silver, [33]). For comparison, Liu et. al. [34] use 24 m of slip in their far-field tsunami model.

Chile has been struck by giant earthquakes and tsunamis in the past, including the 1570s, 1730s, 1837, and the M about 9.5 1868 earthquake in northern Chile. These dates are not representative of return times for M about 9.5 earthquakes from purely a moment-balance perspective (Barrientos and Ward, [10]) and from recent paleoseismologic analysis by Salgado et. al. [48]. The latter study suggests an average return time for great earthquakes in Chile of about 250 years. Even so, if the average slip per event is about 20 m, this results in a seismic slip rate of 8 cm/yr or close to the relative plate convergence rate of 8.4 cm/yr. Although the southern Chile Subduction Zone is considered the most highly coupled subduction zone in the world in terms of seismic efficiency (Scholz, [49]), the repeat time should not be much smaller, nor the average slip per event be much greater, than these estimates to satisfy the moment balance. Figure 25 presents the seafloor deformation for each of these earthquake source models.
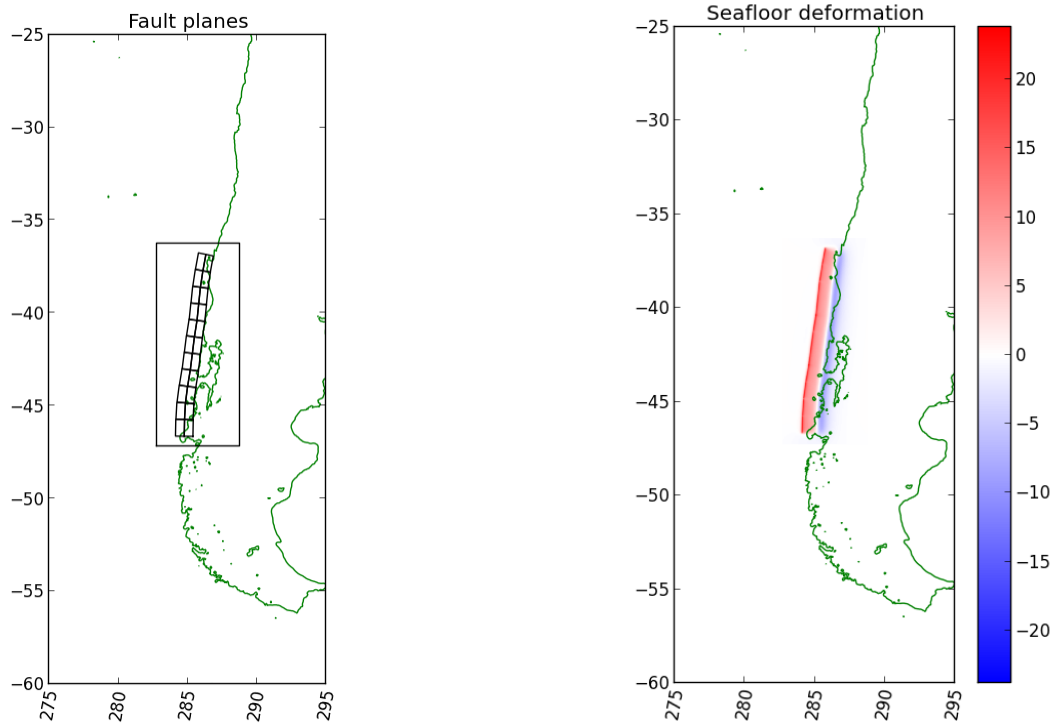

Figure 25:   The sources SChSZe01. Left: Fault planes. Right: Resulting seafloor deformation.

7.5   Japan (TOH)

The far-field sources in the Seaside study did not include potential sources offshore Japan. However, the 11 March 2011 Tohoku M9 earthquake and associated tsunami devastated the Japanese coast, leading us to include such an event in this study as a potential far-field source. Many different sources have been proposed for this event and a comparison of 10 of these sources as input to the GeoClaw model has been performed in [35]. The sources all gave consistent results with observations, both at DART buoys and at several regions on the Japan coast where inundation was compared. Any one of these sources could be used as a potential Japan source for the present study, and we have chosen to use the one proposed by G. Shao, et. al. [51], as discussed further in Section 6.2.

This is not the only possible event on the Japan trench, but we have been unable to obtain good slip realizations for other possible events. Instead we will use the Tohoku event as a proxy for an event originating anywhere in this region, and set the recurrence time to $T_M = 103$ years. This is the mean return time for a similar earthquake to occur somewhere along the Japan Trench faults, as estimated by the Japan Earthquake Research Center (JERC) in their online summary of Japanese earthquakes, see [27]. Because this fault region is so far removed from Crescent City, we believe that the inundation will be little affected by the details of location, and the Tohoku event is thought to be among the worst possible in terms of concentrated slip distribution and resulting tsunami magnitude. Even so it results in very little inundation and hence has little effect on the resulting probabilistic results.

7.6   Cascadia Subduction Zone (CSZ)

The Cascadia Subduction Zone (CSZ) extends from Northern California to Vancouver Island and is known to have produced earthquakes of magnitude 9.1 or greater in the past. Extensive paleotsunami records indicate that many events over the past several thousand years have led to extensive inundatation all along the coast and in particular in the area surrounding Crescent City. However, there have been no major events in recorded history, other than the Mw 9.1 event of 1700 for which observations are available only in Japan. From the geologic record it is difficult to estimate the range of possible events that may occur in this zone or to accurately estimate return times. This means that there is a great deal of epistemic uncertainty associated with CSZ.

Because this subduction zone is so long (≈ 1100 km) and the southern extent lies directly offshore Crescent City, the details of how slip is distributed over the fault zone have a much greater impact on the resulting inundation than is the case with farfield earthquake sources. This suggests that a large number of realizations may be necessary in order to adequately explore the aleatoric uncertainty, even if the epistemic uncertainties could be eliminated. This means that the probability distribution of possible events (even if known exactly) would lie over a relatively high dimensional stochastic space compared to farfield sources. Techniques that might be further developed to efficiently explore this space are briefly discussed in Section 10.1.

The combination of large epistemic uncertainty and high-dimensional stochastic space lead to identifying the choice of CSZ source realizations as the most questionable aspect of the current study and the most important source of uncertainty in the probabilistic results. Our approach is to use the best available science at this time as a guide for specifying realizations of the CSZ source as described below.

7.6.1   Phase I Bandon study sources

Phase I of this study [23] used 15 CSZ earthquake scenarios developed by [61] for a tsunami hazard assessment of Bandon, OR. Based on an analysis of paleoseismic data, including turbidite records, Witter, et. al. [61] generated rupture models for Cascadia Subduction Zone earthquakes to conduct a study of tsunami inundation at Bandon, Oregon. The fault parameters, including estimates of the average recurrence interval, are summarized in Table 4 of their report, which is reproduced in Figure 27. A DVD of vertical seafloor deformation data files for each of these models can be ordered online from the Nature of the Northwest (http://www.naturenw.org/). These sources are based on a logic tree formulation as illustrated in Figure 7 of [61], which is reproduced in Figure 26.

Earthquake source	Earthquake size	Interevent time (years)	Rupture geometry	Scenario name	Total scenario weight
	XXL (0.025)	1200	...		
	XL (0.025)	1050-1200	...		
	L (0.16)	650-800	...		
			Splay fault (0.6)	M1	0.32
Cascadia subduction zone (1.0)	M (0.53)	425-525	Shallow Buried Rupture (0.2)	M2	0.11
			Deep Buried Rupture (0.2)	M3	0.11
	SM (0.26)	275-300	...		
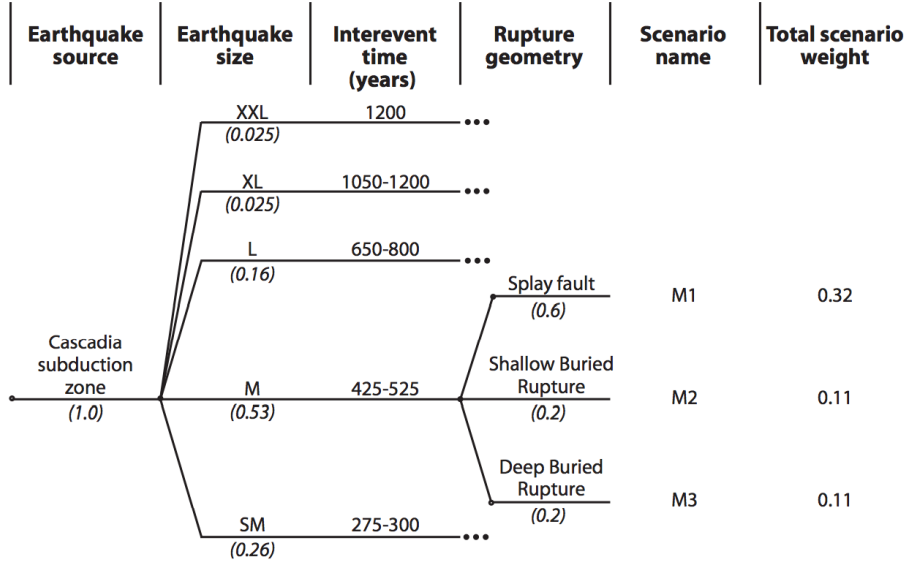
Figure 26: Figure 7 from [61], which illustrates the logic tree used in Phase I to assign conditional probabilities to different realizations of 5 possible CSZ events (in our terminology).

For Phase I, we assumed these 15 sources were realizations of a single event, and we ran two sets of probabilistic computations that differ only in the assumed mean recurrence times of 332 and 525 years, with each assigned conditional probabilities based on the expert opinion of the Bandon study authors, as expressed in the "Total Weight" column of their Table 3, reproduced in Figure 27.

For our final results, we again assumed these 15 sources were realizations of a single event, and added two more realizations for a total of 17. The conditional probabilities used were the scenario weights in the last column of the logic tree of Figure 33 instead of that of the logic tree of Figure 26. As described in Section 7.6.2, this new logic tree was constructed by assuming 40 Cascadia events had occurred in the last 10,000 years; hence, we use a return time of 250 years instead of 332 or 525.

Figure 28, Figure 29 and Figure 30 show the seafloor deformation for all 17 of the sources we used for our final results. Figure 30 includes the two new additional Cascadia sources, called CSZRe01r16 (SS1) and CSZRe01r17 (SS3). These Figures also include the adjustments of Section 7.6.4.

44

Table 3. Cascadia earthquake source parameters used to define 15 rupture scenarios. Logic tree branch weights shown in parentheses. Total scenario weight listed in right column.

Earthquake Size	Interevent Time (yrs)	Fault Geometry	Slip Range (m) Maximum	Slip Range (m) Average	M_w	Scenario Name	Total Weight
Extra Extra Large (0.025)	1,200	Splay fault (0.8)	36–44	18–22	~9.1	XXL 1	0.02
		Shallow buried rupture (0.1)	36–44	18–22	~9.2	XXL 2	0.0025
		Deep buried rupture (0.1)	36–44	18–22	~9.1	XXL 3	0.0025
Extra Large (0.025)	1,050–1,200	Splay fault (0.8)	35–44	17–22	~9.1	XL 1	0.02
		Shallow buried rupture (0.1)	35–44	17–22	~9.2	XL 2	0.0025
		Deep buried rupture (0.1)	35–44	17–22	~9.1	XL 3	0.0025
Large (0.16)	650–800	Splay fault (0.8)	22–30	11–15	~9.0	L 1	0.128
		Shallow buried rupture (0.1)	22–30	11–15	~9.1	L 2	0.016
		Deep buried rupture (0.1)	22–30	11–15	~9.0	L 3	0.016
Medium (0.53)	425–525	Splay fault (0.6)	14–19	7–9	~8.9	M 1	0.318*
		Shallow buried rupture (0.2)	14–19	7–9	~9.0	M 2	0.106
		Deep buried rupture (0.2)	14–19	7–9	~8.9	M 3	0.106
Small (0.26)	275–300	Splay fault (0.4)	9–11	4–5	~8.7	SM 1	0.104
		Shallow buried rupture (0.3)	9–11	4–5	~8.8	SM 2	0.078
		Deep buried rupture (0.3)	9–11	4–5	~8.7	SM 3	0.078

*Scenario M1 carries the highest weight and represents the "most likely" event in our analysis.

Table 4. Estimated earthquake magnitudes for Cascadia rupture scenarios

Rupture Scenario	Length (km)	Width (km)[a]	Interevent Time (yrs)	Maximum Slip (m)[b]	Average Slip (m)[c]	Seismic Moment (10^{22} N m)[d]	Moment Magnitude (M_w)[e]
XXL1	1,000	83	1,200	41	20	6.6	9.1
XXL2	1,000	105	1,200	41	20	8.4	9.2
XXL3	1,000	83	1,200	41	20	6.6	9.1
XL1	1,000	83	1,200	41	20	6.6	9.1
XL2	1,000	105	1,200	41	20	8.4	9.2
XL3	1,000	83	1,200	41	20	6.6	9.1
L1	1,000	83	800	27	13	4.4	9.0
L2	1,000	105	800	27	13	5.6	9.1
L3	1,000	83	800	27	13	4.4	9.0
M1	1,000	83	525	18	9	2.9	8.9
M2	1,000	105	525	18	9	3.7	9.0
M3	1,000	83	525	18	9	2.9	8.9
SM1	1,000	83	300	10	5	1.7	8.7
SM2	1,000	105	300	10	5	2.1	8.8
SM3	1,000	83	300	10	5	1.7	8.7

[a]Equivalent fault width; modeled fault width varies with latitude.
[b]Maximum slip estimates are the product of the recurrence interval times a convergence rate at southern Oregon latitudes (34 mm yr^{-1}).
[c]Average slip estimate is 0.49 of maximum slip estimate.
[d]Seismic moment (M_0) = fault area × slip × rigidity, where rigidity = 4×10^{10} N m^{-2}.
[e]Moment magnitude (M_w) = (log M_0 − 9.1)/1.5.

Figure 27: Tables 3 and 4 from [61], listing the different CSZ events and realizations used in the study of Bandon, Oregon. For our Phase 1 study, we viewed this as one CSZ event with 15 different realizations with conditional probabilites given in the Total Weight column of Table 3.

Figure 28: Seafloor deformation for the Bandon study sources [61]. Three realizations are given for each size XXL (top) and XL (bottom).
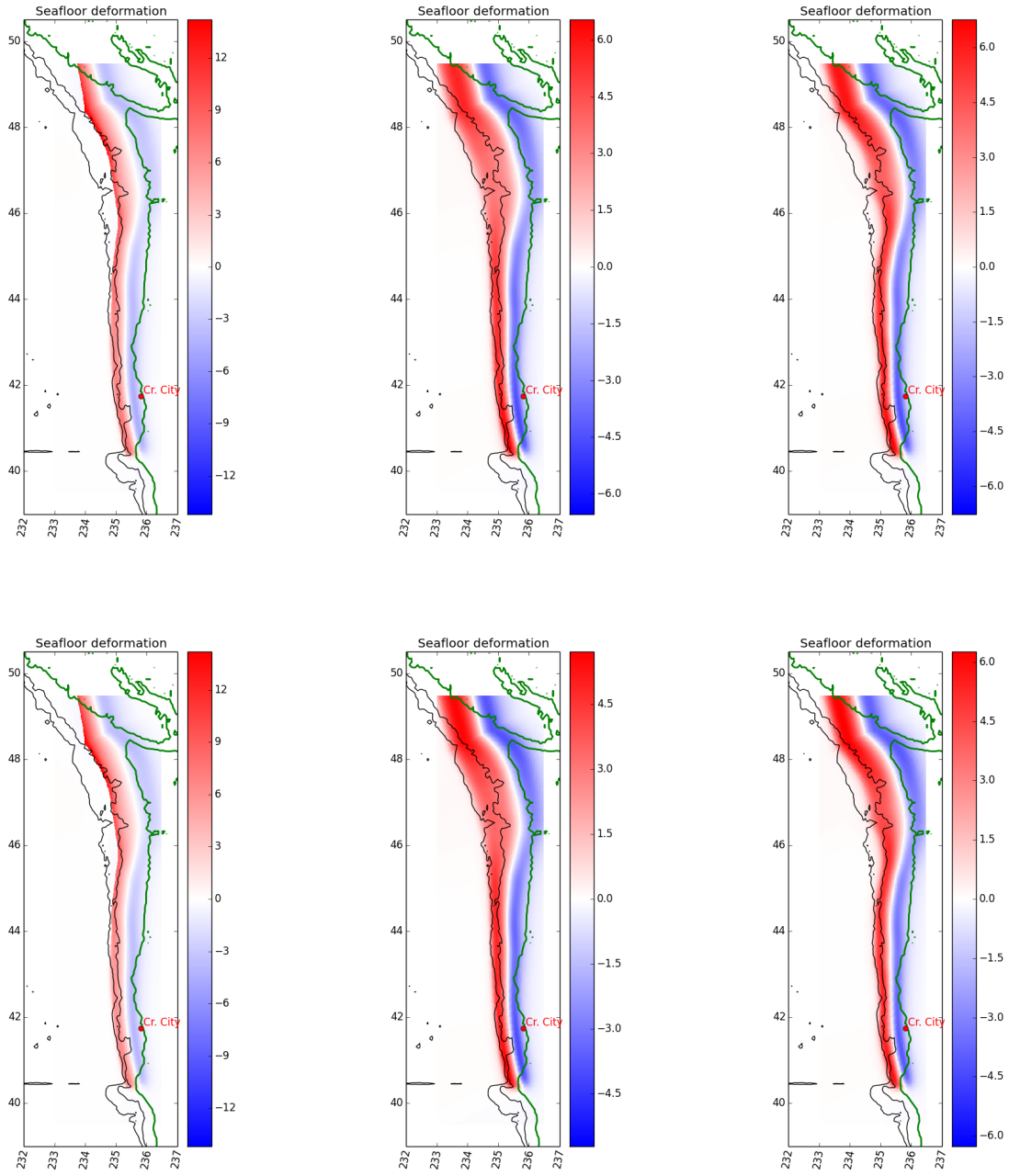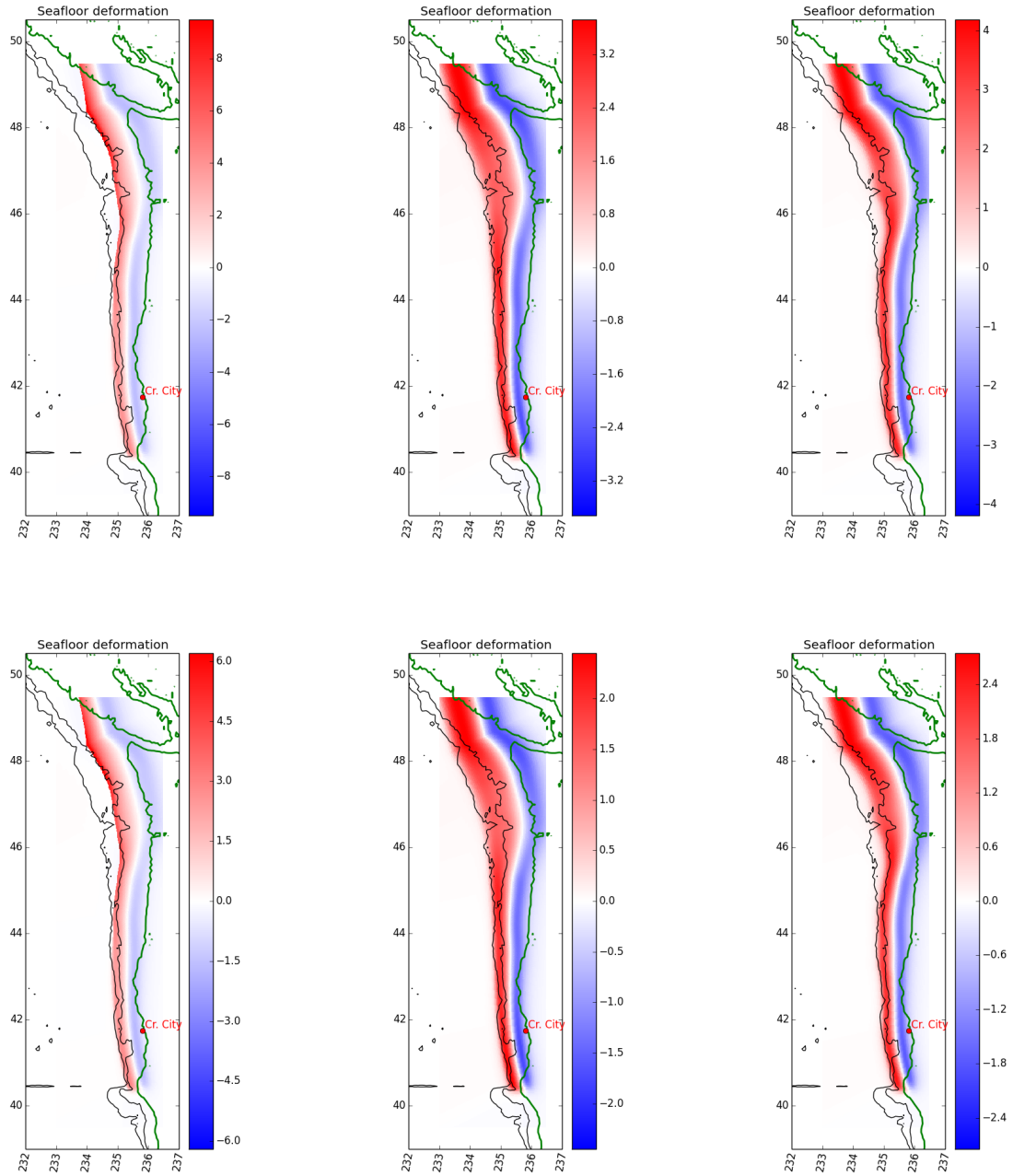
Figure 29: Seafloor deformation for the Bandon study sources [61]. Three realizations are given for the size L (top) and M (bottom).
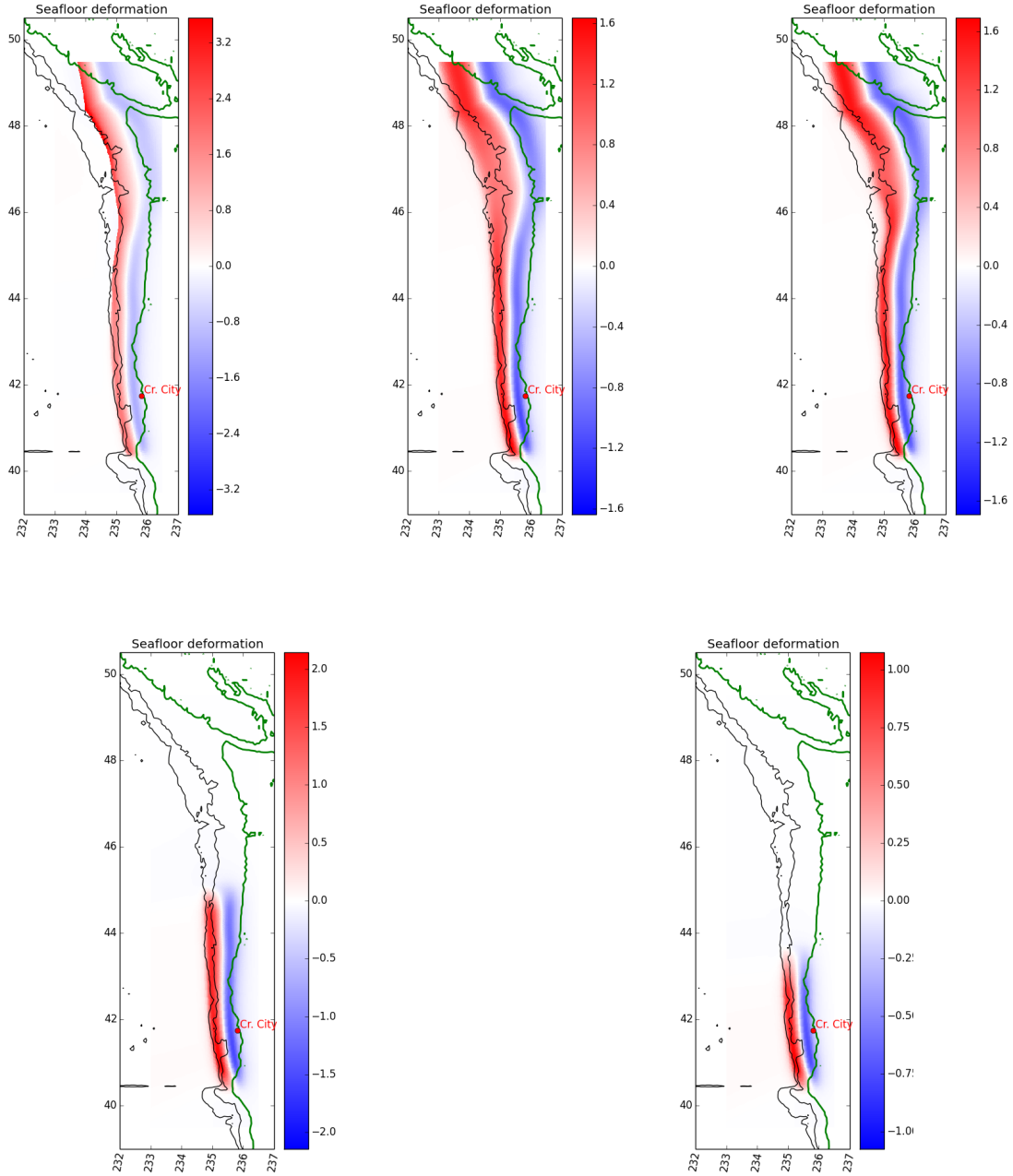
Figure 30: Three realizations of Bandon study sources of size SM (top). Seafloor deformation for the two additional Cascadia study sources SS1 and SS3 (bottom).

7.6.2 Proposed 2014 update to U.S. National Seismic Hazard Map

Recently, [46] assessed the tsunami threat posed to Washington and Oregon communities by sources C and D described in [20]. These two sources are now included in the proposed 2014 update to the U.S. National Seismic Hazard Maps currently under review ([54]); the recurrence periods assigned to each of the NSHM rupture zones 530, 2500, 910 and 1250 years for the A, B, C and D zones, respectively, yield an overall 239 years for the mean time of recurrence for any one of the 4 scenarios to occur. These rupture zones are shown in Figure 31 below.

Figure 31: Four rupture zones identified by Goldfinger, et.al in 2012 [20] and annotated by USGS [54] with the preferred magnitude and recurrence time used for each rupture scenerio; this is the initial implementation under review for possible inclusion in the 2014 U.S. National Seismic Hazard Maps

The Crescent City Probabilistic Tsunami Hazard Analysis Work Group [25] evaluated the CSZ sources adopted by the UW team and noted that 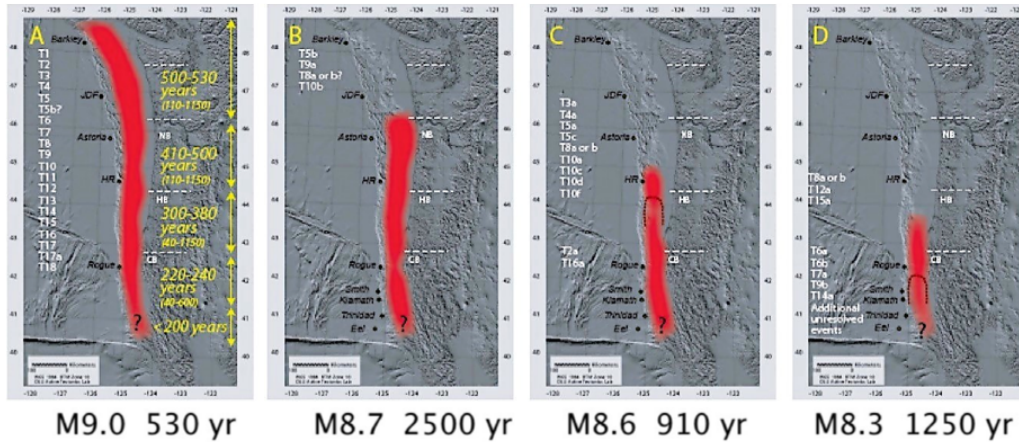"The UW model does not seem to reflect partial ruptures with smaller magnitude earthquakes, like the segmented branch of the NSHM logic tree that is based on the segmentation boundaries and event rates of Goldfinger (2012, i.e., cases B,C, and D)." They further recommended "Consideration and integration into the PTHA of additional smaller earthquakes (M8.0 to M8.5) that occur more often in the southern CSZ" and, finally, concluded that "Alignment of the PTHA with the formal NSHM Probabilistic Seismic Hazard Analysis is important, especially for production of consistent products statewide and nationally (building code, policymakers, and NTHMP), but some adjustments may be needed to accomodate unique aspects of tsunami generation and simulation."

7.6.3   Logic tree

In light of this guidance, we constructed a logic tree based on the analyses of 40 turbidite records spanning 10,000 years, implying a mean CSZ recurrence time of 250 years; in the analyses, a total of 19, 4, 8, and 9 turbidite events were assigned to each of the four rupture zones A, B, C and D, implying mean recurrence times of 526, 2500, 1250, and 1111 years in each zone, respectively, see Figure 32.

Since a seismic deformation model for segment B does not yet exist, our logic tree consists of three branches, arrived at in the following manner. We first note that unpublished evidence based on preliminary analysis of new cores on the Washington slope suggests that B events are closer to segment A types than previously reported (C. Goldfinger, personal communication). Also, those turbidite mass values that are currently available suggest the assignment of 2 of the four B events to size M and 2 to size SM, which leads to the logic tree presented in Figure 33. We interpret the assigned scenario weights (last column of Figure 33) as conditional probabilities for the occurrence of each individual scenario.

The following information used to construct this logic true should also be noted: (1) the seven rupture scenerios (XXL, XL, L, M, SM, SS1, SS3) reflect relative earthquake sizes inferred from paleoseismic turbidite data ([20] in unpublished data from the Gorda Plate), assuming that XXL slip does not decrease significantly from north to south during extreme events; (2) recurrence intervals for the full margin scenarios M, L, and XL that decrease toward the south based on the observation of shorter recurrence times and segment ruptures offshore southern Oregon and northern California, (3) the 20,000-yr recurrence values for the XXL and XL branches result from representing a 1/10,000-yr event in 2 different ways, with and without taper of slip to the south.

Table 34 summarizes the seismic parameters for each scenario. The last column provides the individual scenario recurrence times, approximated by $p = 1 - e^{1/T} \approx 1/T$ for T much greater than 1 year. Note that, although some of the scenario recurrence times are many times longer than the 10,000-yr record, these values are not to be interpreted as physically meaningful; they are simply a mathematical construct of the logic truee process that is consistent with the 250 year mean CSZ recurrence time.

Table 8. Magnitude estimated from time interval, plate motion, and rupture-zone dimensions, Cascadia subduction zone.

Turbidite number	Mean age	Northern margin following interval, in years	Northern margin slip from following time, in meters	Southern margin interval, in years	Southern margin slip from time, in meters	Average northern and southern slip, in meters	Segment name	Rupture length, in kilometers	Rupture width, in kilometers	Mw	Seismic moment
1	250					16.0	A	1,000	83	9.00	398.4E+27
2	482	232	8.9	232	8.3	8.4	A	1,000	55	8.70	138.3E+27
2a	550			57	2.1	2.1	D	222	40	8.19	23.8E+27
3	798	305	11.2	248	8.9	10.0	A	1,000	83	8.87	250.2E+27
3a	1,077			279	10.0	10.0	C	444	50	8.34	40.1E+27
4	1,243	446	16.3	167	6.0	11.2	A	1,000	83	8.90	277.9E+27
4a	1,429			186	6.7	6.7	C	444	50	8.25	29.9E+27
5	1,554	311	11.4	125	4.5	7.9	A	1,000	83	8.80	197.4E+27
5a	1,820			266	9.6	9.6	C	444	50	8.41	51.9E+27
5b	2,036			216	7.8	7.8	B	660	60	8.66	122.5E+27
5c	2,323			286	10.3	10.3	C	444	50	8.41	51.1E+27
6	2,536	982	35.9	213	7.7	21.8	A	1,000	83	9.09	542.7E+27
6a	2,730			194	7.0	7.0	D	222	40	8.24	28.7E+27
7	3,028	492	18.0	298	10.7	14.4	A	1,000	83	8.97	358.2E+27
7a	3,157			129	4.6	4.6	D	222	40	8.23	27.5E+27
8	3,443	415	15.2	286	10.3	12.7	A	1,000	83	8.94	317.2E+27
8a	3,599			442	5.6	0.0	B	660	60	8.67	124.4E+27
8b	3,890			447	10.5	10.5	D	222	40	8.15	21.0E+27
9	4,108	665	24.4	218	7.9	16.1	A	1,000	83	9.01	401.1E+27
9a	4,438			548	11.9	0.0	B	660	60	8.35	41.4E+27
9b	4,535			426	3.5	3.5	D	222	40	8.17	22.5E+27
10	4,770	661	24.2	235	8.5	16.3	A	1,000	83	9.01	406.6E+27
10a	5,062			292	10.5	10.5	C	444	50	8.39	47.6E+27
10b	5,260			198	7.1	7.1	B	660	60	8.43	55.7E+27
10c	5,390			130	4.7	4.7	C	444	50	8.55	82.7E+27
10d	5,735			344	12.4	12.4	C	444	50	7.90	9.0E+27
10f	5,772			37	1.3	1.3	C	444	50	8.37	44.8E+27
11	5,959	1189	43.5	187	6.7	25.1	A	1,000	83	9.13	625.5E+27
12	6,466	508	18.6	508	18.3	18.4	A	1,000	55	8.93	304.0E+27
12a	6,903			437	15.7	15.7	D	222	40	8.22	26.7E+27
13	7,182	715	26.2	278	10.0	18.1	A	1,000	83	9.04	450.7E+27
14*	7,625	443	16.2	443	16.0	16.1	A	1,000	83	9.01	400.7E+27
14a	7,943			318	11.4	11.4	D	222	40	8.17	22.1E+27
15	8,173	548	20.1	230	8.3	14.2	A	1,000	83	8.97	353.0E+27
15a	8,459			286	10.3	10.3	D	222	40	8.36	42.9E+27
16	8,906	733	26.8	447	16.1	21.4	A	1,000	83	9.09	534.1E+27
16a	9,074			169	6.1	6.1	D	222	40	7.54	2.6E+27
17	9,101	195	7.2	27	1.0	4.1	A	1,000	55	8.49	67.0E+27
17a	9,218	117	4.3	117	4.2	4.2	A	1,000	55	8.50	70.1E+27
18	9,795	577	21.1	577	20.8	20.9	A	1,000	83	9.08	521.2E+27

Figure 32: Table 8 from Goldfinger, et.al. (2012) [20], an analysis of 40 turbidites in the CSZ spanning 10,000 years.

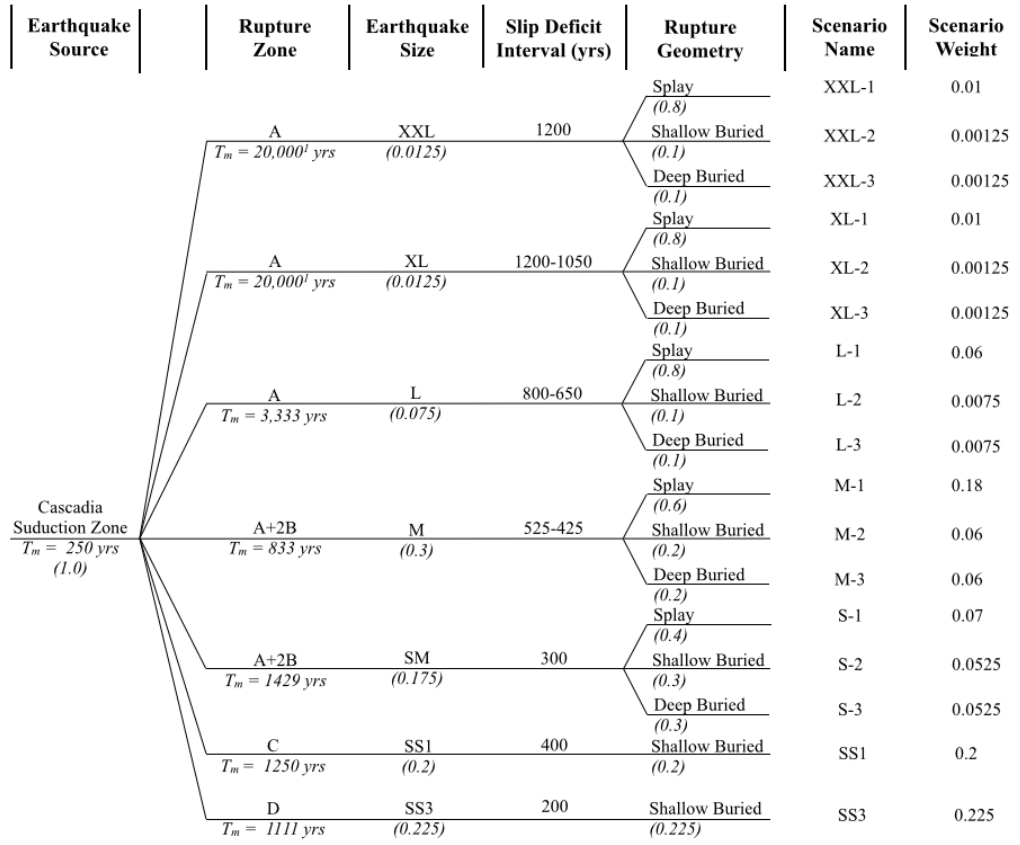| Earthquake Source	Rupture Zone	Earthquake Size	Slip Deficit Interval (yrs)	Rupture Geometry	Scenario Name	Scenario Weight
	A $T_m = 20,000^1$ yrs	XXL (0.0125)	1200	Splay (0.8)	XXL-1	0.01
				Shallow Buried (0.1)	XXL-2	0.00125
				Deep Buried (0.1)	XXL-3	0.00125
	A $T_m = 20,000^1$ yrs	XL (0.0125)	1200-1050	Splay (0.8)	XL-1	0.01
				Shallow Buried (0.1)	XL-2	0.00125
				Deep Buried (0.1)	XL-3	0.00125
	A $T_m = 3,333$ yrs	L (0.075)	800-650	Splay (0.8)	L-1	0.06
				Shallow Buried (0.1)	L-2	0.0075
Cascadia Suduction Zone $T_m = 250$ yrs (1.0)				Deep Buried (0.1)	L-3	0.0075
	A+2B $T_m = 833$ yrs	M (0.3)	525-425	Splay (0.6)	M-1	0.18
				Shallow Buried (0.2)	M-2	0.06
				Deep Buried (0.2)	M-3	0.06
	A+2B $T_m = 1429$ yrs	SM (0.175)	300	Splay (0.4)	S-1	0.07
				Shallow Buried (0.3)	S-2	0.0525
				Deep Buried (0.3)	S-3	0.0525
	C $T_m = 1250$ yrs	SS1 (0.2)	400	Shallow Buried (0.2)	SS1	0.2
	D $T_m = 1111$ yrs	SS3 (0.225)	200	Shallow Buried (0.225)	SS3	0.225

Figure 33: The CSZ logic tree constructed for this study. The last column is the weight assigned to each individual scenerio.

Recurrence (yrs)	Rupture Zone	Rupture Wt	Slip Deficit Interval (yrs)	Rupture Geometry	Rupture Geometry Wt	Scenario Name	Mw	Length (km)	Width (km)	Scenario Wt	Ts (yrs)
20000	A	0.0125	1200	Splay	0.800	XXL-1	9.1	1,000	83	0.01000	25,000
		0.0125		Shallow	0.100	XXL-2	9.2	1,000	105	0.00125	200,000
		0.0125		Deep	0.100	XXL-3	9.1	1,000	83	0.00125	200,000
20000	A	0.0125	1200-1050	Splay	0.800	XL-1	9.1	1,000	83	0.01000	25,000
		0.0125		Shallow	0.100	XL-2	9.2	1,000	105	0.00125	200,000
		0.0125		Deep	0.100	XL-3	9.1	1,000	83	0.00125	200,000
3333	A	0.0750	800-650	Splay	0.800	L-1	9.0	1,000	83	0.06000	4,167
		0.0750		Shallow	0.100	L-2	9.1	1,000	105	0.00750	33,333
		0.0750		Deep	0.100	L-3	9.0	1,000	83	0.00750	33,333
833	A+2B	0.3000	525-425	Splay	0.600	M-1	8.9	1,000	83	0.18000	1,389
		0.3000		Shallow	0.200	M-2	9.0	1,000	105	0.06000	4,167
		0.3000		Deep	0.200	M-3	8.9	1,000	83	0.06000	4,167
1429	A+2B	0.1750	300	Splay	0.400	SM-1	8.7	1,000	83	0.07000	3,571
		0.1750		Shallow	0.300	SM-2	8.8	1,000	105	0.05250	4,762
		0.1750		Deep	0.300	SM-3	8.7	1,000	83	0.05250	4,762
1250	C	0.2000	400	Shallow	1.000	SS1	8.6	450	66	0.20000	1,250
1111	D	0.2250	200	Shallow	1.000	SS3	8.2	250	61	0.22500	1,111

Figure 34: Seismic parameters for the 17 scenarios presented in the Logic Tree of Figure 33.

7.6.4 Slip reduction near Crescent City

Before these scenarios are used to model tsunami generation and inundation at Crescent City, we must also take account of new estimates of CSZ convergence rates at the latitude of Crescent City that are lower than the overall value of 34 mm/yr that was assumed in developing all CSZ vertical deformation models in our earlier work [23]. The significance of a lower convergence rate is a lower slip value when rupture occurs which, in turn, produces lower vertical vertical deformation and correspondingly lower initial tsunami wave height generation in the rupture zone.

A recent study [50] finds that decreasing slip in a southward taper and an increase in the frequency of events are CSZ features that are to be expected from the geometry of the locked zone [55] and calculations of energy flux [38], and conclude that the interpretation of turbidite data by [20] is consistent with this expectation. In addition, computation of a balanced table of slips for the four segments suggests that, in addition to the southward taper, each segment slips less as the total length gets shorted [50]; consequently, if only one of the B, C, or D segments ruptures in isolation (as we assume in this study), then the slip in each case is less than if the segment were to slip as part of a full margin rupture. This is a level of complexity beyond the scope of the present study, in which we use only the existing CSZ slip models at our disposal. We can, however, partially account for these new findings in the following manner.

McCaffrey et. al. (2013) [38] provides estimates of CSZ convergence rates that include the along-trench and forearc deformation components. Noting that almost all worldwide observations indicate that only the trench normal component is recovered in a plate boundary earthquake, we remove the trench parallel component and forearc deformation from the estimate of CSZ convergence of the Gorda Plate at the latitude of Crescdnt City in rupture zone D [38] and find that the normal component in that area is about 21 mm/yr. Accordingly, for all the CSZ source models used in this study, we reduce the vertical deformation values by the factor $21/34 \approx 0.62$ to improve the consisency of our computations with the new information now available, i.e., that a significant reduction in slip is to be expected southward and, in particular, near Crescent City.

7.6.5 Geographical limit of applicability

Note that this procedure results in underestimation of vertical deformation in central and northern Cascadia, but this likely introduces a small error in our tsunami inundation estimates, given the modest influence of distal source areas on tsunami heights near Crescent City [46]. On the other hand, there is a definite geographical limitation to the validity of this approach; becuase of this modification to the vertical deformation fields, the logic tree corresponding to Figure 34 is only applicable to the geographic area of rupture zone D. The sources developed by [61] would be more accurate for coastal sites farther north.

We emphasize that the focus of this study is methodology development for PTHA, not the production of state-of-the-art PTHA products for operational use. Nonetheless, within the limitations of time, resources, and most importantly, less than optimal CSZ source models, we have sought to make the products presented here as consistent as possible with best available science. We are planning a future publication of PTHA analyses that use an update of the CSZ deformation models [55] that are consistent with the recent progress in understanding CSZ slip distribution, as discussed above.

7.7 Comparison of Model Results to Paleotsunami Records

Paleotsunami studies offer potential ground truth for modeling efforts such as this project, though with caveats relating to the disparity between modeled runup distance and the capacity of a tsunami to carry enough material to leave a geologic record. This report does not attempt to fully explore this issue, which will be pursued in a subsequent publication. Here we make a preliminary assessment of the correspondence (or lack thereof) between existing paleotsunami records and the model results. Though lacking an in-depth treatment of the inherent variability in geologic systems of paleo vs. model results, a first order comparison is warranted.

7.7.1 Inundation Extent in the Paleotsunami Record

Paleo tsunami records are available in the Lagoon Creek area, 18 km south of Crescent City (Abramson [2]; Garrison-Laney [16]). These records are consistent with other records of significant Cascadia tsunamigenic earthquakes along the coast (Atwater et al. [9], Kelsey et al. [29]) as well as turbidite records offshore (Goldfinger et al. [20]; Goldfinger et al. [19]; Enkin et al. [15]). The Lagoon Creek records include six events which are coeval with the offshore records of turbidites T1, T3, T4, T5, T6, and T7 within the limitations of radiocarbon comparisons (Goldfinger et al. [20]). Similar records are also found at Bradley Lake (Kelsey et al. [29]) and other land sites, although most land sites have preservation limitations that are discussed in the original publications and in Goldfinger et al. [20]. The most consistent comparison is found in Goldfinger et al. [20] with respect to the regionally correlated turbidites mentioned above. Missing from the tsunami record and many land sites is the offshore T2 event, a likely small event that is typically not recorded at land sites. A key link between the onshore and offshore records is the ≈ 1000 year time gap between offshore events T4 and T5, which is replicated at all land sites with long enough records, including Lagoon Creek. This diagnostic gap in the records at multiple sites provides a robust onshore-offshore link that confirms the recording of multiple lines of evidence from the same phenomenon. The Lagoon creek records include all six events at sites within ≈ 600 m of the modern coast, and diminishing numbers of events landward. At 1 km from the coast, four events remain, likely equivalent to offshore T1, T4, T5, and T6. At 1.5 km from the coast, only three events remain.

Peterson et al. [43] collected cores closer to Crescent City, and provide a second source of evidence closely applicable to this study as shown in Figure 35.
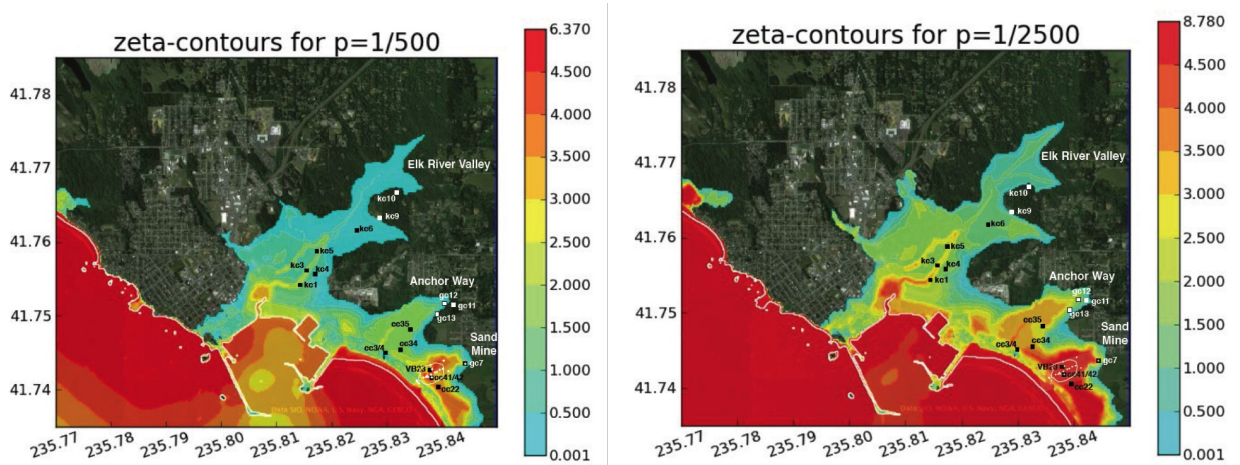

Figure 35: Inundation depths and limits for the 500 (left) and 2500 (right) scenerio events. Core sites and drainage areas from Peterson, et al. [43] are shown.

Peterson et al. [43] examined three back barrier marshes near Crescent city for evidence of tsunami inundation of the local marshes. Cores in the lower Sand Mine marsh and Lagoon record 6-7 tsunami events (excluding 1964) in ≈ 3000 years, with broad temporal agreement with both Lagoon Creek and the offshore turbidite record. As at Lagoon Creek, the number of probable tsunami sand sheets diminishes landward to three sand sheets at an elevation of 7-8m at core GC-7, ≈ 0.85 km from the coast. At Elk Creek, additional cores constrain runup in the main drainage adjacent to Crescent City. These cores extend upstream in the Elk Creek drainage ≈ 2.4 km from the point at which Elk Creek enters the Crescent City Harbor. The series of 7 cores in the Elk Creek drainage all contain probable tsunami sand sheets (Peterson et al. [43]). The Elk Creek drainage includes 7 cores that constitute the best available comparison with tsunami runup models; their landward extent is the greatest of the three drainages in the Peterson et al. [43] study. The Elk Creek cores have a shorter record, and include 3-4 tsunami sand sheets, including the 1964 tsunami sand layer in the upper part of the three most seaward cores. As with the other sites near Crescent City, the

number of tsunami sand sheets is maximized near the present coast, diminishing to the landward extent of the dataset. At Elk Creek, the landward most core is KC-10, which contains only one probable tsunami sand sheet at a depth of ≈ 95 cm in the core. The sand bed is dated at 790-960 cal. BP ($2\ \sigma$), consistent with the second sand sheet at other nearby land paleoseismic sites, and consistent with offshore regional turbidite T3 (660-940 cal. BP) in core TN0909-07PC near Trinidad Canyon (Goldfinger et al. [19]).

The Elk Creek cores evidently do not extend far enough landward to encompass the landward limits of tsunami sand sheets or of inundation, which is greater. The presence of a single sand sheet in core KC10 suggests it may be near the limit for "typical" events, as all but one in the past several thousand years were not recorded at that site.

7.7.2 Comparison of Modeled Runup with Paleotsunami Data

The modeled runup data for a variety of tsunami sources is shown in Figure 35. To make a comparison with locally sourced paleotsunami data, we briefly compare the Elk Creek record with the models shown in Figure 35. The most comparable model is probably the "500 Year" model. The average recurrence time for tsunami sand sheets in the past 3000 years considering all the available land data is ≈ 450 years ([43]). Offshore the turbidite data include at least one additional smaller event, T2, as well as numerous smaller events correlated along the southern margin (Goldfinger et al. [20]; Goldfinger et. al. [19]). While some of these events are likely recorded at Bradley Lake (Kelsey et al. [29]; Goldfinger et al. [18]; Goldfinger et al. [20]; Goldfinger et al. [19]; Witter et al. [60]), none of them have left tsunami sand sheets in the Crescent City area, suggesting that if they extend that far south as discrete ruptures, then the evidence they left (if any) was likely less than that of the 1964 event, which is prominent at Crescent City ([43]). For this reason, we roughly equate the 500 year model to the paleotsunami record of [43] and Garrison-Laney [16]. In general, the model and paleotsunami records appear broadly compatible, with model inundation extending somewhat beyond the KC10 site up the Elk Creek drainage, something that would be expected from a comparison of modeled or real inundation vs. geologic preservation. The other sites also appear broadly compatible, though they are somewhat less diagnostic.

7.7.3 Discussion

While the paleotsunami result and model results appear broadly compatible, there are limitations to both datasets that make direct comparison imperfect. First, it appears that the three sand sheets die out upstream in Elk Creek drainage, as would be expected, with only one remaining at the furthest limit of the core dataset (KC10). While this site may approach the limit of tsunami inundation for an approximate 500 year event, it does not exceed and establish that limit (see the left graph in Figure 35). It is interesting that the locally largest turbidite in the time range addressed by the Elk Creek cores is compatible temporally with the sand sheet extending the furthest landward, represented at site KC10, suggesting a possible further linkage between the onshore and offshore data. We note that the landward limit at Elk Creek drainage may be the most sensitive measure of inland runup. At other sites, and along the lateral limits of the Elk Creek system, topographic control appears quite strong. This is apparent when comparing the lateral limits along the Elk Creek drainage for the 500 and 2500 year events as shown in Figure 35. While wave height, flooding depth and other parameters increase for these scenarios, the lateral inundation changes little for these increasingly large sources. This indicates that topography exerts enough control that land area inundated is a poor measure of tsunami energy and displaced water volume.

Figure 36 shows the DEM and contours for the Elk Creek drainage. Apparent is the flat terrace to the north at an elevation of ≈ 10 m, which is somewhat less prominent to the south. The drainage thalweg is below 5 m, with most of this elevation change occurring within ≈ 300 m of the thalweg. Figure 37 shows a shaded relief of the same area, illustrating the sharp boundaries and relatively steep gradients that confine tsunami wave energy within the drainage.

Second, the cores in Peterson et al. [43] are located near the axis of lowest topography, and are similarly not particularly sensitive to event size because they don't reach and surpass the maximum, nor do they
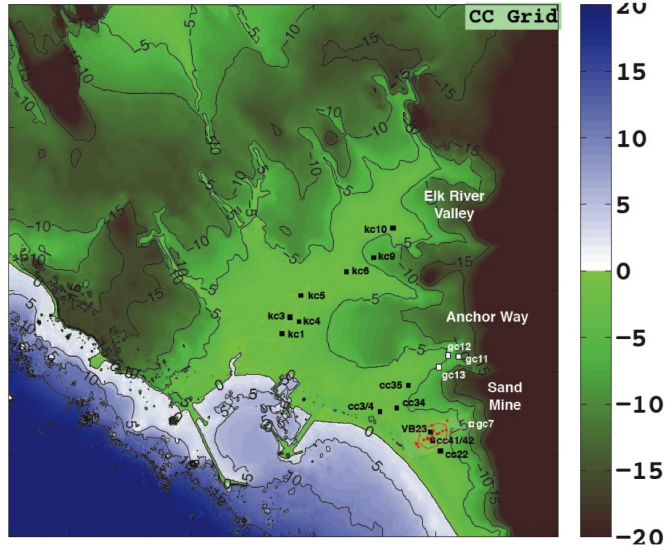
56

Figure 36: Crescent City color flooded DEM with contours and core sites of Peterson et al. [43] shown.
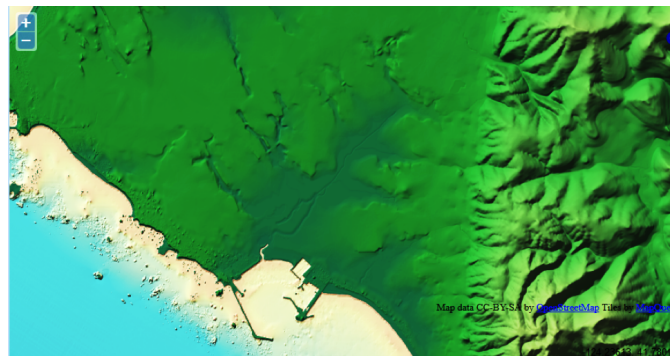

Figure 37: 1/3 arc second shaded relief DEM of Crescent City, Elk Creek drainage, and surrounding areas. Image from http://data.noaa.gov/viewer.

sample the lateral limits of the drainage.

Lastly, the short paleoseismic record at Crescent City limits comparison to the last 3000 years of record at some sites, but only the last $\approx$ 1200 years at the best comparative site, Elk Creek. The relative sizes of turbidite beds have been used as a rough measure of earthquake size (Goldfinger et al. [20]). In that comparison, none of the youngest events within the time range of interest (Peterson et al. [43]) are among the largest four events of the last 10,000 years of paleoseismic record, thus it is unlikely that the tsunami record at Crescent City contains a "2500 year" event for comparison to the models. The slip models of paleoearthquakes remain unknown, of course; thus, at any given location, such comparisons to broad regional trends could render them meaningless.

We conclude that results of this study and the paleotsunami records of [43] are broadly compatible. The tsunami record itself is closely comparable to the offshore record and nearby deep-water paleoseismic sites using turbidites (Goldfinger et al. [20]). Comparisons, however, are somewhat limited by the inadequate spatial sampling of the available core sites at the landward limits of inundation, and the relative insensitivity of both datasets to the lateral limits of inundation, an effect of topographic control.

8 Overview of tidal uncertainty

The range of inundation as well as the depth of flooding can vary significantly depending on the tidal stage when the largest waves arrive. This is shown in Figure 38 for the L1 Cascadia tsunami where GeoClaw simulations at mean low low water (MLLW) and at mean high high water (MHHW) are compared. Including tidal uncertainty into PTHA is extremely important.
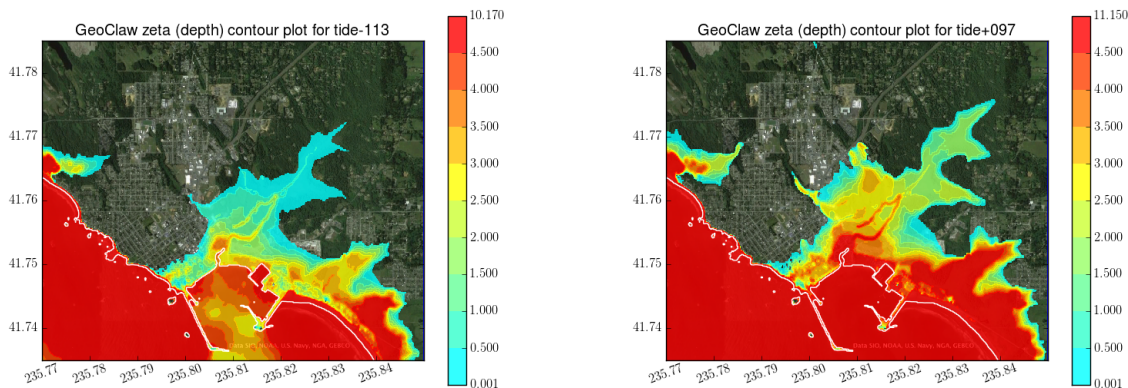

Figure 38: Tidal Impact on CSZRe03r01 Left: GeoClaw Data from MLLW simulation; Right: GeoClaw Data for MHHW simulation

The GeoClaw code is not modeling the tidal dynamics (i.e. the rise or fall of the tide within a single simulation, or how tidal currents could effect the inflow of the tsunami wave.) This limitation might be important to address and is a potential R&D topic. In this study, we used the newly developed Pattern-Method [3] for incorporating the tidal effects as best we can given this limitation. Refer to Appendix B where we describe how we compute the probability of exceeding prescribed ζ, speed or momentum flux levels.

A tsunami wave that arrives at high tide will cause more flooding than the same wave arriving at low tide. But nonlinearities in the governing equations mean that there will be nonlinearities in the tsunami-tide interaction. For example, if the tide stage is 1 meter higher, the resulting maximum flow depth at a point will not generally be exactly 1 meter higher, even at points that are inundated at both tide levels.

Unlike the flow depth ζ, the speeds and momentum flux vary differently with the tide level at different locations. At some locations, these quantities may increase with increasing tide level, at some they may decrease, and at other locations the behavior is neither increasing nor decreasing over the entire tidal range. The GeoClaw code can easily be set to run with different (static) values of sea level in order to explore how the tide stage, denoted ξ relative to MSL, affects the quantity of interest. Since the tide at Crescent City, CA ranges from -1.83 to 1.50 meters above MSL, GeoClaw runs should adequately represent the behavior of the quantity of interest across this range.

Our Phase 1 work concentrated only on flood depths (defined as ζ or η) and they were monotonically increasing (or non-decreasing) with increased tidal level, and as a result using only the tide levels -0.75 (MLW), 0.00 (MSL), and 0.97 (MHHW) was sufficient to determine a piecewise linear relationship between tide level and the quantity of interest.

The behavior of the speed and momentum flux can still be modeled with a piecewise linear function if more tidal levels are included. We first ran the Tohoku tsunami at 12 tide levels covering the Crescent City range. Based on these results, we determined that including -1.13 (MLLW) and 0.77 (MHW) to the three Phase 1 levels, for a total of 5 levels per tsunami is sufficient. The Pattern-Method was adjusted as suggested in [3] to find tide intervals where each chosen exceedance level would be exceeded instead of a single value.

8.1 Crescent City tides

The tidal gauge at Crescent City (Gauge No. 9419750) has the following values for Mean Low Low Water (ξ_{MLLW}), Mean Low Water (ξ_{MLW}), Mean Sea Level (ξ_{MSL}), Mean High Water (ξ_{MHW}), and Mean High High Water (ξ_{MHHW}), respectively. In addition, we include the Lowest (ξ_{Lowest}) and Highest ($\xi_{Highest}$) water seen at the gauge in a year's data from July 2011 to July 2012. Unless explicitly stated, the tide levels we use are referenced to MSL.

Level	Referenced to MSL
ξ_{Lowest}	-1.83
ξ_{MLLW}	-1.13
ξ_{MLW}	-0.75
ξ_{MSL}	0.00
ξ_{MHW}	0.77
ξ_{MHHW}	0.97
$\xi_{Highest}$	1.50

Table 2: Crescent City tide values values, measured in meters relative to MSL.

A fixed number of bins is made from tide levels $-1.83 \leq \xi \leq 1.50$. Then the yearly tide data at Crescent City is associated with the appropriate bin to make the probability density function and associated cumulative distribution function shown in Figure 39. In the cumulative distribution plot, the horizontal axis represents tidal level and the vertical axis the probability of exceedance of this level at any point in time. If the duration of a tsunami was extremely short (instantaneous, for example), this cumulative distribution would be the correct one to give the probability that a particular tide level would be exceeded when the tsunami occurred. However, tsunamis last for many hours and consist of multiple waves of varying amplitudes. The Pattern-Method finds an appropriate cumulative distribution for each particular tsunami.
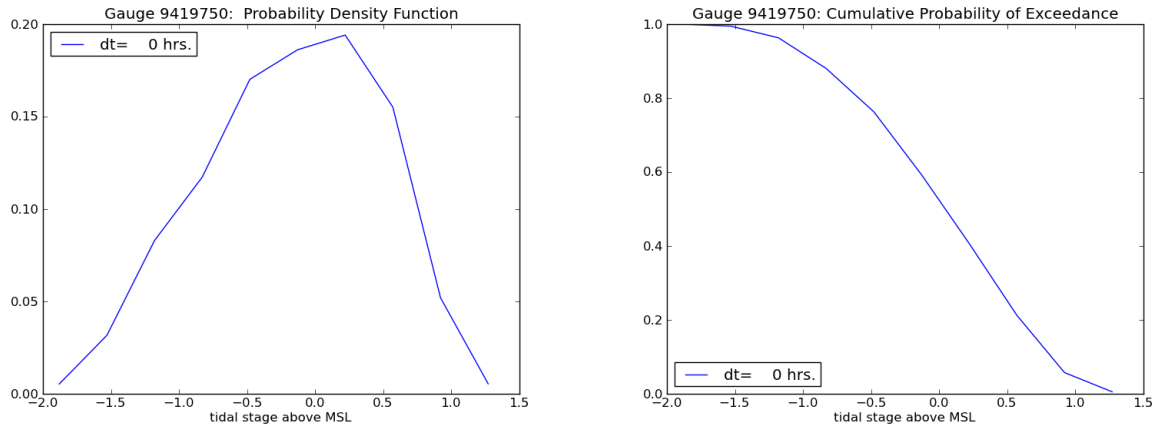
Figure 39: Crescent City Tidal Distributions (July 2011 - July 2012) Left: Probability Density Function (mean=0.0, $\sigma = .638$) Right: Cumulative Distribution Function

8.2 Pattern-Method summary

As mentioned in Appendix B, in order to add tidal uncertainty, we must be able to find the probability that the quantity of interest (ζ, speed, or momentum flux) exceeds a particular level (ζ_i, speed$_i$, mflux$_i$)

given that an event (or a realization of an event) actually occurs. The Pattern-Method is a procedure for finding $P(\zeta > \zeta_i \,|\, E_{jk})$, $P(\text{speed} > \text{speed}_i \,|\, E_{jk})$, or $P(\text{mflux} > \text{mflux}_i \,|\, E_{jk})$, the conditional probability of exceedance given that realization k of event j has occurred. It was developed for use in the Phase I work where the quantity of interest was inundation depth. For this work, we have further developed this method as mentioned in [3] to work with non-monotonic quantities of interest such as speed and momentum flux. A short description of the procedure is given below.

Each tsunami has a pattern of waves that is combined with a yearly Crescent City tide record to create the tsunami's cumulative distribution that gives the probability of exceeding each tide level with such a pattern. This pattern of waves is taken from a computational gauge called Gauge 101, depicted in Figure 2. It is important that the gauge that is used to record the pattern is in a water location that will have an increasing linear relationship (slope nearly 1) with the tide level. Our Gauge 101 is sufficient for this purpose across all the tsunamis we studied.

Values of the quantity of interest (inundation depth, speed, momentum flux) from GeoClaw runs at multiple tide levels are used to determine the behavior as a function of tide level. We use the 5 tide levels described above to construct a piecewise linear curve for each quantity of interest for each tsunami. This curve tells us intervals of tide values where each exceedance level is exceeded. We then use the tsunami's cumulative distribution to determine the probability that exceedance occurs by considering each of the intervals.

This procedure is an advance over methods that work only for monotonically non-increasing quantities of interest such as flow depth. It is more general, and in fact we also apply it to our depth quantity ζ in this study as well as the speed and momentum flux.

Validation of the Pattern Method

The method of Mofjeld, et.al [40] assumed a proxy tsunami of a given amplitude, a 20 minute period, and a two-day e-folding decay time that lasted 5 days to create a probability density function and related distribution for exceedance of a specified ζ level. These formulas were converted to distributions of the tide stage, and compared to what the Pattern Method would give *if* the tsunami seen at Gauge 101 were this proxy tsunami. We then ran the Pattern Method on this proxy tsunami (with amplitude taken as that of the biggest wave seen at Gauge 101 for AASZe03) and created the Pattern Method cumulative distribution. The two when plotted are almost identical with values differing mostly less than 1% as seen in Figure 40 as the green and dashed red graphs.

This explains any differences generated by the Mofjeld method and the Pattern Method at the Gauge 101 for any real tsunami is not due to our methodology, but to the fact that the real tsunami is not well approximated by the proxy one. The Pattern Method can capture the differences of each specific tsunami as seen in Figure 40 by the differences between the black graph and the green (or dashed red) ones.
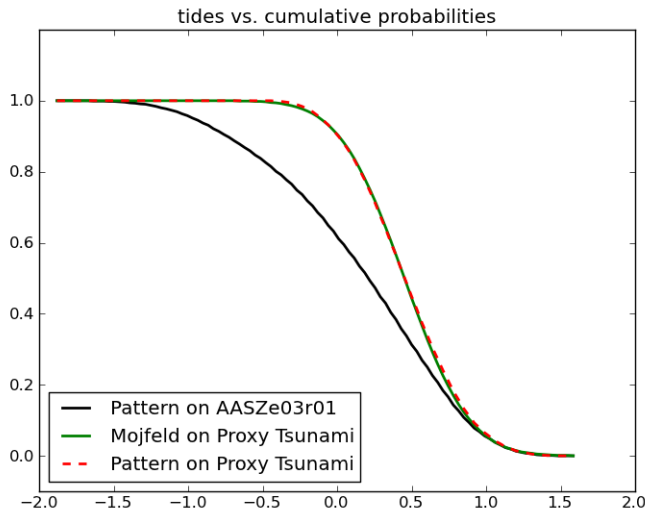
Figure 40:   Pattern Method Validation

9   Deliverable maps and additional products

9.1   Deliverable maps – ζ, speed, momentum flux, and η contour maps

The deliverable maps required by FEMA are the 100-year and 500-year hazard maps for ζ, speed, and momentum flux which are shown in Section 3, and that for η found in Appendix C. In this section we discuss some other ways to visualize probabilistic results that may be useful to consider. These additional products of potential value are referred to as p-contour maps, transects, hazard p-contour maps and curves deaggregated by earthquake zone, and summary snapshots.

9.2 p-contour maps

We believe that viewing only 100-year and 500-year maps may be misleading and that more information is available than is displayed in this format. In this section we point out the limitations and suggest some other products that may be useful to consider.

Our main concerns with the deliverable maps are:

- The lines showing maximum inundation at the probability levels $p = 0.01$ and $p = 0.002$ can be highly sensitive to changes in the input (such as the recurrence time of some events) and also to the choice of these two particular p values.

- There is the possibility of much greater inundation distances than shown on either of the above maps, if it has probability less than 0.002. It may be useful for emergency managers to know about the potential for greater flooding than is shown on these maps, even if the probability is less than the somewhat arbitrary value of 0.002.

To give an illustration of these concerns, consider a simplified hypothetical case in which there is only one possible earthquake in the study — one particular CSZ Mw 9.1 event realization and suppose it has a recurrence time of 499 years. Then our methodology would result in the 500-year map shown on the left in Figure 41, with a large region of possible inundation.

Now consider the same situation but suppose the recurrence time for this one event is 501 years rather than 499 years. Then the 500-year map on the right in Figure 41 results. This map shows no inundation at all, since at every (x, y) point the probability of $\zeta > 0$ is either 0 or $1 - \exp(-1/501) \approx 0.001994 < 0.002$.

Similarly, if we left the recurrence time at 499 years but plotted the inundation map for $p = 0.00201$ rather than for $p = 0.002$, the hazard map would again change to that on the right in Figure 41 since $1 - \exp(-1/499) \approx 0.002002 < 0.00201$.

The above example illustrates that looking at contours of ζ for particular fixed values of p, such as 0.01 and 0.002, can fail to show significantly greater potential inundation that is only slightly less probable.

The ζ-contour maps for fixed p are useful, since they give not only a view of the region inundated with these probabilities but also the depth of inundation at each point that can be expected with these annual probabilities. However, we believe that in addition to these maps it would be useful to also view maps that show *contours of probability* for which a particular inundation depth $\bar{\zeta}$ is exceeded. These are also easily generated from the hazard curves that are generated in our PTHA methodology. At each grid point (x, y) in the region of interest, the hazard curves show directly the probability of exceeding $\bar{\zeta}$. Evaluating this at each grid point allows generating a contour map of p for this $\bar{\zeta}$.

Note in particular that choosing exceedance value $\bar{\zeta} = 0$ will then show the contours of probability for any inundation (i.e., $\zeta > 0$) at each point. In particular the $p = 0.01$ contour of this map will be the limits of the region that experiences any flooding with probability 0.01 and should agree with the limits of the inundation region shown on the 100-year hazard map.

Figure 42 shows contours of p for the exceedance value $\bar{\zeta} = 0$ for the simple examples used above to illustrate sensitivity. (Actually these show a color map in which color indicates probability, and the boundary between colors are contour lines.) Again the plot on the left is what is obtained if we assume a recurrence time of 499 years for the one event considered, and the plot on the right is if we assume a recurrence time of 501 years. The two plots now look very similar, though the color is slightly different indicating a slight change in the probabilities. However the $p = 0.002$ contour line is near the outer limits of the colored region in the left plot while in the right plot there is no region with $p \geq 0.002$.

It may also be useful to look at contour plots of p for different choices of exceedance level $\bar{\zeta}$. For example, choosing $\bar{\zeta} = 1m$ would show probabilities of exceeding 1 meter of inundation at each point. There may be particular depths that are considered hazardous and more meaningful to consider than $\bar{\zeta} = 0$. Some examples are given in the next section.
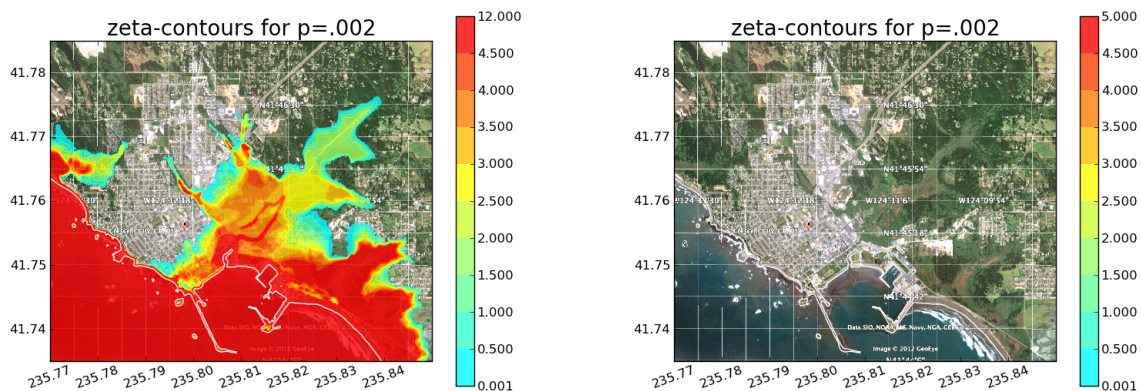

Figure 41: ζ-contours for p=.002 when only one sample event is considered. Left: assuming recurrence=499 years. Right: assuming recurrence=501 years.
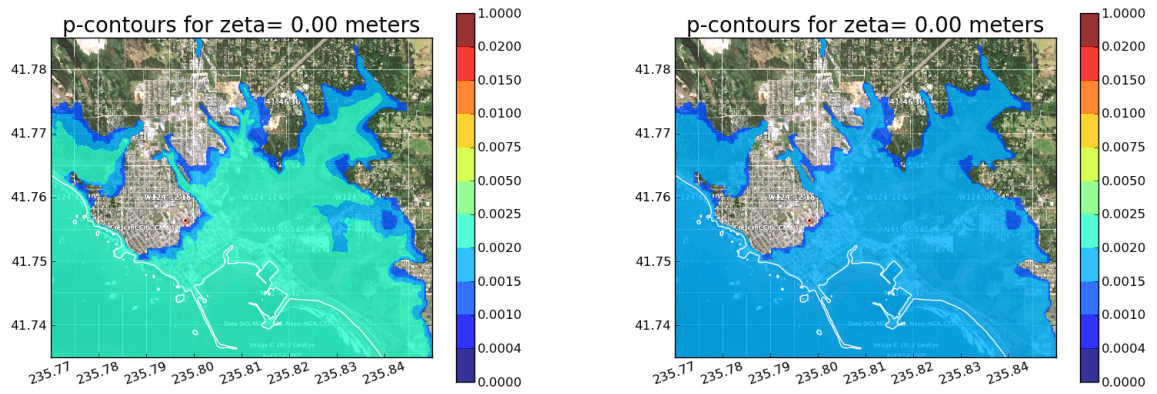
Figure 42: p-contours for $\zeta = 0$ m, when only one sample event is considered. Left: assuming recurrence=499 years. Right: assuming recurrence=501 years.

9.3 Sample p-contour maps

Figure 43 shows p-contours for exceedance level $\bar{\zeta} = 0$ based on the same set of events used for the deliverable maps shown in Section 3 and Appendix C. Note that the $p = 0.01$ contour of Figure 43 agrees with the extent of inundation shown in Figure 3, and the $p = 0.002$ contour of Figure 43 agrees with the extent of inundation shown in Figure 6. Black lines in the figures mark the $p = .01$ and $p = .002$ contours and the white line is the shore line associated with $B = 0$. Figure 44 shows p-contours for different values of exceedance $\bar{\zeta}$.
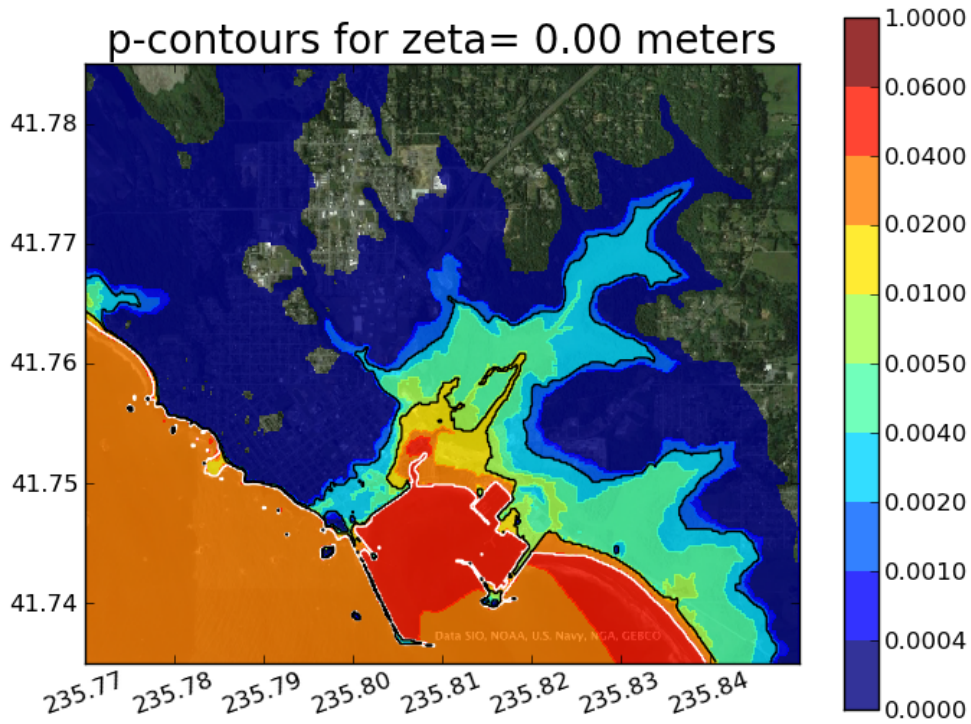
Figure 43:   p-contours, ζ=0.0 meters, with the study sources of Table 1. This includes the Bandon study sources for CSZ with $T_M = 250$ years and a representative Japan source with $T_M = 103$ years.
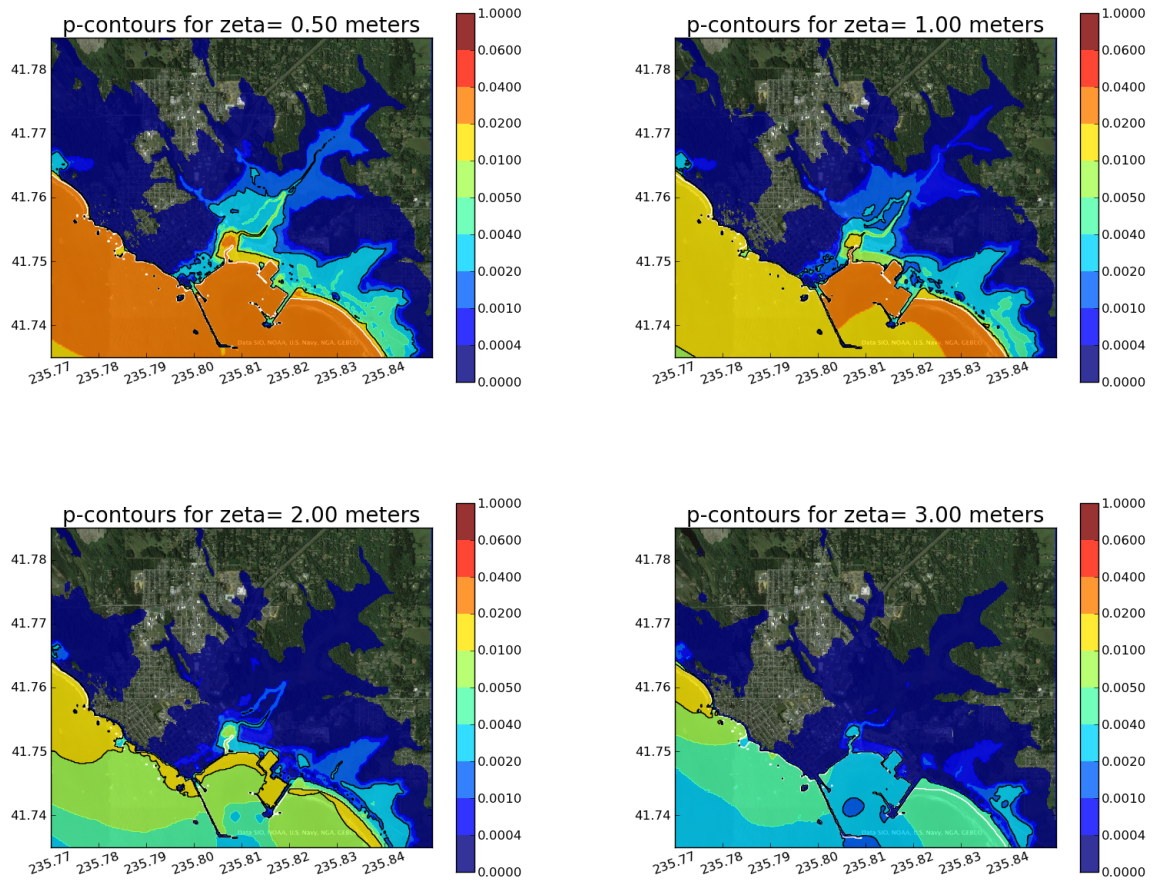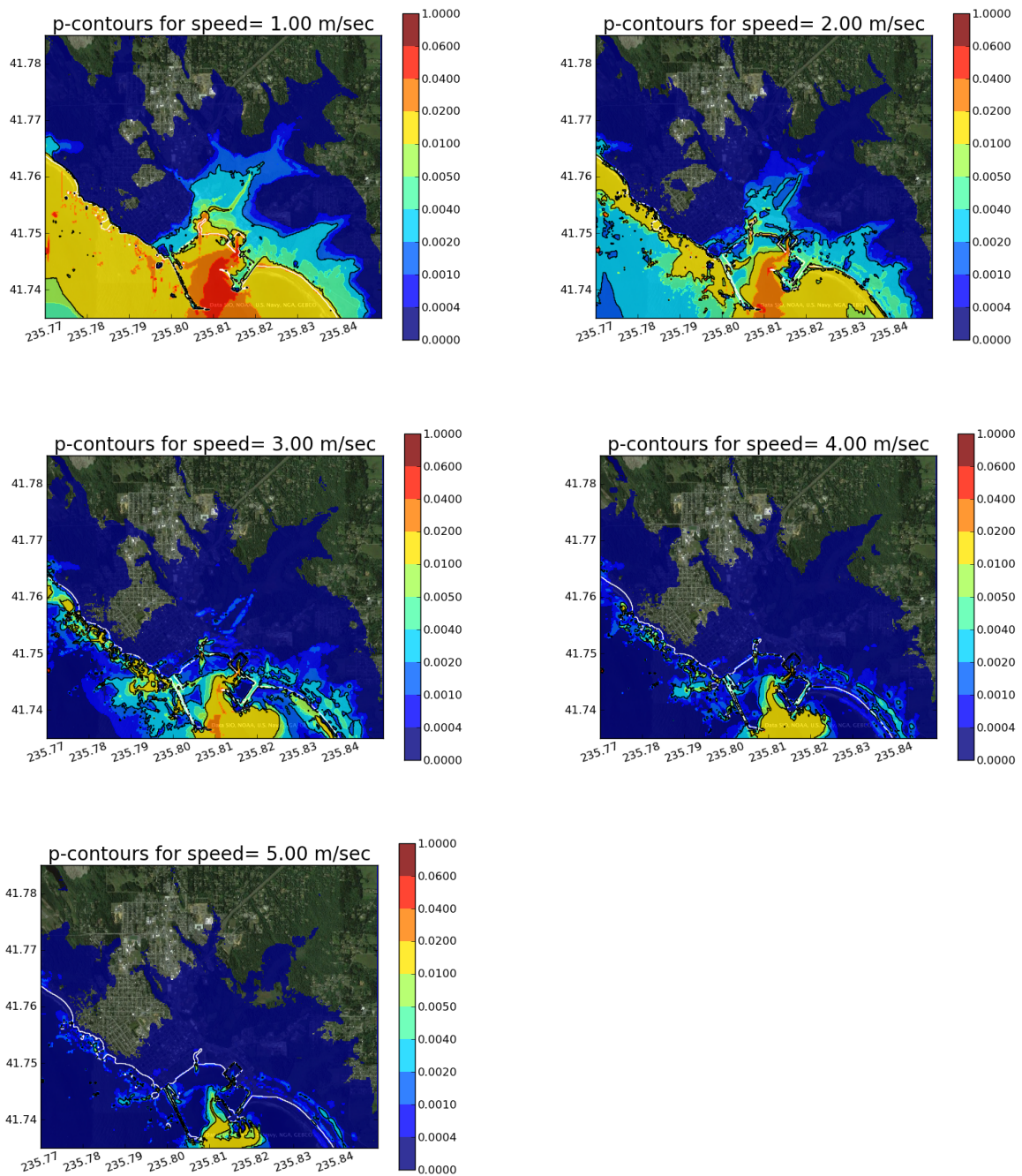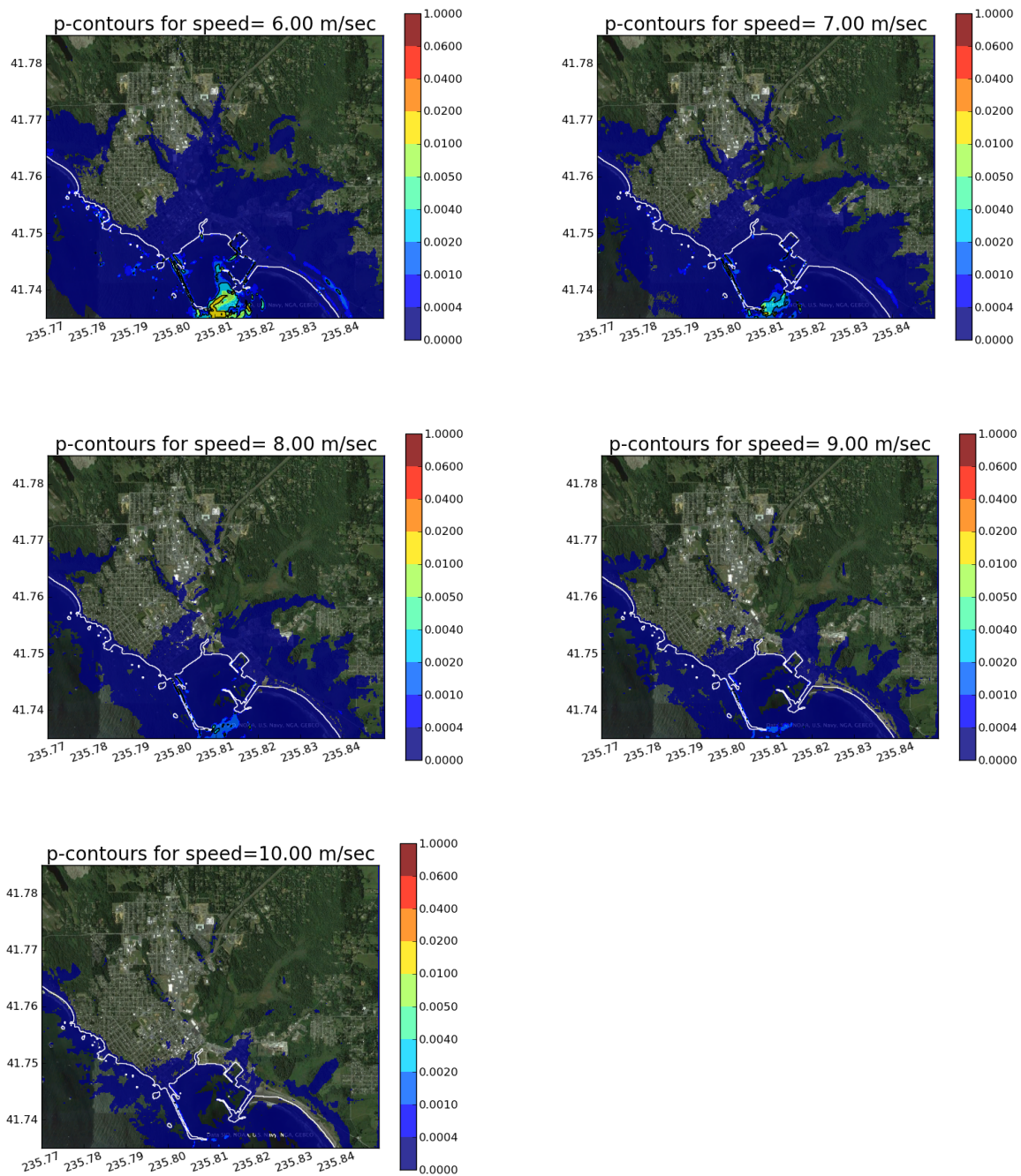
Figure 44: p-contours for ζ for other exceedance levels.

Figure 45 shows p-contours for speed exceeding level speed=0 based on the same set of events used for the deliverable maps shown in Section 3. Note that the $p = 0.01$ contour of Figure 45 agrees with the extent of inundation shown in Figure 4, and the $p = 0.002$ contour of Figure 45 agrees with the extent of inundation shown in Figure 7. Black lines in the figures mark the $p = .01$ and $p = .002$ contours and the white line is the shore line associated with $B = 0$. Figure 46 and Figure 47 show p-contours for speed exceeding different levels, ranging from 1 to 10 meters per second.
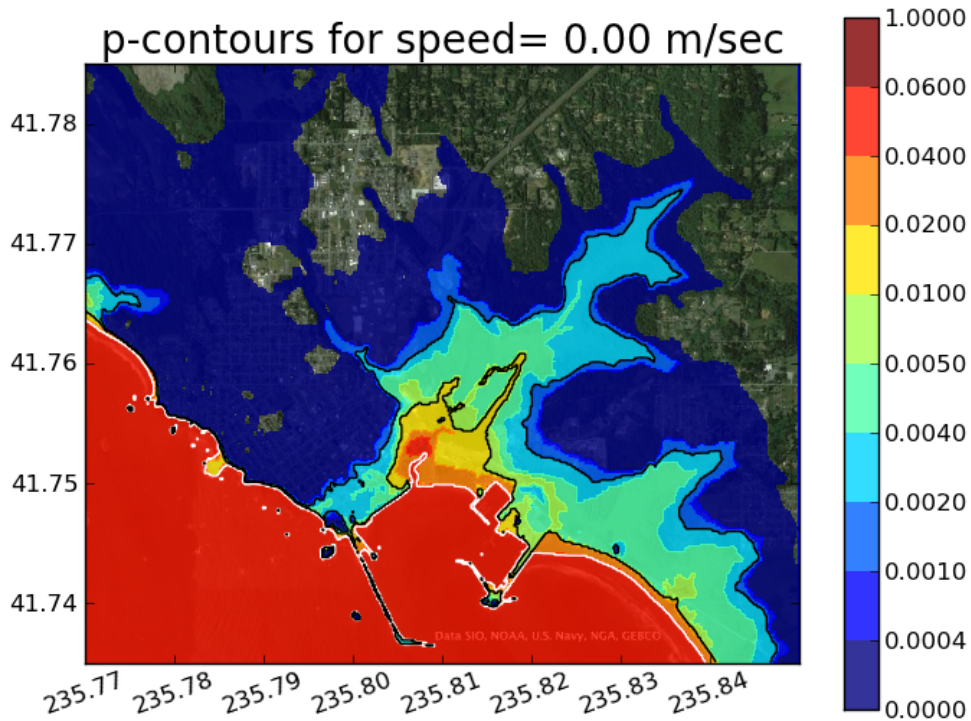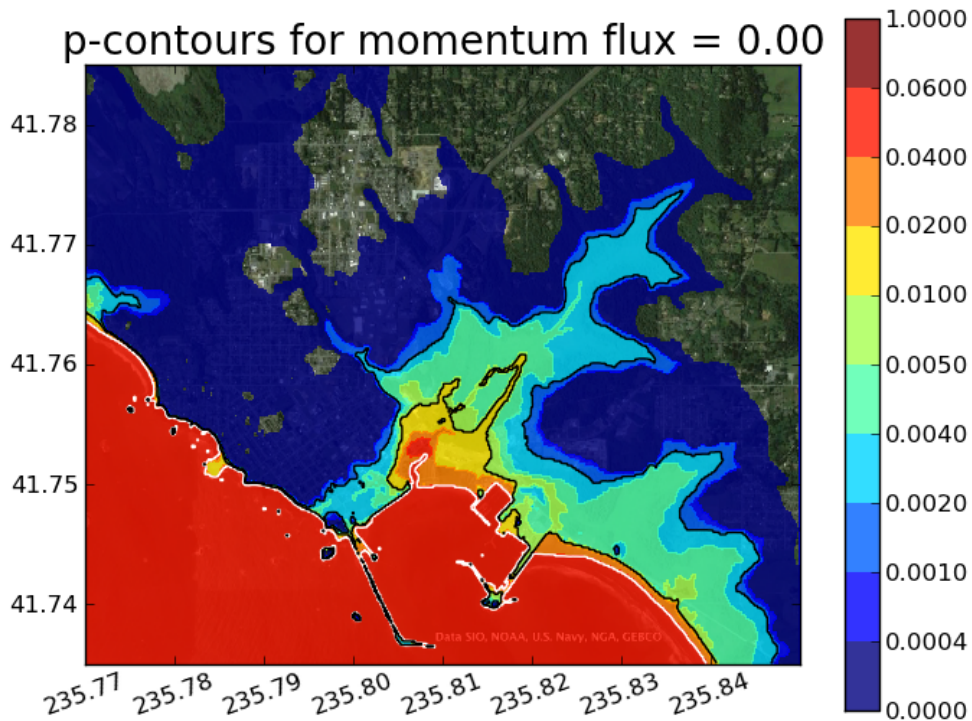

Figure 45:   p-contours, speed=0.0 meters, with the study sources of Table 1. This includes the Bandon study sources for CSZ with $T_M = 250$ years and a representative Japan source with $T_M = 103$ years.

Figure 46: *p*-contours for exceeding speeds 1 to 5 m/sec.

Figure 47: *p*-contours for exceeding speeds 6 to 10 m/sec.

Figure 48 shows p-contours for momentum flux exceeding level mflux=0 based on the same set of events used for the deliverable maps shown in Section 3. Note that the $p = 0.01$ contour of Figure 48 agrees with the extent of inundation shown in Figure 5, and the $p = 0.002$ contour of Figure 48 agrees with the extent of inundation shown in Figure 8. Black lines in the figures mark the $p = .01$ and $p = .002$ contours and the white line is the shore line associated with $B = 0$. Figure 49 shows p-contours for momentum flux exceeding the levels 0.1, 1.0, 10.0 and 100.0 m^3/s^2.

Figure 48:   p-contours, mflux=0.0, with the study sources of Table 1. This includes the Bandon study sources for CSZ with $T_M = 250$ years and a representative Japan source with $T_M = 103$ years.
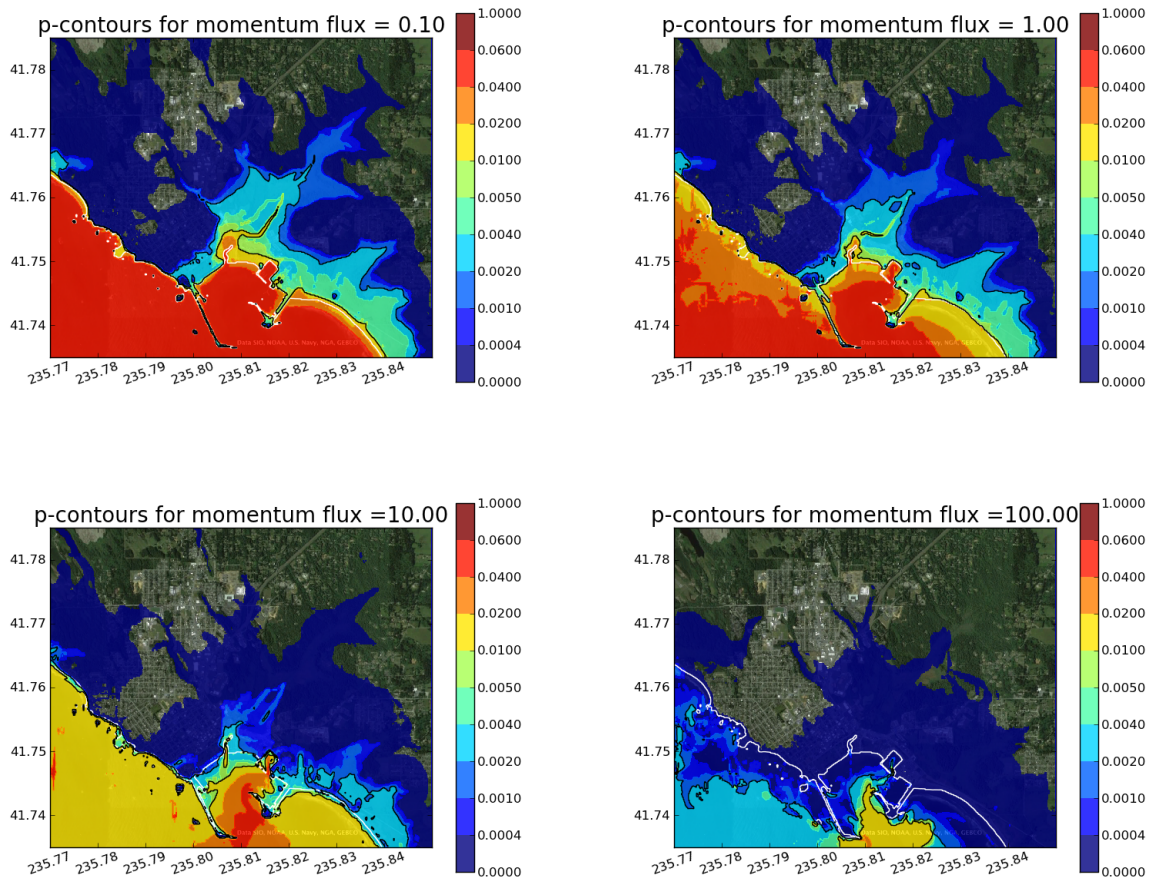
Figure 49: p-contours for mflux exceeding 0.1, 1.0, 10.0, and 100.0 m^3/s^2

9.4 Transects

In addition to contour plots, it is also useful to view one-dimensional transects of the results. Figure 50 and Figure 51 show two examples of such plots. In each case there is a plot of cross sections of the 100-year and 500-year inundations (ζ at fixed probabilities $p = 0.01$ and $p = 0.002$), corresponding to Figure 3 and Figure 6, and also cross sections of the probability of exceeding various ζ values corresponding to Figure 43 and Figure 44. We note that these transects were actually computed based on the corresponding Phase 1 report results. We did not recompute them with the new output, but include them here to show what products are possible to generate if desired.
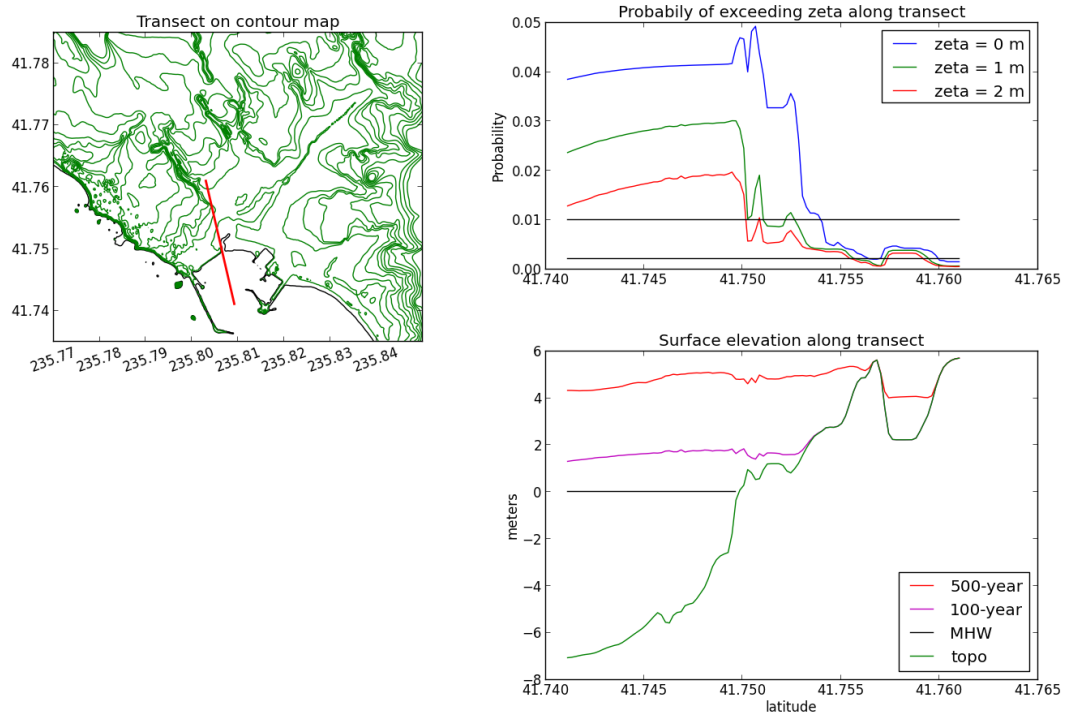
Figure 50: Sample transect plots.
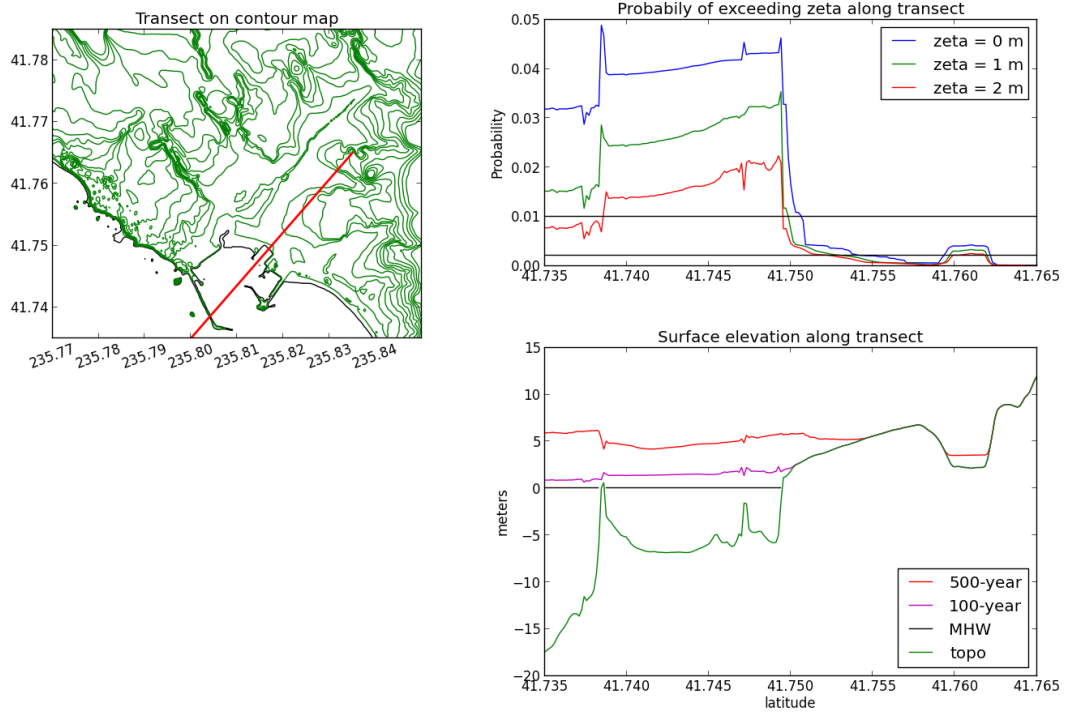
Figure 51: Sample transect plots.

9.5 Hazard by earthquake zone results

Figure 52 breaks down the p-contour plot in Figure 43 for $\zeta = 0$ by earthquake zone. Figure 53 breaks down the p-contour plot in Figure 45 for speed $= 0$ by earthquake zone. Likewise, Figure 54 breaks down the p-contour plot in Figure 48 for mflux $= 0$ by earthquake zone.

The hazard curve at a given location can also be deaggregated by earthquake zone. In Figure 55, Figure 56, and Figure 57, we show each zone's influence on the total hazard at Gauge 101 in the harbor, at a location in the boat harbor near Gauge 102, and at the Gauge 105 land location in Crescent City, respectively.
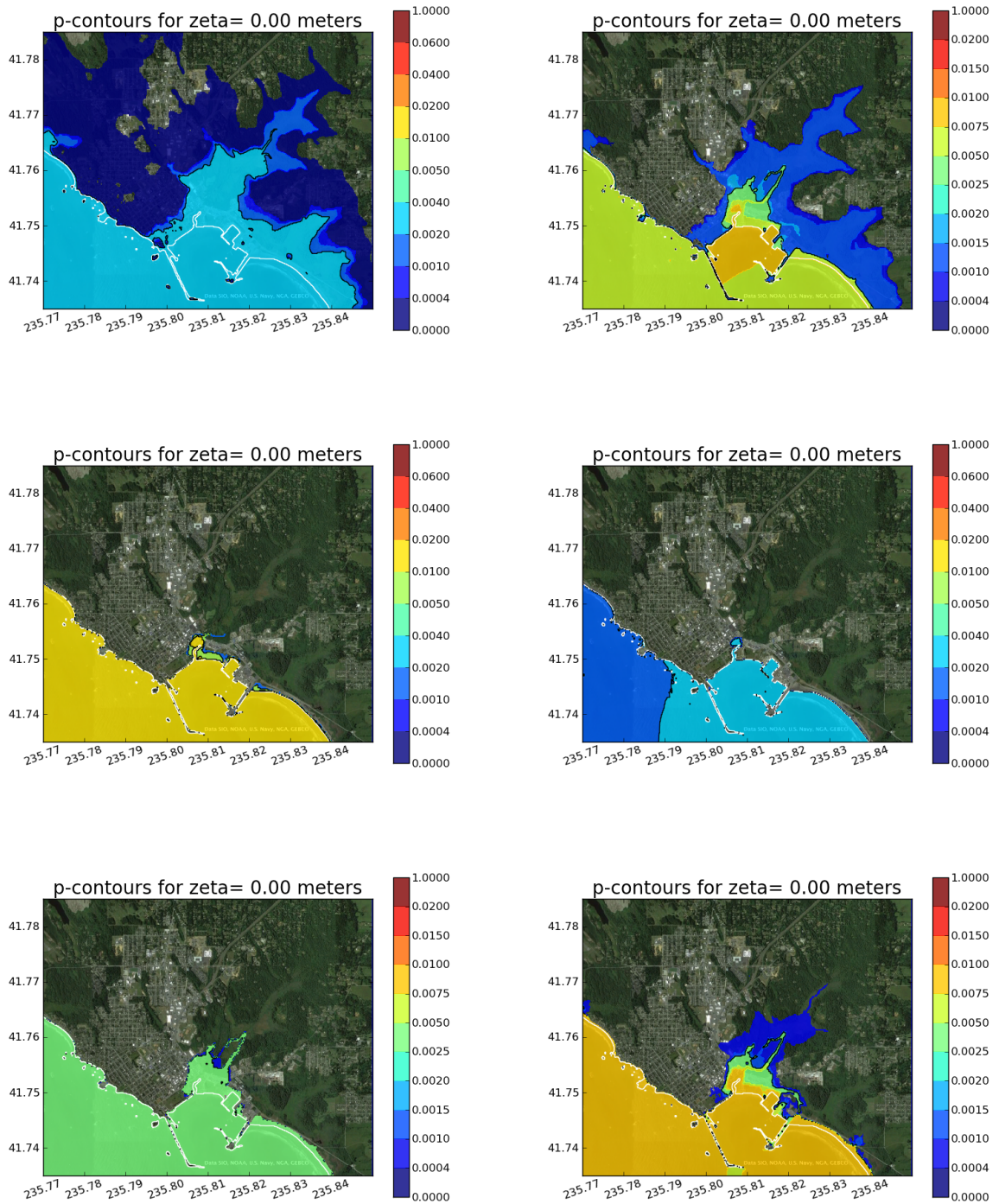
Figure 52: p-contours for $\zeta = 0$. Top left: Only Cascadia; Top right: All AASZ Only; Middle left: All KmSZ Only; Middle right: All KrSZ Only; Bottom left: SChSZe01 Only; Bottom right: TOHe01 Only
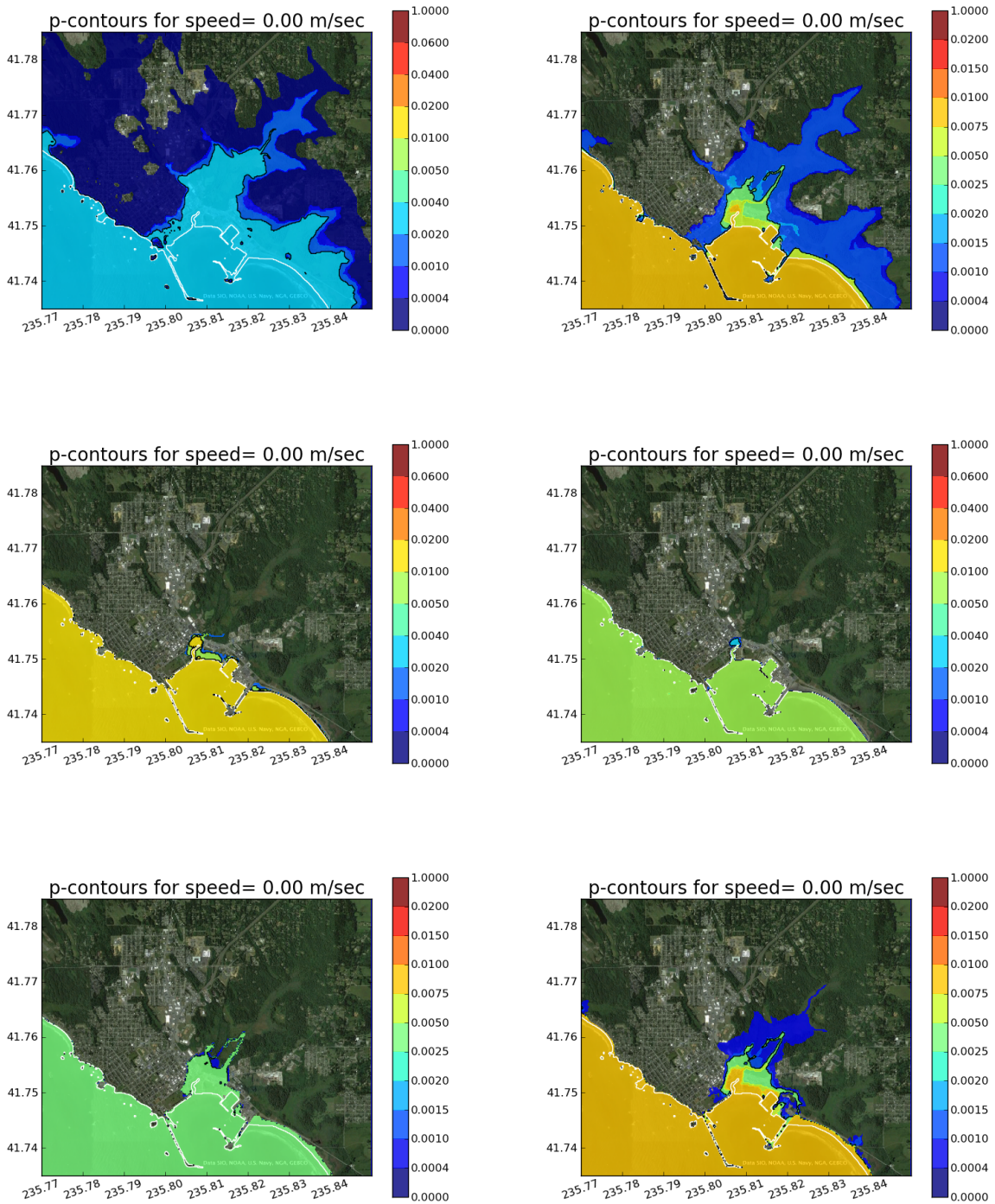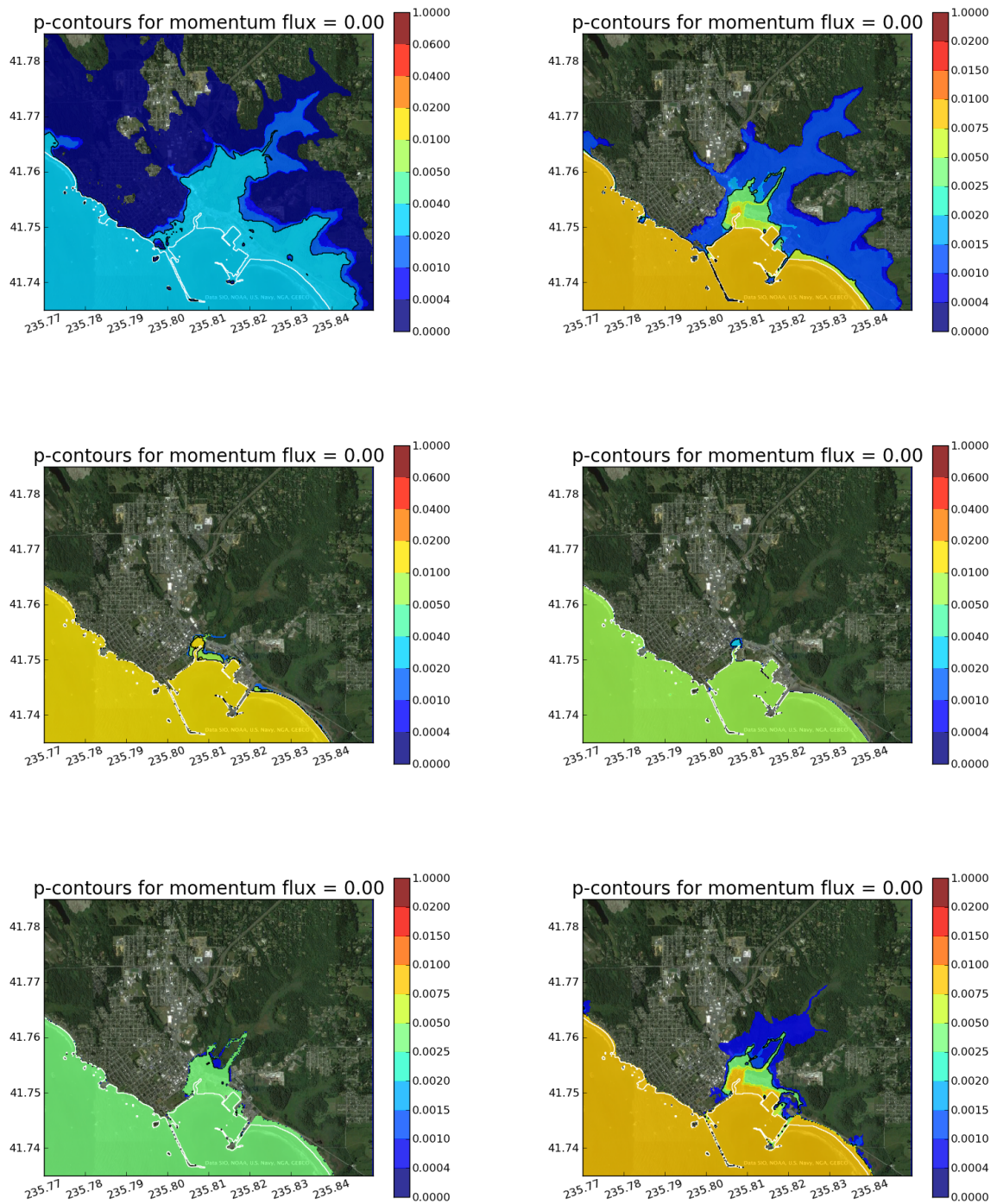
Figure 53: *p*-contours for speed = 0. Top left: Only Cascadia; Top right: All AASZ Only; Middle left: All KmSZ Only; Middle right: All KrSZ Only; Bottom left: SChSZe01 Only; Bottom right: TOHe01 Only
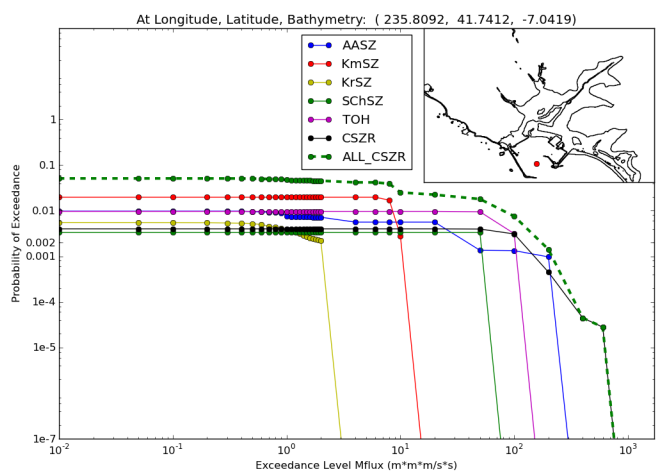
Figure 54: *p*-contours for mflux = 0. Top left: Only Cascadia; Top right: All AASZ Only; Middle left: All KmSZ Only; Middle right: All KrSZ Only; Bottom left: SChSZe01 Only; Bottom right: TOHe01 Only
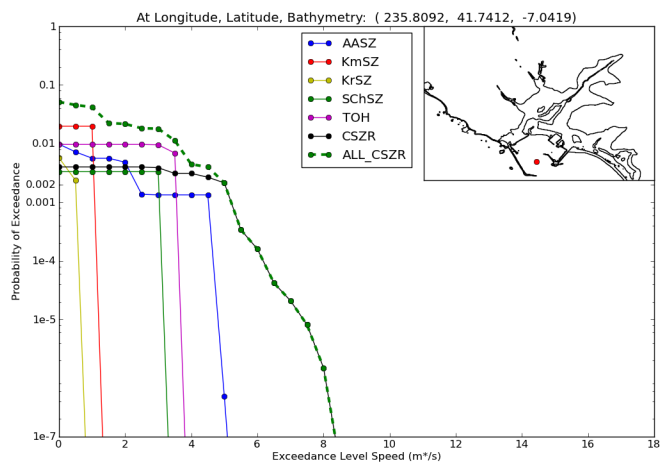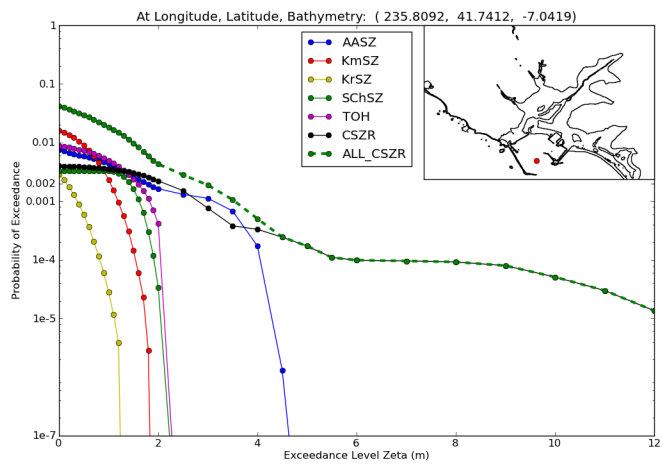
Figure 55:   Zone Hazard Curves for harbor location Gauge 101. Top: ζ; Middle: speed; Bottom: momentum flux
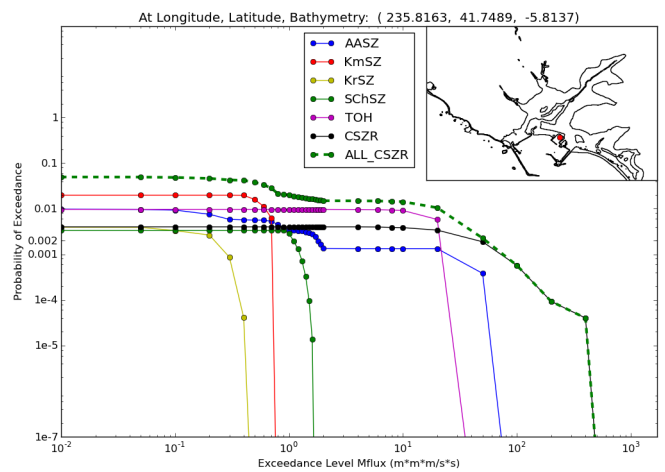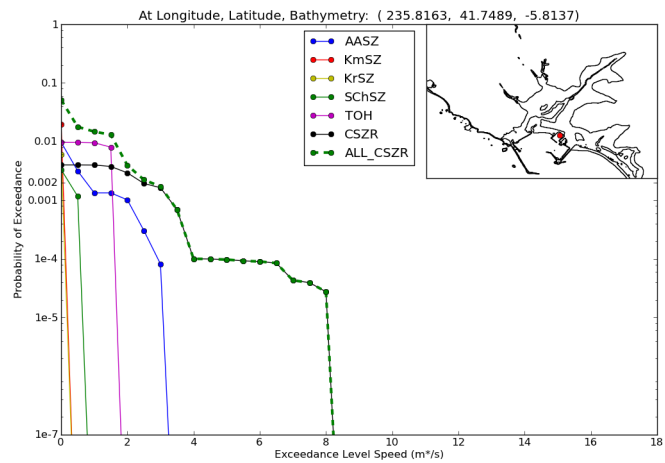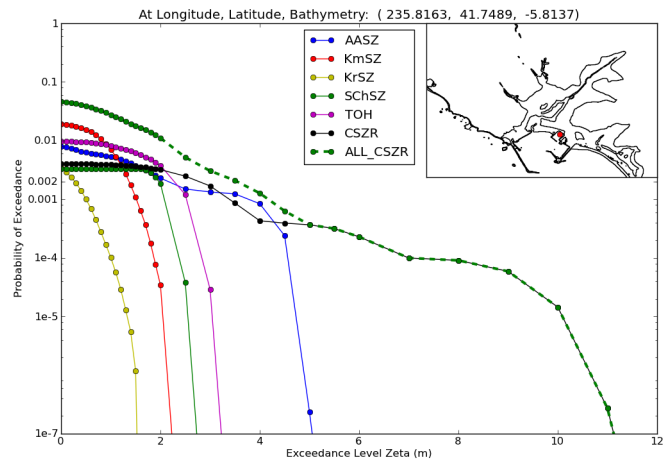
Figure 56: Zone Hazard Curves for a Boat Harbor location near Gauge 102. Top: ζ; Middle: speed; Bottom: momentum flux
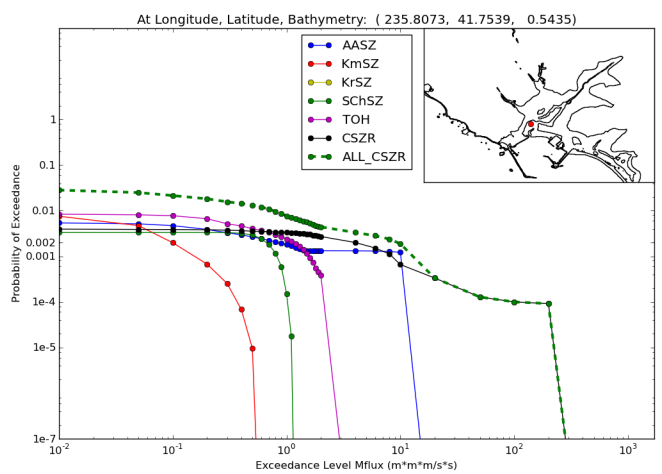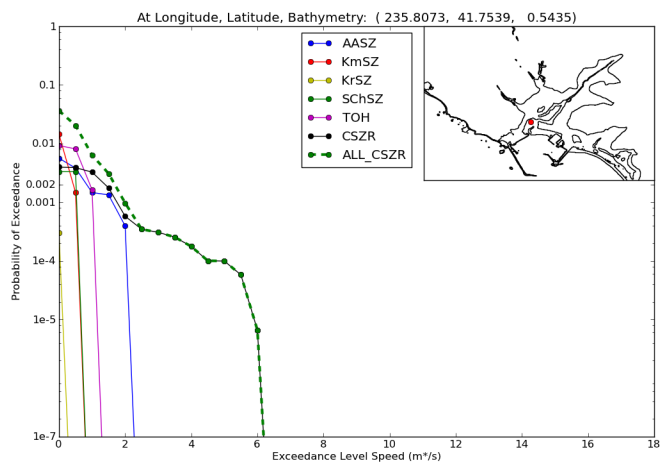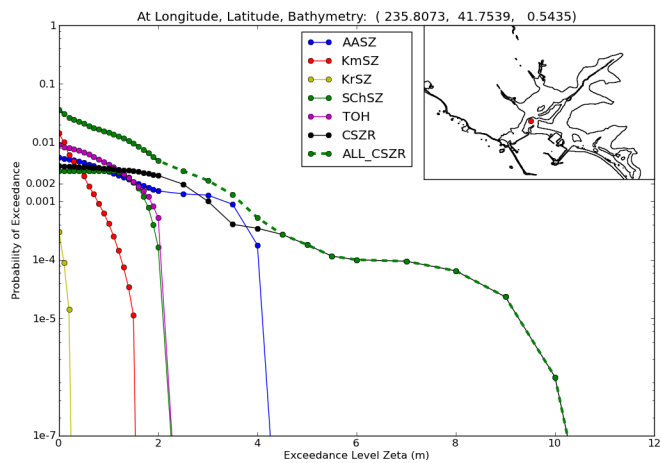
Figure 57: Zone Hazard Curves for land location Gauge 105. Top: ζ; Middle: speed; Bottom: momentum flux

9.6 Summary snapshots

Here we present hazard curves and probabilistic maps for all model-derived quantities of interest (wave height, flood depth, current speed and momentum flux) in a grid format that helps us examine several dependencies of these products on factors such as seismic source characteristics, site characteristics and mean recurrence intervals, in a qualitative way.

In Figure 58 we show the wave height η, flood depth ζ, current speed, and momentum flux 100yr, 300yr, 500yr, 975yr, 2500yr, and 5000yr floods in one large snapshot.

Figure 59 shows snapshots of p-contours for different exceedance levels for flood depth, current speed, and momentum flux.

Figure 60 show snapshots of hazard curves by earthquake zone. The dashed green line on each curve is the total for all zones. This figure includes a location on land (Gauge 105 at +0.5m topography), a location in the boat harbor (near Gauge 102 at -5.8m topography), and a location in the middle of the harbor (Gauge 101 at -7.0m topography).

Note that in all cases, at higher exceedance values the CSZ realizations are the only ones that come into play and so the black curve (CSZ) lies on top of the dashed green line (final hazard curve).

All hazard curves must be non-increasing functions of exceedance level. Hazard curves corresponding to a single event realization tend to be fairly flat with a precipitous drop at the the exceedance value corresponding to what was computed for this event, but are smeared out somewhat due to the incorporation of tidal uncertainty. The events of largest magnitude have small probability and so the zone hazard curves that go out farthest to the right also approach smaller probabilities as exceedance level approaches zero.

Note the variation in behavior of hazard curves between these three points, and recall that these are only three sample points out of the 467,965 points covering Crescent City that were used to generate the final hazard maps. Clearly there is a wealth of information about the physical behavior of tsunamis from different sources and their impact at different locations that could be explored further at a later date.

Mean Interevent Time, T_M (years)

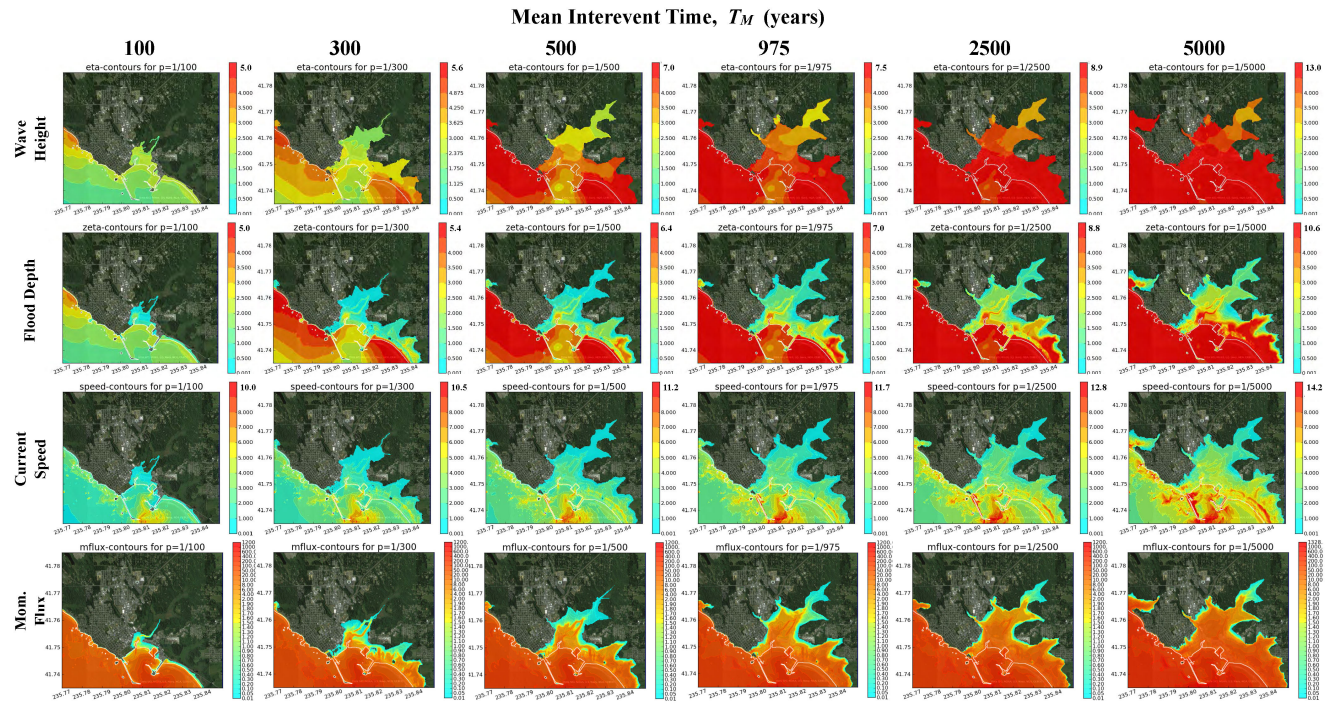| 100 | 300 | 500 | 975 | 2500 | 5000 |

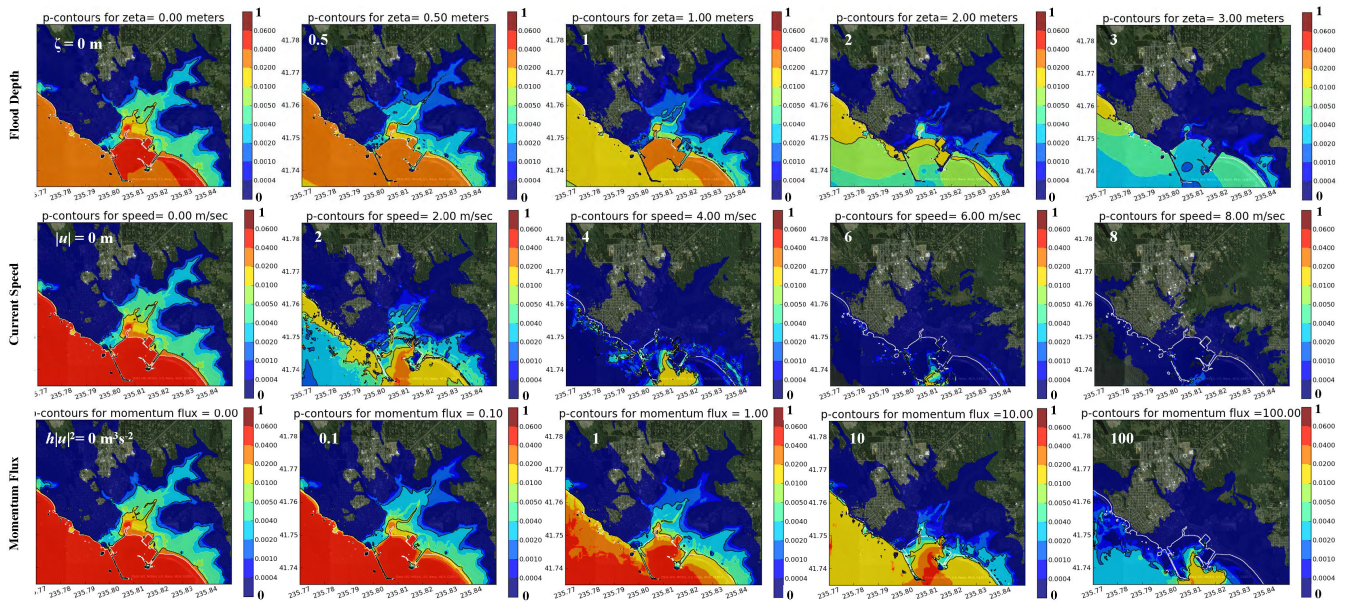Figure 58: Wave Height, Flood Depth, Current Speed, Momentum Flux Flood Maps

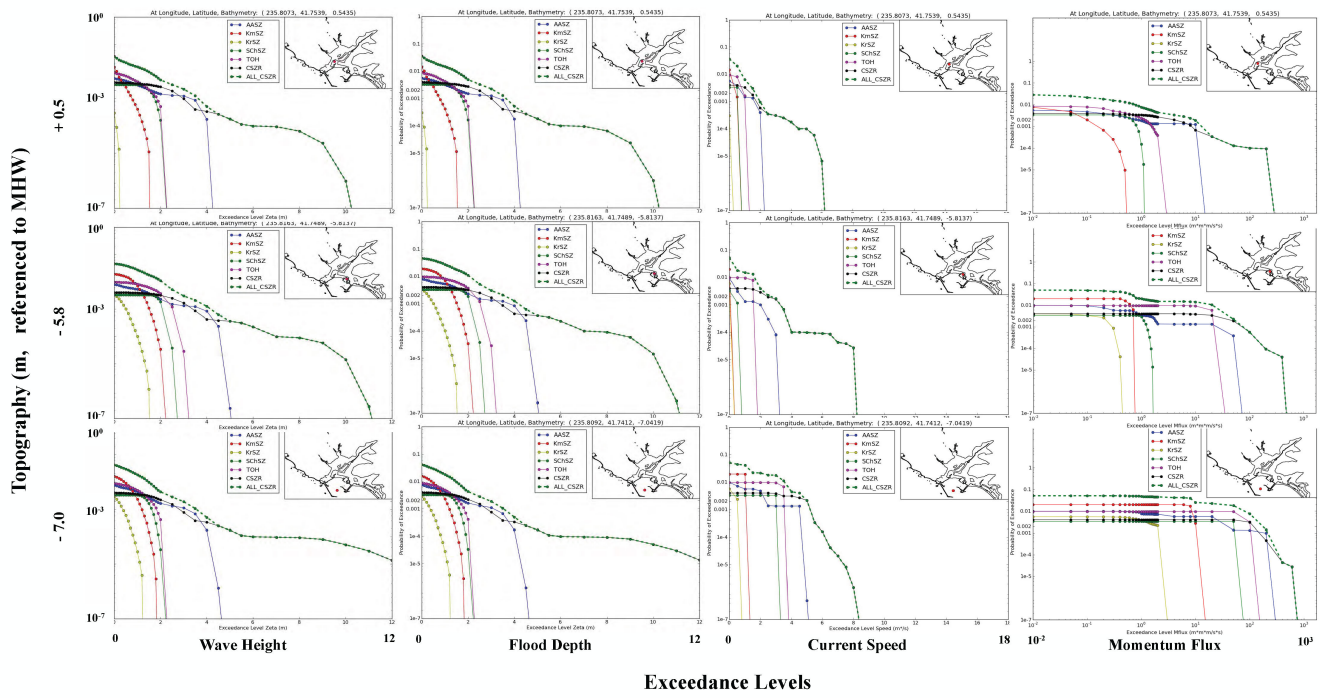Figure 59: Flood Depth, Current Speed, Momentum Flux p-contours

Figure 60: Hazard Curves by Earthquake Zone at Three Locations. Top: Gauge 105 Location; Middle: Boat Harbor Location (near Gauge 102); Bottom: Gauge 101 Location

10 Summary, results, and conclusions

The deliverable maps resulting from this work are the 100-year and 500-year flood maps based on our probabilistic modeling. These are presented in Section 3 and Appendix C. This modeling required the choice of a set of earthquake sources (seafloor deformation) along with the recurrence time for such an earthquake. A set of appropriate sources was developed in Section 7. The GeoClaw software described in Section 5 was used to perform a tsunami propagation and inundation simulation at five different static tide levels for each source. Tidal uncertainty was incorporated using a new "pattern method" technique discussed in Section 8. From all of these simulation results, a hazard curve can be computed at each grid point on the spatial grid covering Crescent City, as described briefly in Section 3.3 and more fully in Appendices A and B. From this set of hazard curves, the deliverable maps can be easily created by interpolating to find the inundation depth ζ for the probabilities $p = 0.01$ and $p = 0.002$.

The 500- and 2500- flow depth maps were compared with paleotsunami core data that were available in the Crescent City region. Section 7.7 provides an analysis and discussion of this comparison, which concludes that, within the temporal and spatial sampling limitations of the paleotsunami data, the probabilistic modeling results are broadly consistent with the currently available field data.

An interesting finding is that the speeds and the momentum flux vary drastically with location within Crescent City but do not vary as much with tide level changes as the depths (ζ) do. This can be seen in the GeoClaw raw data for depth, speed, and momentum flux for the Alaska (1964) tsunami at MLLW and MHHW in Figure 61 below. Similar patterns are seen for all 32 tsunamis in the study.
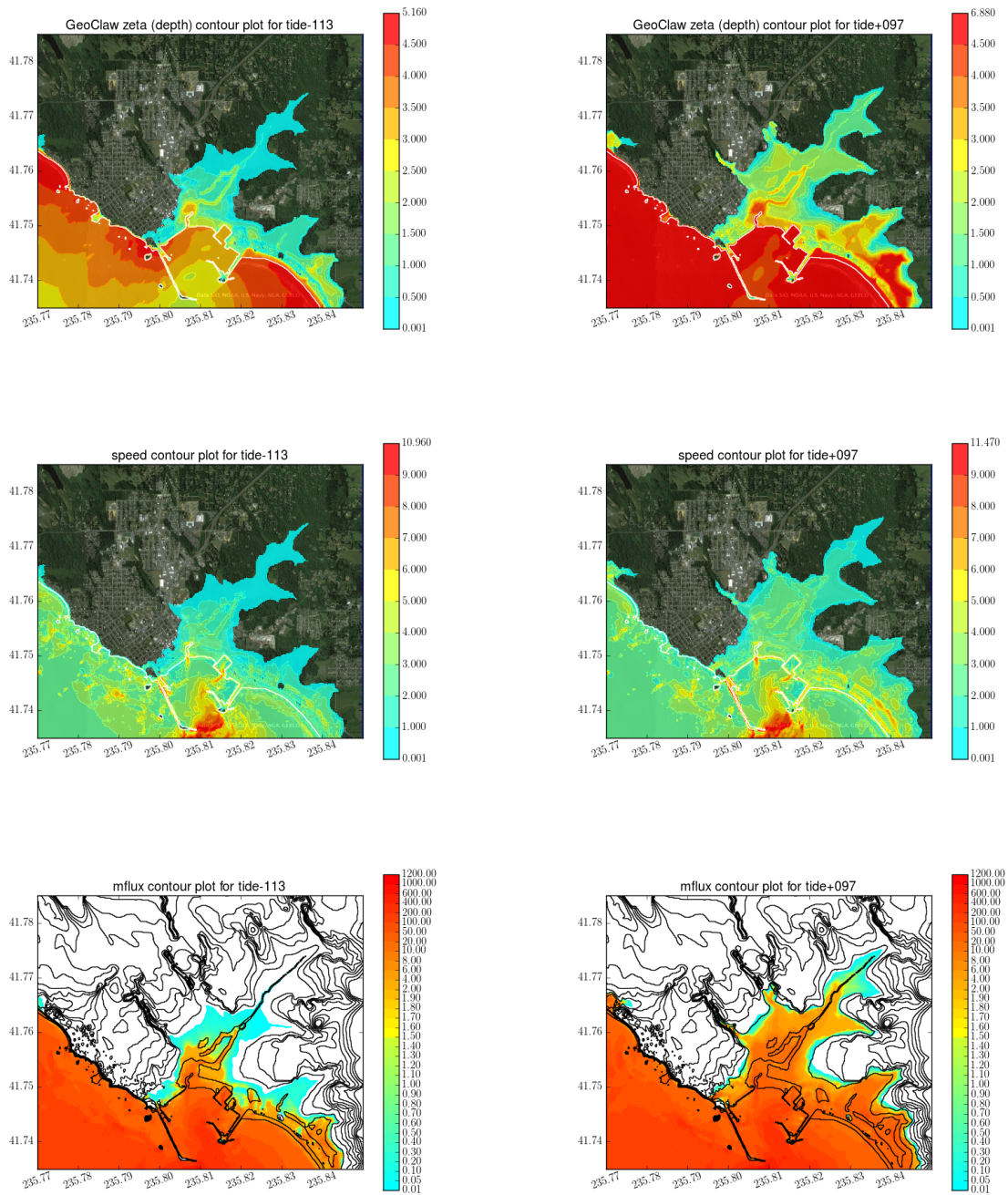
Figure 61: GeoClaw Data for Alaska 1964. Top left: ζ (MLLW), Top right: ζ (MHHW), Middle left: speed (MLLW), Middle right: speed (MHHW), Bottom left: mflux (MLLW), Bottom right: mflux (MHHW)

An implication of the observation above is that large speeds and momentum flux are possible at particular locations even when the tsunami arrives at a low tidal level. This was seen in our probabilistic results on speeds and momentum flux, and were actually observed in Crescent City for the Tohoku tsunami's damage to the boat harbor, which actually occurred when the tide was low. The Zone plots in Section 9.5 also show that the TOH zone contributes more to the probability for speeds less than 4 meters/sec than the AASZ zone for locations in the harbor and boat harbor. This is also due to the shorter return time of TOH tsunamis compared to Alaska ones.

Given the post-processed model output data that is used to construct the the probabilistic maps, it is also possible to create additional products, such as contour maps of probability for a fixed inundation depth, plots of any of these quantities along a one-dimensional transect, or deaggregated results by earthquake zone. In Section 9.2 we discussed some of the limitations of the deliverable maps and the possible complementary use of other products. These post-processed data that allow construction of such probabilistic products can be found at http://depts.washington.edu/ptha/CCpthaFinal.

10.1 Limitations and future directions

There are many limitations of the current study and the results should be viewed in this light. Some of the things that require further study are:

- Earthquake sources. We believe this is the largest source of error in the probabilistic results, since the epistemic uncertainty of determining the proper probability distributions of possible events has not been fully addressed.

- Our attempts at modeling tidal uncertainty are not perfect. Moreover we do not model the currents that are generated by the tide rising and falling. A tsunami wave arriving on top of an incoming tide could potentially inundate further than the same amplitude wave moving against the tidal current, even if the tide stage is the same. Modeling this is beyond the scope of current tsunami models.

- Instantaneous uplift is assumed. Some tsunami models include dynamic rupture and even the effect of finite acoustic speed in water, which results in a somewhat different displacement of the sea surface than the seafloor. Based on past validation of the code (Section 5.3 through 6.2), we do not think this will make a significant difference, particularly since the sea floor deformations are meant to be random samples rather than models of particular events.

- We have used the constant Manning coefficient $n = 0.025$ everywhere. It would be better to use a variable friction coefficient that takes into account the variable surface roughness. We have followed standard practice with use of this constant value.

- The topography is "bare earth" and does not include structures. This fact, together with the use of a relatively small Manning coefficient, means the inundation distances computed may be greater than they should be.

- The depth-averaged shallow water equations are less accurate in the inundation region, where three-dimensional effects can be important, than offshore. Moreover, the water will be mixed with debris onshore and become more of a debris flow rather than pure water, which might be better modeled by other equations.

Future improvements are planned for the GeoClaw software, such as spatially varying Manning friction coefficients that will allow for more accurate simulations.

Further improvements in probabilistic results might be accomplished if it were possible to better describe the probability distribution of potential events. This is primarily a geophysics problem, but we have started to explore some of the mathematical techniques that could be useful in describing and efficiently sampling from a given probability density. Because it may require many stochastic parameters to describe a random

slip pattern over the fault geometry, the resulting stochastic space is very high dimensional. One approach to describing the slip is by using a Karhunen-Loève expansion in the framework of random spatial methodologies such as Mai and Beroza [37], in which the spatial pattern is written as a linear combination of modes that are taken to be the eigenvectors of a desired covariance matrix. The coefficients are then independent random variables. We put considerable effort into this as a possible way to generate new CSZ realizations. We feel it is a promising approach for future work, but were not able to determine the necessary parameters sufficiently well to make use of this in the present study.

Once a high-dimensional probability density is determined, there are various techniques that may be useful to efficiently sample such a distribution and compute the desired probabilities of inundation. Dimension reduction techniques, importance sampling, multi-level Monte-Carlo, and stochastic collocation are some ideas from the Uncertainty Quantification (UQ) literature that we have started to pursue.

References

[1] K. Abe. Size of great earthquake of 1837-1974 inferred from tsunami data. *J. Geophys. Res.*, 84:1561–1568, 1979.

[2] H. Abramson. Evidence for Tsunami and Earthquakes During the Last 3500 years from Lagoon Creek, a Coastal Freshwater Marsh, Northern California. Master's thesis, Humboldt State University, 1998.

[3] L. Adams, R.J. LeVeque, and F.I. González. The pattern-method for incorporating tidal uncertainty into probabilistic tsunami hazard assessment (ptha). *Natural Hazards*, pages 1–20 (in review), 2014.

[4] Amanda R. Admire, Lori A. Dengler, Gregory B. Crawford, Burak U. Uslu, Jose C. Borrero, S. Dougal Greer, and Rick I. Wilson. Observed and Modeled Currents from the Tohoku-oki, Japan and other Recent Tsunamis in Northern California. *Pure and Applied Geophysics*, February 2014.

[5] C. Amante and B. W. Eakins. ETOPO1 1 Arc-Minute Global Relief Model: Procedures, Data Sources and Analysis. NOAA Technical Memorandum NESDIS NGDC-24, U.S. Dept. of Commerce, Boulder, CO, 2009.

[6] D. Arcas and B. Uslu. A tsunami forecast model for Crescent City, California. PMEL Tsunami Forecast Series: Vol. 2, NOAA OAR Special Report (April 8), 2010.

[7] M. E. M. Arcos and R. J. LeVeque. Velocity measurements near Hawaii compared to model simulations of the 11 March 2011 Tohoku tsunami. *J. Geophys. Res.*, submitted.

[8] Federal Emergency Management Association. Guidelines for design of structures for vertical evacuation from tsunamis. FEMA Report P646, http://www.fema.gov/media-library-data/20130726-1641-20490-9063/femap646.pdf, 2008.

[9] B. F. Atwater, A. R. Nelson, J. L. Clague, G. A. Carver, D. K. Yamagouchi, P. T. Bobrowsky, J. Bourgeois, M. E. Darienzo, W. C. Grant, E. HemphillHaley, H. M. Kelsey, G. C. Jacoby, S. Nishenko, S. P. Palmer, C. D. Peterson, and M. A. Reinhart. Summary of coastal geologic evidence for past great earthquakes at the Cascadia Subduction Zone. *Earthquake Spectra*, 11:1–18, 1995.

[10] S. E. Barrientos and S.N. Ward. The 1960 Chile earthquake: Inversion for slip distribution from surface deformation. *Geophysical Journal International*, 104:589–598, 1990.

[11] M. J. Berger, D. L. George, R. J. LeVeque, and K. T. Mandli. The geoclaw software for depth-averaged flows with adaptive refinement. Preprint and simulations: www.clawpack.org/links/papers/awr10, 2010.

[12] J. L. Blair, P. A. McCrory, and D. H. Oppenheimer. A geo-referenced 3d model of the Juan de Fuca Slab and associated seismicity. http://pubs.usgs.gov/ds/633/, 2012.

[13] I. L. Cifuentes. The 1960 Chilean earthquakes. *J. Geophys. Res.*, 94:665–680, 1989.

[14] I.L. Cifuentes and P.G. Silver. Low-frequency source characteristics of the great 1960 Chilean earthquake. *J. Geophys. Res.*, 94:643–663, 1989.

[15] R. J. Enkin, A. Dallimore, J. Baker, J. R. Southon, and T. Ivanochko. A new high-resolution radiocarbon Bayesian age model of the Holocene and Late Pleistocene from core MD02-2494 and others, Effingham Inlet, British Columbia, Canada; with an application to the paleoseismic event chronology of the Cascadia Subduction Zone. *Canadian Journal of Earth Sciences*, 50:746–760, 2013.

[16] C. E. Garrison-Laney. Diatom Evidence for Tsunami Inundation from Lagoon Creek, a Coastal Freshwater Pond, Del Norte County, California. Master's thesis, Humboldt State University, 1998.

[17] D. L. George. *Finite Volume Methods and Adaptive Refinement for Tsunami Propagation and Inundation.* PhD thesis, University of Washington, 2006.

[18] C. Goldfinger, K. Grijalva, R. Burgmann, A.E. Morey, J.E. Johnson, C.H. Nelson, J. Gutierrez-Pastor, E. Karabanov, J.D. Chaytor, J. Patton, and E. Gracia. Late Holocene rupture of the northern San Andreas Fault and possible stress linkage to the Cascadia Subduction Zone. *Bull. Seis. Soc. Amer.*, 98:861–889, 2008.

[19] C. Goldfinger, A. E. Morey, B. Black, J. Beeson, C. H. Nelson, and J. Patton. Spatially limited mud turbidites on the Cascadia margin: segmented earthquake ruptures? *Nat. Hazards Earth Syst. Sci.*, 13:2109–2146, 2013.

[20] C. Goldfinger, C. H. Nelson, A. E. Morey, J. R. Patton, E. Karabanov, J. Gutierrez-Pastor, and A. T. Eriksson. Turbidite event history–methods and implications for Holocene paleoseismicity of the Cascadia Subduction Zone. USGS professional paper 1661-F July 17, 2012.

[21] F. González, R. J. LeVeque, J. Varkovitzky, P. Chamberlain, B. Hirai, and D. L. George. GeoClaw Results for the NTHMP Tsunami Benchmark Problems. http://depts.washington.edu/clawpack/links/nthmp-benchmarks/geoclaw-results.pdf, 2011.

[22] F. I. González, E L Geist, B. Jaffe, U Kanoglu, et al. Probabilistic tsunami hazard assessment at Seaside, Oregon, for near-and far-field seismic sources. *J. Geophys. Res.*, 114:C11023, Jan 2009.

[23] F.I. González, R.J. LeVeque, and L. Adams. Probabilistic Tsunami Hazard Assessment (PTHA) for Crescent City, CA, Final Report on Phase I, January 13, 2013.

[24] P.R. Grothe, L.A. Taylor, B.W. Eakins, K.S. Carignan, R.J. Caldwell, E. Lim, and D.Z. Friday. Digital elevation models of Crescent City, California: Procedures, data sources and analysis. NOAA Technical Memorandum NESDIS NGDC-51, U.S. Dept. of Commerce, Boulder, CO, 2011.

[25] CA PTHA Working Group. Evaluation and Application of Probabilistic Tsunami Hazard Analysis in California, Aug 2013.

[26] TPSWG (Tsunami Pilot Study Working Group). Seaside Oregon Tsunami Pilot Study-modernization of FEMA flood hazard maps. NOAA OAR Special Rep., NOAA/OAR/PMEL, Seattle, WA, 94 pp. +7 appendices, 2006.

[27] Japan Earthquake Research Center (JERC). Year 2013 calculation reference date (2013) January 1 summary of long-term evaluation of subduction-zone earthquakes. http://www.jishin.go.jp/main/choukihyoka/kaikou.htm with map http://wwwjishin.go.jp/main/p_hyoka02.htm, 2012.

[28] J. M. Johnson and K. Satake. Asperity distribution of the 1952 Great Kamchatka earthquake and its relation to future earthquake potential in Kamchatka. *Pure and Applied Geophysics*, 154:541–553, 1999.

[29] H. M. Kelsey, A. R. Nelson, E. Hemphill-Haley, , and R. C. Witter. Tsunami history of an Oregon coastal lake reveals a 4600 yr record of great earthquakes on the Cascadia subduction zone. *GSA Bulletin*, 117:1009–1032, 2005.

[30] R. J. LeVeque. *Finite Volume Methods for Hyperbolic Problems*. Cambridge University Press, 2002.

[31] R. J. LeVeque and D. L. George. High-resolution finite volume methods for the shallow water equations with bathymetry and dry states. In P. L-F. Liu, H. Yeh, and C. Synolakis, editors, *Advanced Numerical Models for Simulating Tsunami Waves and Runup*, volume 10, pages 43–73, 2007. http://www.amath.washington.edu/ rjl/pubs/catalina04/.

[32] R. J. LeVeque, D. L. George, and M. J. Berger. Tsunami modeling with adaptively refined finite volume methods. *Acta Numerica*, pages 211–289, 2011.

[33] A. T. Linde and P. G. Silver. Elevation changes and the great 1960 Chilean earthquake–support for aseismic slip. *Geophys. Res. Lett.*, 16:1305–1308, 1989.

[34] P. L. F. Liu, Y. S. Cho, S. B. Yoon, and S.N. Seo. 1960 Chilean tsunami propagation and inundation at Hilo, Hawaii. In Y. Tsuchiya, N. Shuto, and Kluwer Academic Publishers, editors, *In Tsunami: Progress in Prediction, Disaster Prevention and Warning*, pages 99–115, 1995.

[35] B. T. MacInnes, A. R. Gusman, R. J. LeVeque, and Y. Tanioka. Comparison of earthquake source models for the 2011 Tohoku-oki event using tsunami simulations and near field observations. submitted, preprint at http://faculty.washington.edu/rjl/pubs/tohoku1/, 2012.

[36] O. Magoon. Structural damage by tsunamis. Proceedings American Society of Civil Engineers , Specialty Conference on Coastal Engineering, Santa Barbara, CA, Chapter 4, Oct., 1965.

[37] P. M. Mai and G. C. Beroza. A spatial random field model to characterize complexity in earthquake slip. *J. Geophys. Res.*, 107:?, 2002.

[38] R. McCaffrey, R.W. King, S.J. Payne, and M. Lancaster. Active tectonics of northwestern U. S. inferred from GPS- derived surface velocities. *J. Geophys. Res. Solid Earth*, 118(2):709–723, 2013.

[39] P. A. McCrory, J. L. Blair, F. Waldhauser, and D. H. Oppenheimer. Juan de Fuca slab geometry and its relation to Wadati-Benioff zone seismicity. *J. Geophys. Res.*, 117:B09306, September 2012.

[40] H.O. Mofjeld, F.I. Gonzáles, V.V. Titov, A.J. Venturato, and J.C. Newman. Effects of tides on maximum tsunami wave heights: Probability distributions. *J. Atmos. Ocean. Technol.*, 24(1):117–123, 2007.

[41] F. Nanayama, K. Satake, R. Furukawa, K. Shimokawa, B.F. Atwater, K. Shigeno, and S. Yamaki. Unusually large earthquakes inferred from tsunami deposits along the Kuril trench. *Nature*, 424:660–663, 2003.

[42] Proceedings and results of the 2011 nthmp model benchmarking workshop. U.S. Department of Commerce/ NOAA/NTHMP; (NOAA Special Report). 436 p., http://nthmp.tsunami.gov/documents/nthmpWorkshopProcMerged.pdf, 2011.

[43] C. D. Peterson, G. A. Carver, K. M. Cruikshank, H. F. Abramson, C. E. Garrison-Laney, and L. A. Dengler. Evaluation of the use of paleotsunami deposits to reconstruct inundation distance and runup heights associated with prehistoric inundation events, Crescent City, southern Cascadia margin. *Earth Surf. Process. Landforms*, 36:967–980, 2011.

[44] T. K. Pinegina, J. Bourgeois, L. Bazanova, I. V. Melekestsev, and O.A. Braitseva. A millennial-scale record of Holocene tsunamis on the Kronotskiy Bay coast, Kamchatka, Russia. quaternary research. *Quaternary Research*, 59:36–47, 2003.

[45] F. F. Pollitz, P. A. McCrory, D. Wilson, J. Svarc, C. Puskas, and R. B. Smith. Viscoelastic-cycle model of interseismic deformation in the northwestern United States. *Geophysical Journal International*, 181:665–696, March 2010.

[46] G. R. Priest, Y. Zhang, R.C. Witter, K. Wang, C. Goldfinger, and L. Stimely. Tsunami impact to Washington and northern Oregon from segment ruptures on the southern Cascadia subduction zone. *Nat. Hazards*, pages 1–22, 2014.

[47] L. J. Ruff and H. Kanamori. The rupture process and asperity distribution of three great earthquakes from long-period diffracted p-waves. *Physics of the Earth and Planetary Interiors*, 31:202–230, 1983.

[48] I. Salgado, A. Eipert, B.F. Atwater, M. Shishikura, and M. Cisternas. Recurrence of giant earthquakes inferred from tsunami sand sheets and subsided soils in southcentral Chile (abstract). Geological Society of America Abstracts with Programs, 2003.

[49] C. H. Scholz. *The mechanics of earthquakes and faulting.* Cambridge University Press, 1990.

[50] C.H. Scholz. Holocene earthquake history of Cascadia: A quantitative test. *Bulletin of the Seismological Society of America*, 104(4), 2014.

[51] G. Shao, X. Li, C. Ji, and T. Maeda. Focal mechanism and slip history of 2011 mw 9.1 off the Pacific coast of Tohoku earthquake, constrained with teleseismic body and surface waves. *Earth Planets Space*, 63:559–564, 2011.

[52] A. Suppasri, S. Koshimura, and F. Imamura. Developing tsunami fragility curves based on the satellite remote sensing and the numerical modeling of the 2004 Indian Ocean tsunami in Thailand. *Nat. Hazards Earth Syst. Sci.*, 11:173–189, 2011.

[53] V. V. Titov and F. Gonzales. Implementation and testing of the method of splitting tsunamis (MOST) model. NOAA Tech. Memo. ERL PMEL-112, 1997.

[54] USGS. 2014 Preliminary Hazard Maps, Chapter 5: Earthquake Recurrence and Down Dip Edge of Rupture for the Cascadia Subduction Zone, June 2013.

[55] K. Wang, R. Wells, S. Mazzotti, R.D. Hyndman, and T. Sagiya. A revised dislocation model of inter-seismic deformation of the Cascadia subduction zone. *J. of Geophysical Research*, 108(1):9–1 – 9–13, 2003.

[56] S. N. Ward. Earthquake mechanisms and tsunami generation: The Kuril Islands event of 13 October 1963. *Bulletin of the Seismological Society of America*, 72:759–777, 1982.

[57] R. Wilson, A. Admire, J. Borrero, L. Dengler, M. Legg, P. Lynett, K. Miller, A. Ritchie, K. Sterling, and P. Whitmore. Observations and impacts from the 2010 Chilean and 2011 Japanese tsunamis in California. *Pure and Applied Geophysics*, 2012.

[58] R. Wilson, C. Davenport, and B. Jaffe. Sediment scour and deposition within harbors in California (USA), caused by the March 11, 2011 Tohoku-oki tsunami. *Sedimentary Geology*, 282:228–240, 2012.

[59] R. Wilson, K. Miller, C. Davenport, T. Nicolini, L. Dengler, A. Admire, and C. Synolakis. Comparison of strong currents and impacts on the California (USA) maritime communities from the 2010 Chile and 2011 Japan Teletsunamis. American Geophysical Union fall meeting 2011, Abstract NH1AA-1342, December 9: 1-1, 2011.

[60] R. C. Witter, Y. Zhang, K. Wang, C. Goldfinger, G. R. Priest, and J. C. Allan. Coseismic slip on the southern Cascadia megathrust implied by tsunami deposits in an Oregon lake and earthquake-triggered marine turbidites. *J. Geophys. Res.*, 117:B10303, 2012.

[61] R. C. Witter, Y. Zhang, K. Wang, G. R. Priest, C. Goldfinger, L. L. Stimely, J. T. English, and P. A. Ferro. Simulating tsunami inundation at Bandon, Coos County, Oregon, using hypothetical Cascadia and Alaska earthquake scenarios. Oregon Department of Geology and Mineral Industries Special Paper 43, 2011.

APPENDICES

A Generating hazard curves ignoring tidal variation

A key step in our probabilistic approach to producing hazard maps is the generation of a *hazard curve* at each point on a fine grid covering Crescent City and the surrounding area. The terminology of hazard curves has been used for many years in probabilistic *seismic* hazard assessment (PSHA) and has been adopted in PTHA and used in past studies such as [22]. The hazard curve for inundation at a fixed (x, y) location (longitude and latitude) shows maximum depth of inundation ζ on the horizontal axis and probability of exceeding this value on the vertical axis. This is a cumulative probability function, but the fact that we consider the probability of *exceeding* each value means the probability does not generally approach 1 as $\zeta \to 0$. Instead, the value $P(0; x, y)$ is the probability of having any flooding ($\zeta > 0$) at this point (x, y).

A sample hazard curve is shown in Figure 62 for the point $(235.80719, 41.75391)$, the location of Gauge 105 in Figure 2. This simple example was created by assuming that the only possible events are the first 3 AASZ characteristic tsunamis discussed in Section 7.1, and using the recurrence times from Table 3. We have also ignored tidal uncertainty to begin with and only consider inundation computed when the simulation is run at MHHW. The incorporation of tidal uncertainty is discussed in the next section.

By examining the synthetic tide gauge records at Gauge 105 for each of the three AASZ sources, the maximum depth of water, $\hat{\zeta}$, at this point can be determined for each scenario, with the maximum depths and annual probability of occurrence as given in Table 3.

$$
\begin{array}{lll}
\text{AASZe01:} & \hat{\zeta}_1 = 1.9 \text{ m} & p_1 = 1/1313 = 0.000762 \\
\text{AASZe02:} & \hat{\zeta}_2 = 1.3 \text{ m} & p_2 = 1/750 = 0.00133 \\
\text{AASZe03:} & \hat{\zeta}_3 = 4.0 \text{ m} & p_3 = 1/750 = 0.00133
\end{array}
$$

Table 3: Three distinct AASZ events with the depth they inundate at one fixed (x, y) point.

We see from this data that there is 0 probability of exceeding depth $\zeta = 4$, while for any value of ζ between 1.9 and 4, the probability of exceedance is $p_3 = 0.00133$, since only one event AASZe03 inundates to this level.

On the other hand there are two events (AASZe03 and AASZe01) that exceed 1.3 m, and so for any ζ between 1.3 and 1.9 the probability of exceedance must be computed taking into account that either event might occur.

If two events are independent with annual probabilities p_i and p_j then the probability of at least one event happening is

$$
p_{ij} = 1 - (1 - p_i)(1 - p_j) = p_i + p_j - p_i p_j \approx p_i + p_j.
$$

Hence the probability of event 1 or 3 happening is $p_{13} \approx 0.0021$, and this is the value displayed on the hazard curve for $1.3 < \zeta < 1.9$. Note that if $p_i = 1 - e^{-\mu_i}$ and $p_j = 1 - e^{-\mu_j}$ then $p_{ij} = 1 - e^{-\mu_i}e^{-\mu_j} = 1 - e^{-(\mu_i + \mu_j)}$, so the combined probability can also be computing by adding the Poisson rates $\mu_i = 1/T_i$.

Similarly, for $0 < \zeta < 1.3$ there are three possible events (AASZe03, AASZe01, or AASZe02) that give this level of inundation and so for any ζ in this range the probability of exceedance is $p_{134} = 0.0034$, computed via

$$
p_{ijk} = 1 - (1 - p_i)(1 - p_j)(1 - p_k) = p_{ij} + p_k - p_{ij}p_k \approx p_i + p_j + p_k.
$$

The latter approximation is valid if all probabilities are much less than 1. Similar formulas hold when more than 3 events are considered.
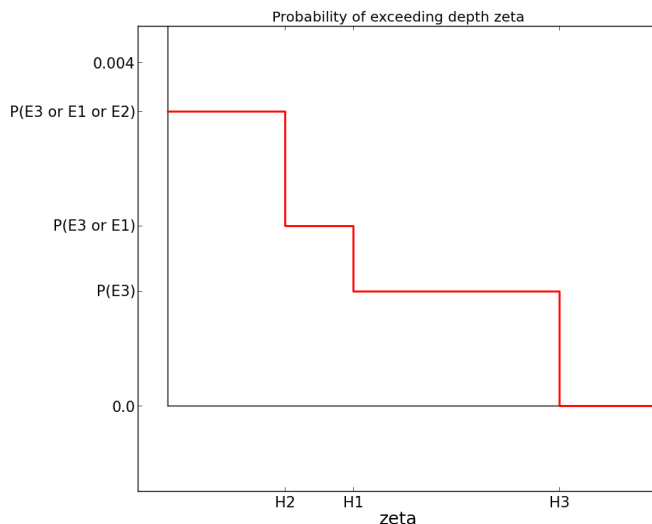
Figure 62: Sample hazard curve for a fixed (x, y) point when three distinct events are considered that give inundation to three depths. Using the data from Table 3.

With only three possible discrete events to consider, the hazard curve is piecewise constant with jump discontinuities at the values $\zeta = \hat{\zeta}_2, \ \hat{\zeta}_1, \ \hat{\zeta}_3$ corresponding to the maximum inundation observed for each event. The magnitude of each jump is approximately equal to the probability of the corresponding event, as long as the sum of all probabilities of larger events is much less than 1.

Note that if an additional event were added that gave maximum inundation $\bar{\hat{\zeta}}$ at the (x, y) point being studied, then a new jump discontinuity would be added to the hazard curve at the point $\bar{\hat{\zeta}}$, with the portion of the curve to the left of $\bar{\hat{\zeta}}$ shifted upwards by approximately $\bar{p}$, the probability of occurance of this event. (More exactly by $1 - (1 - \bar{p}) \prod_k (1 - p_k)$ where the product is over all events with inundation $\hat{\zeta}_k > \bar{\hat{\zeta}}$.)

Note also that if there is uncertainty in the exact details of the slip pattern for one of these events, then we might replace the single realization, say AASZe01, by N slightly different realizations, which might give a range of inundations near $\hat{\zeta}_1$. If we assigned each a probability p_1/N, for example, then the hazard curve would be unchanged except in the vicinity of $\hat{\zeta}_1$, where the discontinuity of magnitude $p_{13} - p_3$ would be replaced by N discontinuities each with magnitude roughly $1/N$ as large, distributed near $\hat{\zeta}_1$ at points corresponding to the maximum inundation of each of these N realizations. If we considered a continuous distribution of possible realizations of AASZe01, then this would generally tend to smooth out the discontinuity into a continuous curve between the minimum and maximum inundations observed for different realizations, with the total drop in the exceedance probability over this interval remaining constant at $p_{13} - p_3$. If we do this for each of the events shown in Table 3 and Figure 62, we might get a hazard curve similar to what is shown in Figure 63. As explained in the next section, a similar smoothing of the hazard curve is observed when tidal uncertainty is incorporated, since this also increases the range of inundation values ζ that can be observed for each event.

In practice we do not attempt to compute the hazard curve probabilities for all values of ζ at each (x, y). Instead we choose a finite set of exceedance values ζ_k and determine the probability of exceeding each ζ_k. We then approximate the hazard curve by a piecewise linear function that interpolates these values $(\zeta_k, \ P(\zeta_k; x, y))$. The left plot in Figure 64 shows this approximation for the previous example. We do this because computing each value $P(\zeta_k; x, y)$ requires combining information from all simulation runs together with tidal variation, as described in the next section, and is somewhat costly to perform. By choosing a
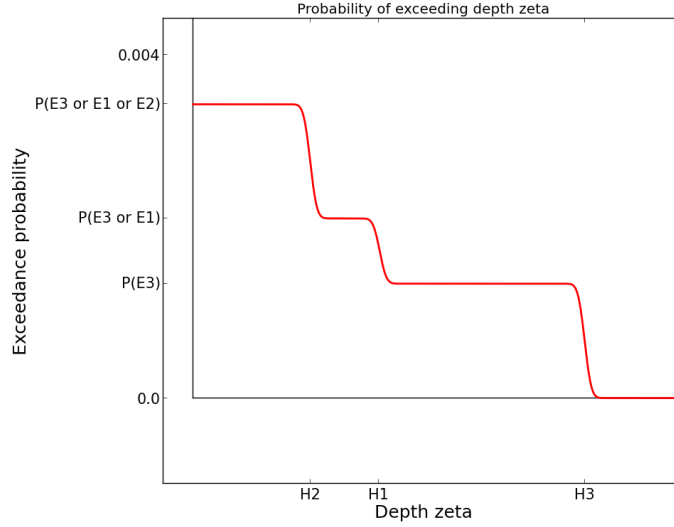
Figure 63: Sample hazard curve as in Figure 62, but with uncertainty in the amplitude added. The probability of each event is the same as before, but the extent of inundation may vary between different realizations, leading to a spreading of the jump discontinuity.

finite set of ζ_k values the postprocessing is also simplified.

We have chosen the following exceedance values:

$$
\begin{aligned}
\zeta_k = 0,\ 0.1,\ 0.2,\ &\ldots,\ 1.9,\ 2.0, \\
&2.5,\ 3.0,\ \ldots,\ 5.5,\ 6.0, \\
&7.0,\ ,8.0,\ \ldots,\ 12.0,
\end{aligned}
\tag{4}
$$

which we believe is sufficiently dense to yield good approximations of the hazard curves in general.

Likewise, we have chosen the following exeedance values (in m/s) for our analysis of speed,

$$
\zeta_k = 0.0,\ 0.5,\ 1.0,\ \ldots,\ 16.5,\ 17.0\,,
\tag{5}
$$

and the following exceedance values (in m^3/s^2) for our analysis of momentum flux,

$$
\begin{aligned}
\zeta_k = 0.01,\ 0.05,\ 0.1,\ 0.2,\ &\ldots,\ 2.0, \\
&4.0,\ 6.0,\ 8.0,\ 10.0,\ 20.0,\ 50.0 \\
&100.0,\ 200.0,\ 400.0,\ 600.0,\ 1000.0,\ 1500.0,\ 1700.0\,.
\end{aligned}
\tag{6}
$$

The hazard curve for ζ determined from considering only the three events discussed above is shown in Figure 64.

Once the hazard curve at each (x, y) has been determined, the information contained in this curve can be used in two distinct ways. For a given probability such as $\bar{p} = 0.01$ it is possible to find the corresponding value ζ for which $P(\zeta; x, y) = 0.01$. This could be interpreted as the depth of inundation expected in a "100-year event". By determining this for each (x, y) it is possible to plot the extent of inundation expected with probability $\bar{p}$ and the flow depth at each point inundated.

Conversely, one can choose a particular inundation level $\tilde{\zeta}$ and determine the probability of exceeding this value $P(\tilde{\zeta}; x, y)$ at each point. A contour plot of this value over the spatial (x, y) domain then shows
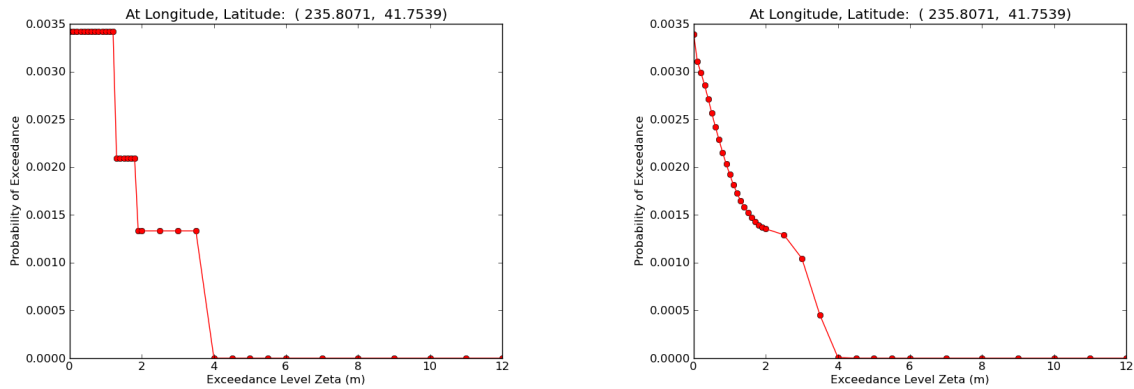
93

Figure 64: Sample hazard curve for a fixed (x, y) point when three distinct events are considered that give inundation to three depths. Left: Using the data from Table 3, as in Figure 62 but illustrating the use of a finite number of exceedance values ζ_k. Right: Corresponding curve for the same three events but when tidal uncertainty is included.

the probability of exceeding $\tilde{\zeta}$ at each point in the community. In particular, choosing $\tilde{\zeta} = 0$ would show probability contours of seeing any flooding. The $p = 0.01$ contour would again correspond to the inundation limit of the "100-year event". This approach and the advantages of generating maps of this form are discussed further in Section 9.2.

B Generating hazard curves including tidal variation

We consider J tsunami events, with event E_j having a recurrence rate ν_j that obeys a Poisson process. That is, the probability that E_j occurs is $P(E_j) = 1 - e^{-\nu_j}$. We are interested in finding the probability that inundation height ζ exceeds level ζ_i at a grid location of interest. Typically, we are interested in all grid locations covering a fixed grid of the Crescent City area. The same procedure we outline below also applies when we let ζ and ζ_i represent speed (or momentum flux) and a chosen exceedance level for speed (or momentum flux), respectively.

The probability that E_j does not produce exceedance of ζ_i is

$$1 - (1 - e^{-\nu_j}) \, P(\zeta > \zeta_i \,|\, E_j).$$

Then the probability that at least one event gives exceedance of ζ_i is

$$P(\zeta > \zeta_i) = 1 - \prod_{j=1}^{J} \left(1 - (1 - e^{-\nu_j}) \, P(\zeta > \zeta_i \,|\, E_j) \right). \tag{7}$$

Furthermore, if event E_j is composed of k_j mutually exclusive realizations, so that when E_j occurs, exactly one of the realizations occurs, say E_{jk}, we can substitute

$$P(\zeta > \zeta_i \,|\, E_j) = \sum_{k=1}^{k_j} P(\zeta > \zeta_i \,|\, E_{jk}) \, P(E_{jk} \,|\, E_j)$$

where $\sum_{k=1}^{k_j} P(E_{jk} \,|\, E_j) = 1$ into equation (7) to get

$$P(\zeta > \zeta_i) = 1 - \prod_{j=1}^{J} \left(1 - (1 - e^{-\nu_j}) \sum_{k=1}^{k_j} P(\zeta > \zeta_i \,|\, E_{jk}) \, P(E_{jk} \,|\, E_j) \right). \tag{8}$$

If we define $\bar{\mu}_{ij}$ as

$$\bar{\mu}_{ij} = (1 - e^{-\nu_j}) \sum_{k=1}^{k_j} P(\zeta > \zeta_i \,|\, E_{jk}) \, P(E_{jk} \,|\, E_j), \tag{9}$$

equation (8) can be written as

$$P(\zeta > \zeta_i) = 1 - \prod_{j=1}^{J} (1 - \bar{\mu}_{ij}) \tag{10}$$

and following the discussion in Section 2.6.1, can be approximated as

$$P(\zeta > \zeta_i) = 1 - \prod_{j=1}^{J} e^{-\bar{\mu}_{ij}}. \tag{11}$$

If we again use the discussion in Section 2.6.1 to approximate $\bar{\mu}_{ij}$ in equation (9) by μ_{ij}, where

$$\mu_{ij} = \nu_j \sum_{k=1}^{k_j} P(\zeta > \zeta_i \,|\, E_{jk}) \, P(E_{jk} \,|\, E_j), \tag{12}$$

we arrive at the expression for $P(\zeta > \zeta_i)$ that was used by González,et.al. [22] in the Seaside, Oregon study. That is,

95

$$P(\zeta > \zeta_i) = 1 - \prod_{j=1}^{J} e^{-\mu_{ij}}. \tag{13}$$

By varying $i = 1 \ldots Z$ to cover more exceedance levels of interest, we can calculate the pairs $(\zeta_i, P(\zeta > \zeta_i))$, $i = 1 \ldots Z$ and construct a hazard curve for each fixed grid point of interest.

C   The 100- and 500-year flood: η-contour maps

The deliverable maps required by FEMA are the 100-year and 500-year hazard maps shown in Section 3 and those in this Appendix. The maps in Section 3 show ζ, where ζ is the flow depth on land and the height above MHW for a grid location in the sea. The plots below are the same with η plotted, where η is the height above MHW on either the land ($\eta = \zeta + B$) or in the sea ($\eta = \zeta$). For a land point, B is the pre-earthquake bathymetry measured above MHW. These two plots are exactly those of Figure 3 and 6, with η plotted instead of ζ. For simplicity, and because maximum flow depth ζ is the most easily visualized expression of the physical flooding hazard, we chose to work only with ζ in the body of this report.
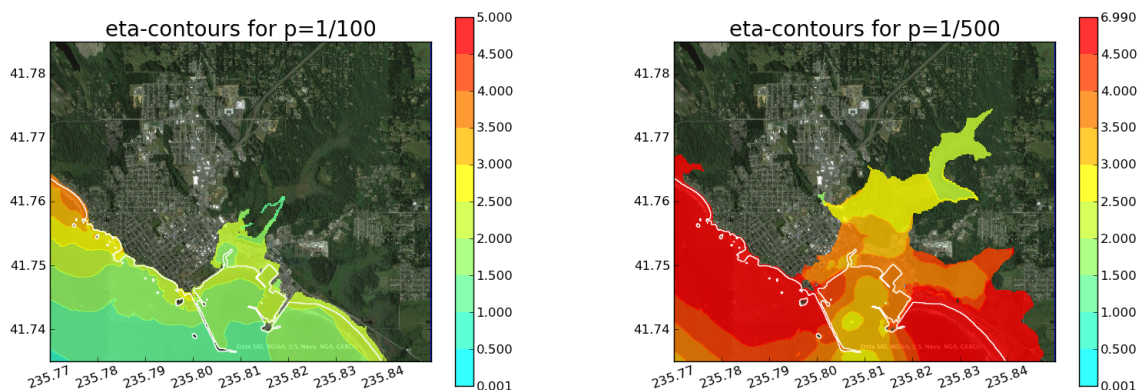

Figure 65: η-contours for Table 1 sources for p=.01 (Left) and p=.002 (Right), with $T_M = 250$ for Cascadia

D   Data files

Eight data files will be provided to BakerAECOM to accompany this report, ASCII text format. Each file has 467,965 lines, one for each grid point in the 1/3" grid covering the city and harbor. The files are:

1. `xyB.txt`: The file containing the $(x, y) = $ (longitude, latitude) coordinates of each point in columns 1 and 2 and the topography/bathymetry of the point in column 3. The pre-earthquake bathymetry is in meters relative to MHW (positive on land).

2. `Zeta.txt` Column 1 is the ζ value for the 100-year ($p = 0.01$) flood and column 2 is the ζ value for the 500-year ($p = 0.002$) flood. This was computed using all sources in Table 1, assuming a return time of 250 years for the CSZ sources. This is the data plotted in Figure 3 and Figure 6.

3. `Eta.txt` Column 1 is the η value for the 100-year ($p = 0.01$) flood and column 2 is the η value for the 500-year ($p = 0.002$) flood. This was computed using all sources in Table 1, assuming a return time of 250 years for the CSZ sources. This is the data plotted in Figure 65.

4. `Speed.txt` Column 1 is the speed value for the 100-year ($p = 0.01$) flood and column 2 is the speed value for the 500-year ($p = 0.002$) flood. This was computed using all sources in Table 1, assuming a return time of 250 years for the CSZ sources. This is the data plotted in Figure 4 and in Figure 7.

5. `Mflux.txt` Column 1 is the momentum flux value for the 100-year ($p = 0.01$) flood and column 2 is the momentum flux value for the 500-year ($p = 0.002$) flood. This was computed using all sources in Table 1, assuming a return time of 250 years for the CSZ sources. Here, the momentum flux is calcuated as the square of the speed times the value of flow depth h, as described in Section 2.6. This is the data plotted in Figure 5 and in Figure 8.

6. `exceedance_probs_Zeta.txt` This file has 35 columns, giving the probability of exceedance for each of 35 different exceedance levels ζ_i for $i = 1, 2, \ldots, 35$ as listed in (4) and repeated here:

$$\zeta_i = 0, \ 0.1, \ 0.2, \ \ldots, \ 1.9, \ 2.0,$$
$$2.5, \ 3.0, \ \ldots, \ 5.5, \ 6.0,$$
$$7.0, \ ,8.0, \ \ldots, \ 12.0 \,.$$

Plotting these ζ_i values against a row of the file will produce the hazard curve at the corresponding grid point. This file contains exceedance probabilities when all sources in Table 1 are used, with a return time of 250 years for CSZ.

7. `exceedance_probs_speed.txt` This file has 35 columns, giving the probability of exceedance for each of 35 different exceedance levels speed_i for $i = 1, 2, \ldots, 35$ as listed in (5) and repeated here:

$$\text{speed}_i = 0.0, \ 0.5, \ 1.0, \ \ldots, \ 16.5, \ 17.0 \,.$$

Plotting these speed_i values against a row of the file will produce the hazard curve for speed at the corresponding grid point. This file contains exceedance probabilities when all sources in Table 1 are used, with a return time of 250 years for CSZ.

8. `exceedance_probs_mflux.txt` This file has 35 columns, giving the probability of exceedance for each of 35 different exceedance levels mflux_i for $i = 1, 2, \ldots, 35$ as listed in (6) and repeated here:

$$\text{mflux}_i = 0.01, \ 0.05, \ 0.1, \ 0.2, \ \ldots, \ 2.0,$$
$$4.0, \ 6.0, \ 8.0, \ 10.0, \ 20.0, \ 50.0$$
$$100.0, \ 200.0, \ 400.0, \ 600.0, \ 1000.0, \ 1500.0, \ 1700.0 \,.$$

Plotting these mflux_i values against a row of the file will produce the hazard curve for momentum flux at the corresponding grid point. This file contains exceedance probabilities when all sources in Table 1 are used, with a return time of 250 years for CSZ.

E Momentum flux and hydrodynamic forces

The GeoClaw code keeps track of the maximum value of the momentum flux hu^2 observed at each point over the full run and these values were originally plotted, e.g. in Figure 8 and reproduced for convenience in Figure 66 below. The units of hu^2 are m^3/s^2.

Of more interest in terms of the engineering application is the hydrodynamic force on a structure, given by

$$\text{force} = \frac{1}{2} C_d \, \rho A u^2,$$

where C_d is a dimensionless drag coefficient, ρ is the density of the fluid, A is the area, and u is the velocity. For tsunami applications, we assume the area of impact is the depth of the fluid times the breadth of the structure in the cross-flow direction (denoted by B), and so the force is

$$\text{force} = \frac{1}{2} C_d \, \rho B h u^2.$$

The force per unit length in the cross-flow direction is thus directly proportional to the momentum flux,

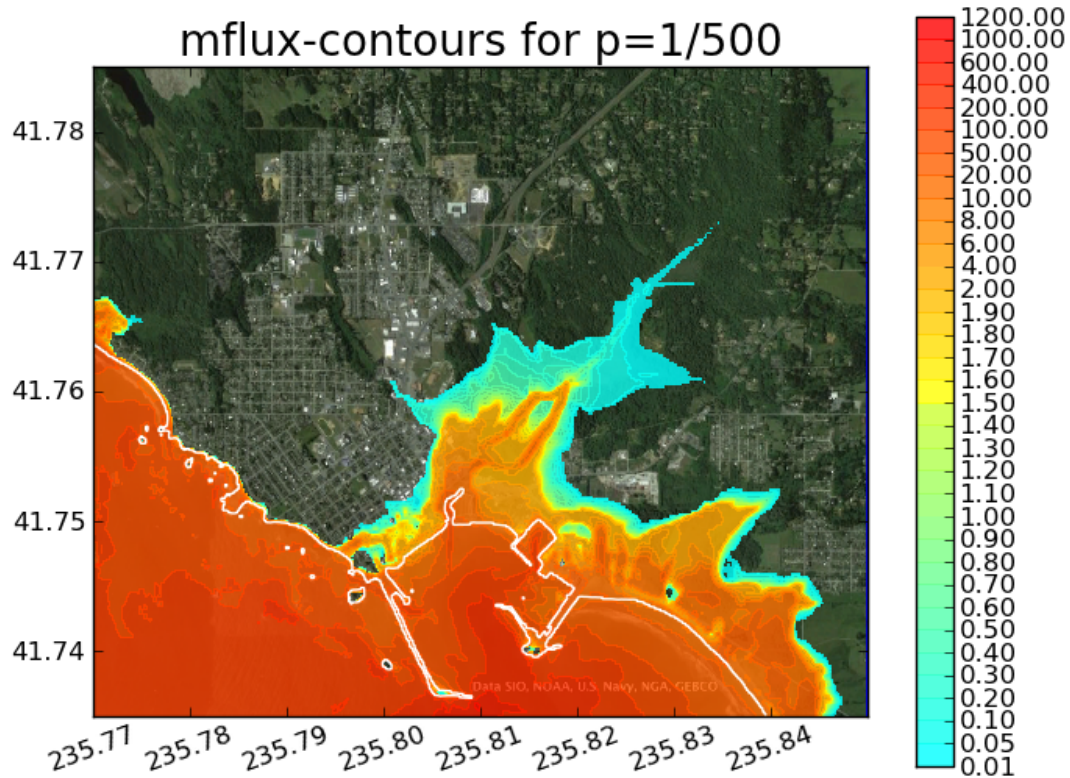$$\text{force / unit length} = \frac{1}{2} C_d \, \rho h u^2.$$

Figure 66: mflux-contours for p=.002. This product was created using all the study sources in Table 1. This includes CSZ with recurrence time $T_M = 250$ years and a representative Japan source with recurrence time $T_M = 103$ years. Note that momentum flux is measured in (m^3/s^2). Appendix E shows that this quantity can be measured in (kN/m) by multiplying the numbers on the colorbar by 1.8.

Section 6.5.4 of FEMA P646 [8] recommends the following:

- $C_d = 2$ for hydrodynamic forces or $C_d = 3$ to include the larger "surge force" of the water initially hitting the structure.

- $\rho = 1200$ kg/m^3 for the fluid density to model seawater with sediment load.

This suggests multiplying hu^2 by a factor of 1.8 to convert into force per unit length in units of kN/m. (kN = kilo Newton = 1000 kg m/s^2).

Figure 8 from the report is repeated in Figure 66. Rescaling the colorbar, the transition from green to yellow is at about 1.5 m^3/s^2 = 2.7 kN/m. Note that the color scale is logarithmic and values of 10 and 100 m^3/s^2 on the color bar convert to 18 and 180 kN/m respectively.

Figure 67 below shows a plot from [52], and shows fragility curves from two sites studied following the 2004 Sumatra event. They show the fraction of structures destroyed as a function of the force per unit length in units of kN/m.
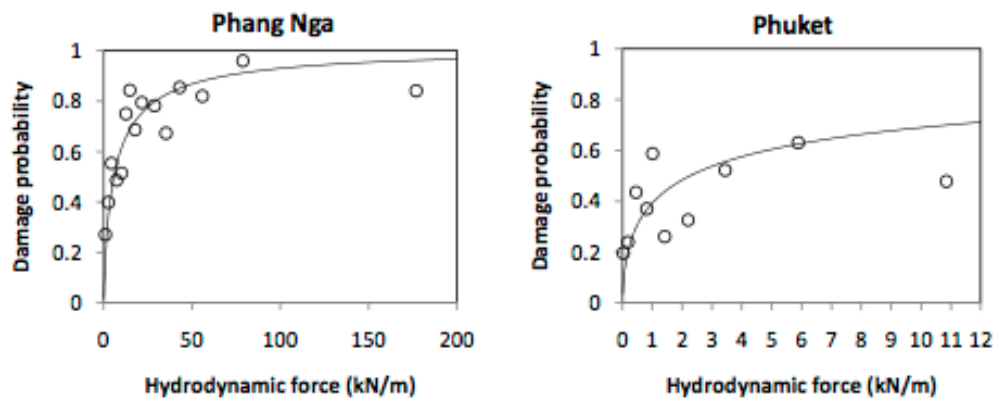
Figure 67: Fragility curves from [52].